Traveling-Wave Metal-Insulator-Metal Diodes for Infrared Optical Rectennas

by

Bradley Pelz

B.S., Washington University in Saint Louis, 2010

M.S., University of Colorado, Boulder, 2017

A thesis submitted to the

Faculty of the Graduate School of the

University of Colorado in partial fulfillment

of the requirements for the degree of

Doctor of Philosophy

Department of Electrical, Computer, and Energy Engineering

2018

This thesis entitled:
Traveling-Wave Metal-Insulator-Metal Diodes for Infrared Optical Rectennas
written by Bradley Pelz
has been approved for the Department of Electrical, Computer, and Energy Engineering

Prof. Garret Moddel

Prof. Wounjhang Park

Date

The final copy of this thesis has been examined by the signatories, and we find that both the content and the form meet acceptable presentation standards of scholarly work in the above mentioned discipline.

Pelz, Bradley (Ph.D., Electrical Engineering)

Traveling-Wave Metal-Insulator-Metal Diodes for Infrared Optical Rectennas

Thesis directed by Prof. Garret Moddel

Infrared optical rectennas absorb electromagnetic radiation in a micro-antennas and rectify the AC signal with high speed diodes. These devices have applications in detection and energy harvesting. Metal-insulator-metal (MIM) diodes provide an excellent option for the high speed diode required for optical rectification, but are limited by poor coupling efficiency to the antenna due to their capacitive nature. One option to improve the antenna/diode coupling efficiency is the traveling-wave diode (TWD). By changing the diode to an MIM transmission line structure that acts like a distributed rectifier, the impedance seen by the antenna becomes the input impedance of the transmission line rather than the capacitive impedance of the lumped-element diode.

The germanium shadow mask is an effective method for fabricating TWD rectennas and has several benefits. First, this technique requires only a single lithography step, which helps reduce processing time. The critical feature sizes are controlled by angled metal evaporations at a higher resolution than the lithography used pattern the shadow mask. Finally, it keeps contaminates such as photoresist away from the sensitive MIM diode junction and results in high diode yield.

A simplified TWD geometry is modeled in COMSOL. Since linear FEM solvers cannot handle a nonlinear $I(V)$ characteristic, the rectification is calculated as part of the post processing. The fabricated devices are experimentally measured with infrared illumination from a CO_2 laser with an automated measurement system. The measured system responsivites are as high as 471 μA/W, which is within a factor of ten of a commercially available HgCdTe photodiode detector. With additional development, the TWD is expected to surpass this existing technology.

Despite the coupling efficiency improvements of more than three orders of magnitude for the TWD compared to the lumped-element, the overall improvement is limited. This limitation is because in the TWD there is an additional loss mechanism: the propagation of the surface plasmon

along the MIM interface. The thin insulator required to support electron tunneling leads to very high field confinement and lossy plasmonic propagation. In a lumped-element rectenna, once the AC power enters the diode, all of it is available to be rectified. Alternatively, in a TWD, since all the rectification does not occur at the same location, the field that couples to the diode must still propagate along the MIM interface, and this propagation loss becomes costly. Because of this limitation, the traveling-wave rectenna probably cannot achieve efficiencies high enough for practical energy harvesting in the current configuration. However, the work in this thesis has shown that the coupling efficiency limitations of MIM rectennas can be circumvented through careful engineering of the diode input impedance as seen by the antenna. This means that capacitance compensation works, and high coupling efficiencies are possible. Infrared optical rectennas with some alternative, low-loss, compensation structure show promise as energy harvesters.

Acknowledgements

First and foremost I would like to express my sincere gratitude to my advisor, Professor Garret Moddel, for the opportunity to work in his lab. Garret's passion for taking on the toughest research challenges is inspiring. He provided invaluable insight, challenged my conclusions, and pushed for deep understanding. I could not have imagined a better advisor.

Next, I would like to thank my committee members, Professor Steven George, Professor Wounjhang Park, Professor Sean Shaheen, and Professor Bart Van Zeghbroeck for their participation in my comprehensive exam and thesis defense. An additional thank you to Professor Park for his thoughtful insights on the plasmonic characteristics of the traveling-wave rectenna.

To previous graduate student lab members Olga Dmitriyeva, James Zhu, and Saumil Joshi, thanks for helping me get started. The insight and support they provided were invaluable.

Without the financial support of RedWave Energy in conjunction with Advanced Research Projects Agency-Energy (ARPA-E), much of this work would not have been possible. I am grateful for Jim Nelson's tireless fund raising efforts and Pat Brady's tenacious approach to pushing MIM diode and rectenna technology forward. The opportunity to work with RedWave has given me access to a wealth of knowledge from some amazing scientists and engineers. Dr. Michael Cromar shared his extensive knowledge of thin film deposition and vacuum equipment. Even after he left RedWave to pursue other career opportunities, he continued to help troubleshoot equipment and process complications at a moments notice. Dr. Brad Herner enhanced my understanding of device fabrication best practices and expanded my knowledge of available techniques. In a similar manner, Dr. Miena Armanious shared his extensive electromagnetic simulation knowledge. Without his help

and insight, my simulation model would have been far less robust.

To the members of the RedWave team at the University of Missouri Patrick Pinhero and Zach Thacker for their contributions to understanding material characteristics at at terahertz frequencies.

To my current lab members, Amina Belkadi, Ayendra Weerakkody, and John Stearns for keeping the day to day fun, productive and interesting.

As the most senior member of the lab, a special thanks to Dave Doroski. Dave keeps the lab running; whatever is needed, from tube furnace repair and to sputter system maintenance, to urgent thermal evaporations and plumbing needs. Dave is always there to lend a helping hand.

To my all Boulder friends (Cam, Clay, Christine, Dennis, Martin, & Phoebe) who helped me achieve the play-hard portion of work-hard, play-hard lifestyle. Nothing relieved the stress of stubborn research problems better than a good adventure, and you guys were always ready to get after it.

To Lorena, for her tireless support during the long process of compiling my work into a thesis. Her encouragement always provided me a much needed boost.

Finally, to my family, all their love and support are truly appreciated. To my brother Ben for his interest in my work and frequent visits. To my sister Dana for the inspiring way in which she has dealt with her own life challenges. To my dad for helping foster my initial interest of how things work to his enthusiasm for the details of any given research challenge. To my mom, for the selfless support of everything I pursue. I can never thank them enough.

Contents

Chapter

Tables

Table

Figures

Figure

Chapter 1

Introduction

1.1 Rectennas

A rectenna, illustrated in Figure 1.1, is an antenna coupled to a diode. The antenna absorbs an electromagnetic wave and the diode rectifies the signal to give a DC output. Rectennas were first demonstrated at microwave frequencies by Brown in the 1960's (Neil et al., 1969). In the 1970's Bailey proposed the concept of optical rectennas (Bailey, 1972). Infrared optical rectennas have potential applications in both detection and energy harvesting.

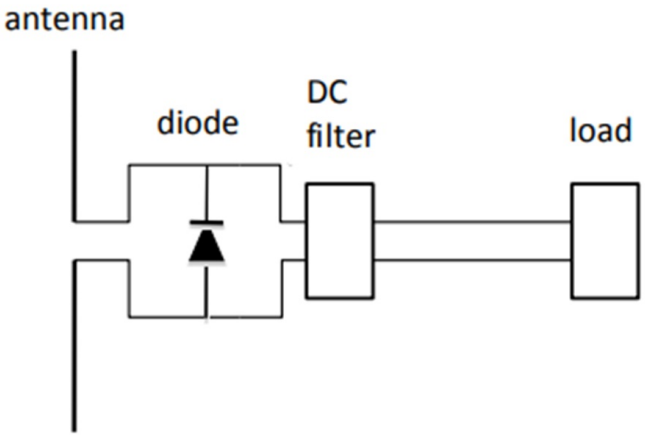

Figure 1.1: Rectenna diagram (Zhu, 2014).

While microwave rectennas can make use of semiconductor diodes and can operate at overall power conversion efficiencies up to 90% (Zhang and Huang, 1980), optical rectennas require an ultra-fast diode to operate at in the terahertz region. The speed of semiconductor diodes is limited

by their plasma frequency and electron mobility. For this reason, metal-insulator-metal (MIM) diodes, which use femtosecond fast electron tunneling for rectification, are an excellent candidate (Hartman, 1962; Heiblum et al., 1978; Eliasson, 2001; Miskovsky et al., 2012; Nagae, 1972).

1.2 Metal-Insulator-Metal Diodes

MIM diodes are formed by separating two metals with a thin insulator (∼2-6 nm). The metal-insulator junction forms a barrier with a height, ϕ_b, that is determined by the difference between the metal work function and the insulator electron affinity as shown in Figure 1.2 (a).

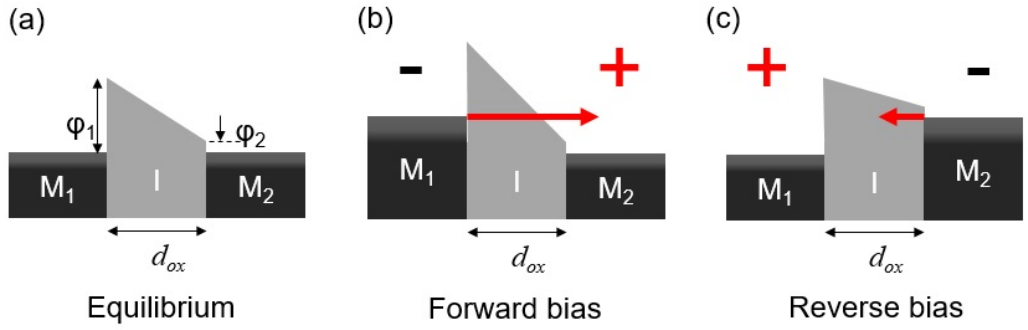

Figure 1.2: MIM energy band structure. Where M_1 and M_2 are the diode metals, I is the diode insulator with thickness d_{ox}. The barrier formed between M_1/I and M_2/I is ϕ_1 and ϕ_2 respectively.

When metals with different work functions are used on either side of the insulator, the two metal-insulator junctions will have different barrier heights. At equilibrium, the Fermi levels of metals align, and the conduction band of the insulator bends accordingly, as shown by Figure 1.2 (a). This asymmetric barrier gives rise to an asymmetric tunneling characteristic. When the diode is forward biased, as illustrated in Figure 1.2 (b), the insulator bends further, reducing the distance the electron must tunnel. In the opposite bias, Figure 1.2 (c), the effective tunneling distance is increased, resulting in a lower tunneling current.

Adding a second insulator can make diodes more asymmetric (Grover and Moddel, 2012). Double insulator MIM didoes fall into two categories, step diode and resonant diode. In the

resonant tunneling case, shown in Figure 1.3 (a), the bending of the insulator conduction bands forms a quantum well. When the structure is biased to drive electrons from M_1 to M_2, the Fermi level of M_1 can align with the resonant states in the well, resulting in a high forward current.

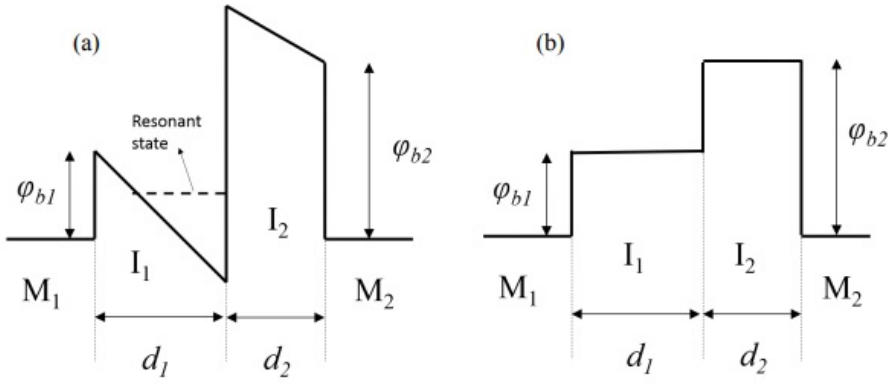

Figure 1.3: MIIM energy band structure (a) resonant diode (b) step diode(Joshi, 2015). The insulators, I_1 and I_2 have thicknesses d_1 and d_2 respectively. The metals, M_1 and M_2, form barriers with height ϕ_{b1} and ϕ_{b2} with their respective insulators.

Figure 1.3 (b) shows a step diode energy band diagram. In a step diode, when the bias is applied to drive electrons from M_2 to M_1, the Fermi level of M_2 can be raised far enough that electrons that tunnel through I_2 are at a high enough energy to be injected into the conduction band of I_1. In the reverse direction, electrons must tunnel though both I_1 and I_2.

Despite the ultrafast nature of electron tunneling (on the order of femtoseconds), a fast rectification mechanism is not the only requirement of an efficient optical rectenna diode. The efficiency of rectennas can be broken down into three major components shown in Eq. 1.1: η_{ant} which is the antenna efficiency, η_c which is the coupling efficiency between the antenna and the diode, and finally, η_d, the diodes rectification efficiency.

$$\eta_{rectenna} = \eta_{ant}\eta_c\eta_d \tag{1.1}$$

The overall efficiency is the product of those components. For efficient AC to DC power

conversion, impedance matching is required to maximize power transfer (coupling efficiency) and ensure a low RC time constant (Grover and Moddel, 2011; Sanchez et al., 1978). Given the inherently capacitive structure of an MIM diode, and the tradeoff between resistance and capacitance for changing area, the fundamental cut-off frequency of a lumped-element MIM is in the low terahertz. Specifically, the coupling efficiency between a lumped-element MIM diode and an antenna can be calculated as follows:

$$\eta_c = \frac{4R_A R_D}{(R_A + R_D)^2 + (R_A R_D \omega C)^2} \tag{1.2}$$

In this equation, R_A is the antenna impedance, assuming the antenna reactance is negligible compared to the diode reactance. The diode resistance is R_D, ω is angular frequency, and C is the diode geometric capacitance.

$$C = \frac{\epsilon_0 \epsilon_r A}{d} \tag{1.3}$$

where A is the diode area, d is the insulator thickness, and ϵ_r is the relative dielectric constant. Using optimistic assumptions, $d = 3$ nm, $R_A = 100\ \Omega$, $R_D = 100\ \Omega$, $\epsilon_r = 8.5$ (NiO), and $A = (200\ \text{nm})^2$, I plot the coupling efficiency in Figure 1.4.

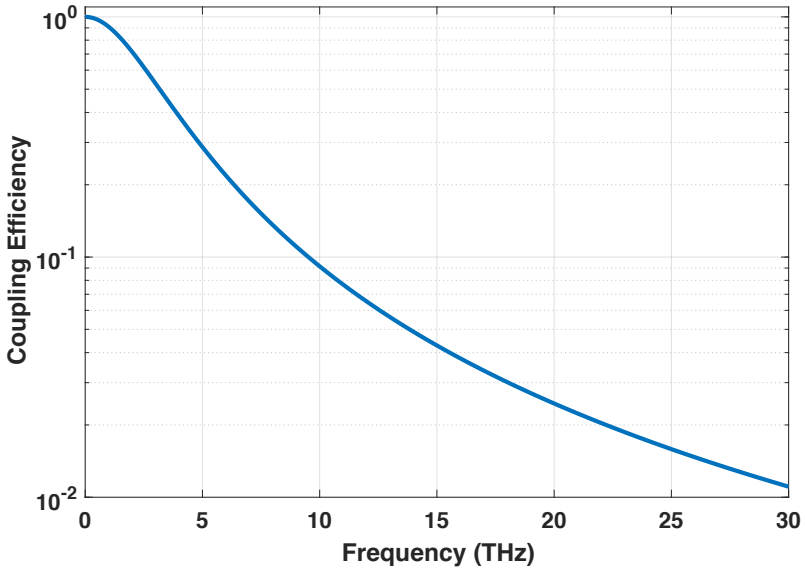

Figure 1.4: Coupling efficiency of lumped-element MIM diode

As Figure 1.4 shows, even with these optimistic assumptions, ignoring the antenna reactance and using a small-area 100 Ω diode, the coupling efficiency at 30 THz is only ∼1%. When antenna reactance is included, it can reduce the coupling efficiency by a factor of 10 or more.

1.3 Traveling-Wave Diodes

One proposed solution to overcome the RC time constant limitation is the traveling-wave diode (TWD) (Estes and Moddel, 2006). A TWD differs from a lumped-element rectenna primarily in the method it is fed from the antenna. In a lumped-element configuration, the diode is located at the feed-point of the antenna, where it receives a voltage signal uniformly across the diode as the signal from each antenna leaf enters from opposite sides of the diode. A TWD, on the other hand, requires a transition at the feed point of the antenna so that the signal from the antenna can couple to the MIM transmission line. This transition excites a surface plasmon mode at the MIM interface. In this way, the power from each antenna leaf propagates in the same direction away from the antenna feed-point and along the TWD. Figure 1.5 (b) shows the TWD extending perpendicular to the antenna axis from this transition region.

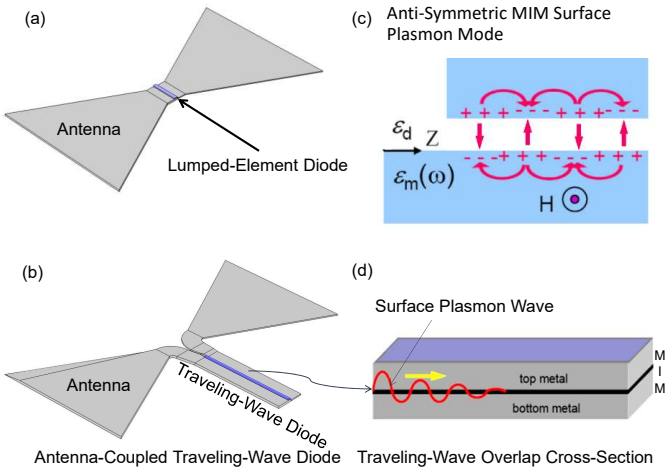

Figure 1.5: TWD vs lumped-element configuration.

In such a TWD configuration, the antenna excites a surface plasmon wave that travels down the line, as illustrated in 1.5 (c) and (d). I discuss coupled surface plasmon modes in detail in Chapter 5, Section 5.3. As the wave propagates, it is rectified by the MIM diode. Since the antenna is now loaded by a rectifying transmission line, the impedance seen by the antenna is the input impedance of the line, rather than the capacitive and resistive lumped-element MIM impedance. The TWD optical rectenna concept has been demonstrated experimentally in a waveguide-coupled configuration at 1.6 μm (Hobbs et al., 2007). Previously, the finite element method (FEM) was used to examine the effects of the cross-section geometry on the TWD rectenna performance with the assumption that the TWD length is much longer than the plasmonic decay length (Grover et al., 2010; Hashem et al., 2014; Sayed et al., 2015). In these cases, the nonlinear characteristic of the MIM junction cannot be included in the finite element analysis. In other work, the nonlinear $I(V)$ characteristic was included in a FDTD simulation examining a TWD for pulse detection (Lei and Van, 2013). In this thesis, I will discuss fabrication techniques, DC characterization, 3D FEM modeling with estimations for rectification, and experimental testing of the optical response of TWD rectennas at 10.6 μm.

Chapter 2

Fabrication

2.1 Available Fabrication Techniques

One important fabrication requirement for optical rectenna MIM diodes is a small area. For lumped-element diode rectennas, the small area is important for obtaining the low capacitance necessary for best-case coupling efficiency. TWD's require a small overlap (ideally < 100 nm) to have a good impedance match to the antenna, as shown by TWD modeling in Chapter 5. Because of this small area requirement, it is common for MIM optical rectennas to be built using either deep ultraviolet (DUV) lithography or electron beam (e-beam) lithography. The simplest way to form a small area MIM device using high-resolution lithography, is to use a simple overlap structure (Dagenais et al., 2010; Choi et al., 2011) depicted in Figure 2.1.

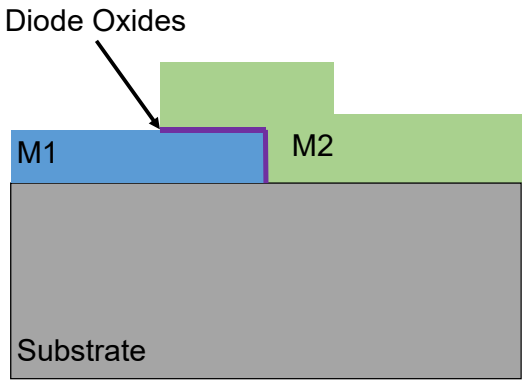

Figure 2.1: Overlap MIM diode fabrication.

In this overlap process, the first metal, M1, is patterned using liftoff. Then the diode oxides are either grown or deposited. Finally, the second metal, M2, is patterned by liftoff so that there is a small overlap region. Unfortunately, there are several prominent problems with this process. First, using liftoff to form the MIM junction can easily leave resist residue and disrupt the MIM tunneling characteristics. The common practice of removing resist residue with an O_2 plasma descum cannot be used with M2 in this process because the exposure to oxygen plasma will grow an uncontrolled diode oxide. Second, even if the resist residue problem is avoided (possibly by using an etchback process where metal is deposited everywhere before the lithography and etched to leave the desired pattern), when this type of overlap is formed, there is both surface and edge conduction, which limits the ability to control the diode characteristics as tunneling can vary greatly between the vertical edges and the horizontal surfaces. This variation is usually attributed to nonuniform oxide growth/deposition or the sharp corner in the middle of the junction formed by M1 at the transition between the vertical and horizontal surfaces. This sharp corner generally leads to enhanced fields in this area. The inability to distinguish surface and edge conductions disrupts the ability to engineer the desired MIM $I(V)$ characteristics.

The problems of the overlap diode can be avoided with techniques such as the pillar process shown in Figure 2.2. (Herner et al., 2017b,a). I have run and helped develop several similar processes. These types of processes require at least four lithographic steps, and relies on a DUV stepper to get small feature sizes ($\sim(300\text{ nm})^2$ diode area), and good alignment.

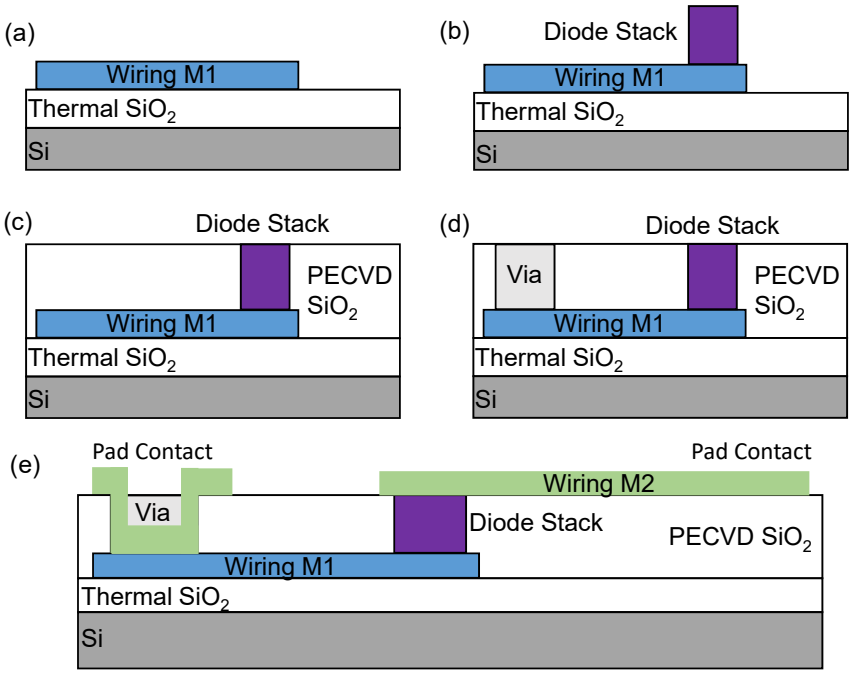

Figure 2.2: Pillar process MIM diode fabrication. (a) Wiring metal, M1, is patterned by liftoff. (b) the diode stack, including diode insulators, is deposited and patterned by etchback. The stack is capped in a refractory metal like Nb to provide a good chemical-mechanical polishing (CMP) stop. (c) The wafer is coated with SiO_2 by plasma enhanced chemical vapor deposition (PECVD). CMP planarizes the surface and exposes the top of the diode stack. (d) A large via is etched into the PECVD SiO_2 to allow electrical contact the wiring M1. (e) The second wiring metal, M2, is patterned by etchback.

While the pillar process can eliminate the problems associated with the overlap method, it comes at a cost of a substantially more complex fabrication procedure. The pillar process has three fundamental limitations that prevent me from using it to make TWDs. First, the minimum 248 nm stepper resolution is ~200 nm. From the TWD modeling in Chapter 5, this is larger than the desired MIM overlap. Second, the pillar process has slow turnaround. Given the experimental nature of MIM diodes, a process with fast turnaround provides the beneficial opportunity to experiment with different materials and oxide thicknesses. Finally, particularly in multi-user cleanroom facilities,

like the ones available to me, achieving repeatable and reliable fabrication results with many process steps often takes an extraordinary amount of development.

The germanium shadow mask (GSM) technique solves all three of these shortcomings. First, it utilizes a single lithography step, that is completed prior to any material depositions. This is ideal for experimenting with diode materials and oxide thicknesses. Second, it allows fabrication of feature sizes beyond the resolution of the lithography. This improved dimensional control is achieved by making use of a shadowing effects from suspended bridge and angled evaporations. This improved control comes at a cost of pattern fidelity for other geometry features. Finally, by employing a limited number of process steps, the GSM can achieve repeatable results with relative ease, even with a multi-user facility. The GSM process is described in detail in the following section.

Additionally, GSM does not reintroduce any of the problems found in the overlap technique. As soon as the diode MIM structure is deposited, no additional processing is required beyond an acetone bath for liftoff. This limits the possibilities for contamination of the MIM junction. The problems associated with edge conduction vs surface conduction are also avoided because angle depositions required by GSM form an MIM junction at an angle, that is neither strictly surface or edge. This angled junction also avoids the sharp corner found in the overlap process. I fabricated all of my devices using a germanium shadow mask (GSM) technique similar to (Hobbs et al., 2005, 2007; Bean et al., 2011). One major difference from this previous shadow mask work is that I adapted the process for use with a DUV 248 nm stepper rather than e-beam lithography. Using a stepper allowed me to build many identical die, which provided some additional advantages for optimizing the process, described in the following section.

2.2 Germanium Shadow Mask Process

I start with a 4 inch, high-resistivity, silicon wafer with a 300 nm layer of thermally grown SiO_2. I spin 4% polymethyl-methacrylate (PMMA) in anisole solution on to the wafer at a thickness of 260 nm. To ensure all the solvent is removed, I bake the wafer at 180° C for 15 minutes. Next, I cover the surface with 60 nm of evaporated germanium. The top view in the insert of Figure

2.3 shows the pattern printed on the surface with a ASML 5500 248 nm DUV stepper in the nanofabrication cleanroom at the University of California, Santa Barbara. This pattern is one representative geometry for a TWD rectenna with a bow-tie antenna and four-point probe leads connected at the end of the TWD. I used anti-reflective coating and UVN2300-.5 resist or UV210, depending on the tone of the reticle (I had reticles made with both tones). The stepper prints ~20 die (1-4 cm^2) on the wafer. Each die contains many TWDs with varying geometries, primarily variations in TWD length. I etch the pattern into the germanium with a CF_4 reactive ion etch and remove the under layer of PMMA with a O_2 plasma clean. The O_2 plasma is run at a relatively high pressure (~700 mT) to ensure the PMMA removal undercuts the Ge by at least a 0.5 μm. The insert in Figure 2.3 is a top view and shows the location of the cross-section illustrated in the main portion of the figure. The cross-section shows the resulting structure has a suspended Ge bridge that is supported by PMMA in/out of the plane of the cross-section. The bridge length defines the TWD length for the different devices in the die and ranges from 1 to 3 μm.

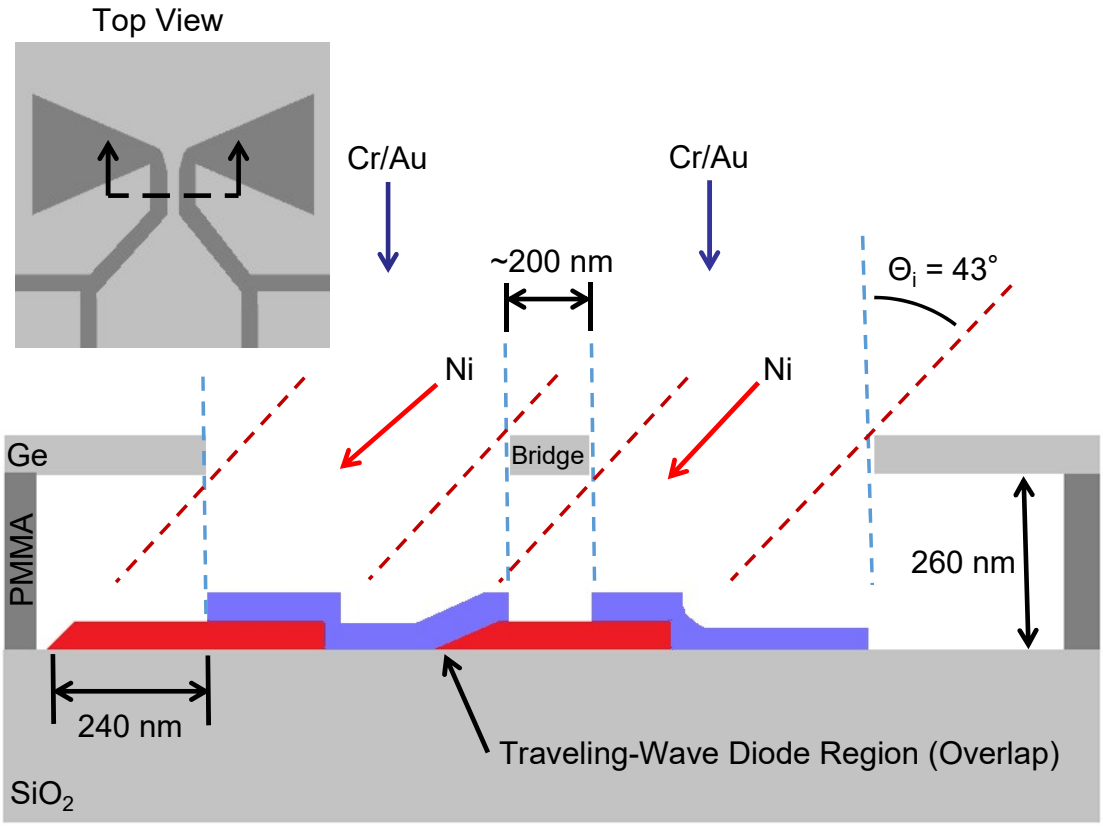

Figure 2.3: TWD fabrication with germanium shadow mask.

While the GSM supports fabrication of many different MIM material sets, I will focus on the one I found to be the most reliable, Ni-NiO(∼3 nm)-Nb_2O_5(∼2 nm)-Cr/Au. Prior to diode material deposition, the 4 inch wafer is diced into individual die (∼1-4 cm^2), as each die contains plenty of devices (∼50) for testing. After the wafer is diced, immediately prior to the first metal deposition, an additional 30 second O_2 plasma clean is performed to ensure the substrate is free of organic contaminates. Then, Ni (M1) is thermally evaporated at an angle, $\Theta_i = 43°$, from the right. Depending on the specific PMMA thickness, Ge bridge width, and desired overlap, the ideal angle for deposition can vary. However, since there are multiple die, corrections to deposition angle can be made on subsequent die to achieve the desired overlap. This is one of the biggest advantages of patterning with a DUV stepper rather than e-beam lithography.

After the nickel is deposited, a nickel oxide is grown in an O_2 plasma (30 W, 50 mT, 30-60 s)

to a thickness of ∼3 nm. Then Nb_2O_5 is DC reactively sputter deposited (60 W, 2.5 mT, 60-100 s) from a Nb target in an O_2/Ar plasma to a thickness of ∼2 nm. To complete the MIM junction, a 3 nm layer of Cr and a 30 nm layer of Au are evaporated at normal incidence. Finally, excess material is lifted off in an acetone bath. The thin Cr layer forms a good barrier for an asymmetric $I(V)$ characteristic. The thick Au improves the plasmonic propagation characteristics of the TWD.

In order to have good control of the overlap dimension, I need tight control over the deposition angle relative to the wafer. Figure 2.4 shows how I used a self-leveling laser to accurate measure the angle of the metal deposition, Θ_i.

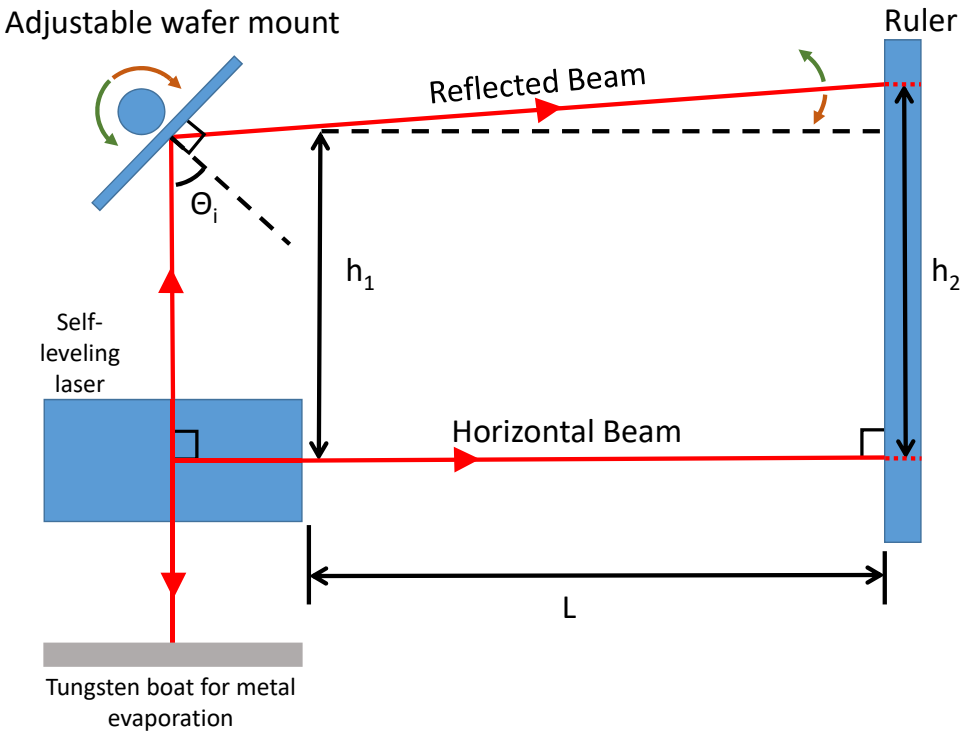

Figure 2.4: Evaporation angle measurement.

The self-leveling laser emitted a level and plumb laser beams. The beam from the bottom of the laser aligns the laser to the metal source. The horizontal beam is directed at a ruler mounted

to a wall ∼2 m away. The beam from the top of the laser reflects off the sample, which is mounted at an angle, toward the wall-mounted ruler. The sample holder is mounted on a round rod, and can be rotated to adjusted the angle of incidence, θ_i. As the wafer mounted is rotated clockwise (counter-clockwise), θ_i and h_2 decreases (increases). Using the height difference from horizontal source beam and the reflected beam from the wafer, I calculated the metal incident angle relative to the normal of the wafer using the following equation:

$$\Theta_i = \frac{90^\circ + arctan(\frac{h_2 - h_1}{L})}{2} \tag{2.1}$$

For $L = 1760$ mm, a 5 mm difference in the h_1 and h_2 gives a change in θ_i of approximately 0.1° (near $\theta_i = 45^\circ$). With a PMMA thickness of 260 nm, this corresponds to theoretical overlap control of ∼1 nm. In practice, the control is not that good because of slight variations in PMMA thickness and bridge width. In some cases, we managed to push the overlap dimension to ∼20-30 nm as shown by the transmission electron micrograph (TEM) in Figure 2.5.

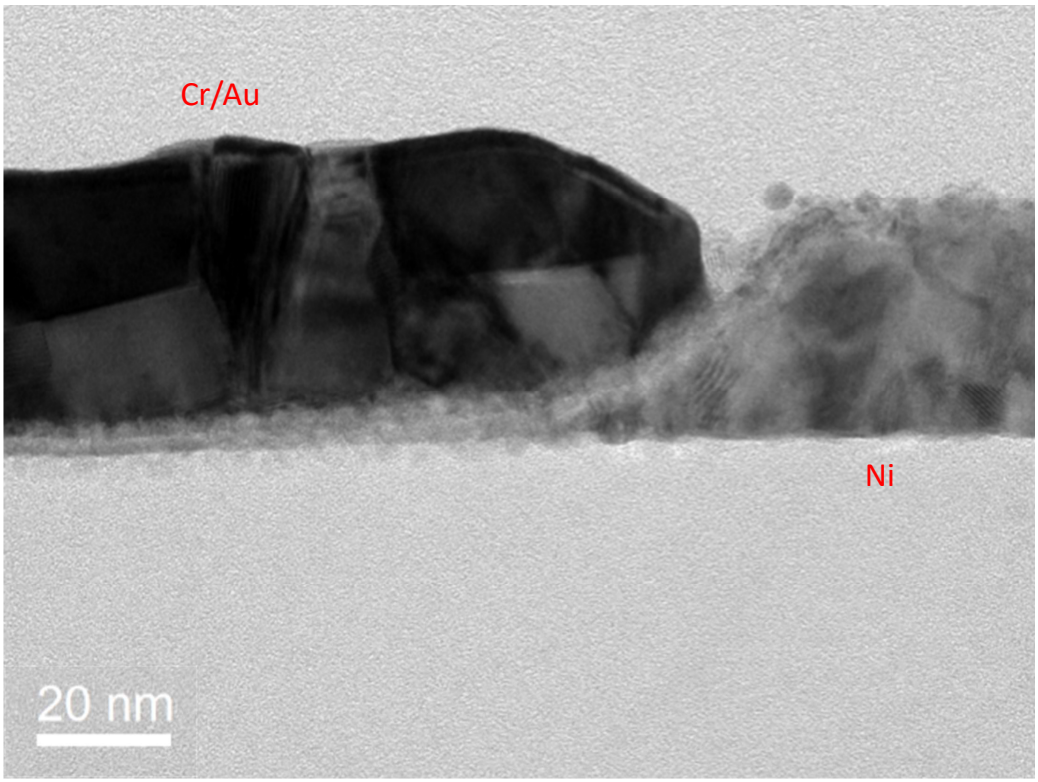

Figure 2.5: TEM of MIM junction with ∼20 nm overlap. Fabrication by Ayendra Weerakkody.

While hundreds of TWDs were fabricated (and characterized by DC $I(V)$ measurement) and ∼50 were measured for infrared optical response, I will focus on five devices for full analysis: a lumped-element rectenna for reference, TWD1 (3 μm), TWD2 (1.5 μm), TWD3 (1.35 μm), and TWD4 (∼1.0 μm). All five devices are Ni-NiO-Nb_2O_5-Cr/Au material set with an estimated 3 nm NiO and 2 nm Nb_2O_5. This material set proved to have the most reliable $I(V)$ characteristics, but we used the GSM to explore many other material combinations including:

(1) Ni-NiO-Ni
(2) Ni-NiO-Pt
(3) Ni-NiO-Nb_2O_5-Ni
(4) Ni-NiO-Nb_2O_5-Al
(5) Ni-NiO-Nb_2O_5-Nb
(6) Ni-NiO-Ta_2O_5-Ta
(7) Ni-NiO-TiO_2-Ti
(8) Ni-NiO-TiO_2-Cr
(9) Ni-NiO-ZnO-Ti

(10) Ni-NiO-ZnO-Cr

(11) Co-CoO_x-TiO_2-Ti

(12) Co-CoO_x-TiO_2-Cr

(13) Ni-NiO-Al_2O_3-Cr

Despite all the benefits, the GSM is not without drawbacks. First, and fundamentally, GSM requires directional metal depositions. This limits the metal choices to only the ones that can be evaporated. Second, there is a cost to achieving dimensional control of the MIM junction beyond the resolution of the lithography. That is, other features become distorted due to the relative displacement of subsequent layers from the angle depositions. This distortion is seen clearly in all of the SEM images in Chapter 4. The final limitation is based on the specific equipment available to me. Since our oxides are deposited or grown in a sputter system, which is separate from the evaporator, the MIM diodes cannot be deposited in-situ. The time of junction exposure to atmosphere is limited to several minutes, however, depositing in-situ would still be the preferred method. To build MIM diodes with GSM in-situ, specialty equipment that can evaporate metals, deposit and grow oxides, and control the angle of the wafer relative to evaporation sources, all without breaking vacuum, would be required. Even with the consideration of its limitations, GSM is the best option for fabricating TWDs.

Chapter 3

Exponential Fitting

3.1 Importance of $I(V)$ Curve Fitting

Measuring the DC $I(V)$ characteristic of fabricated MIM diodes is the first step in experimentally analyzing and testing an optical rectenna. From the DC $I(V)$ characteristics, certain performance metrics, such as differential resistance, responsivity, and asymmetry, given in Eqs. 3.1, 3.2, and 3.3 respectively, can be extracted. Two of these three metrics require differentiation, indicted by the primes in the equations. These metrics describe properties that are central in assessing a diode's suitability for use in an optical rectenna.

$$R_d(V) = I'(V)^{-1} \tag{3.1}$$

$$\beta(V) = \frac{1}{2}\frac{I''(V)}{I'(V)} \tag{3.2}$$

$$A(V) = -\frac{I(V)}{I(-V)} \tag{3.3}$$

For an efficient rectenna, a high coupling efficiency between the MIM diode and the antenna is required. The antenna impedance is typically on the order of 100 ohms, and for efficient power transfer the diode resistance should match it (Sanchez et al., 1978; Grover and Moddel, 2011). For this reason, only diodes that have a relatively low resistance are of interest, despite the higher asymmetry and nonlinearity seen in some high-resistance diodes (Weerakkody et al., 2015; Maraghechi

et al., 2011, 2012; Herner et al., 2017a). A high diode responsivity, which is a measure of rectified DC voltage or current as a function of input power, and a large asymmetry, which is the ratio of forward to reverse current, are required for efficient rectification (Grover and Moddel, 2011). Since optical rectennas usually operate at voltages close to zero (Joshi and Moddel, 2015), we use the zero-bias resistance, $R_0 = R_d(0)$, and the zero-bias responsivity, $\beta_0 = \beta(0)$, when analyzing our diodes. Using zero-bias values simplifies the differential resistance and responsivity curves into single quantitative metrics.

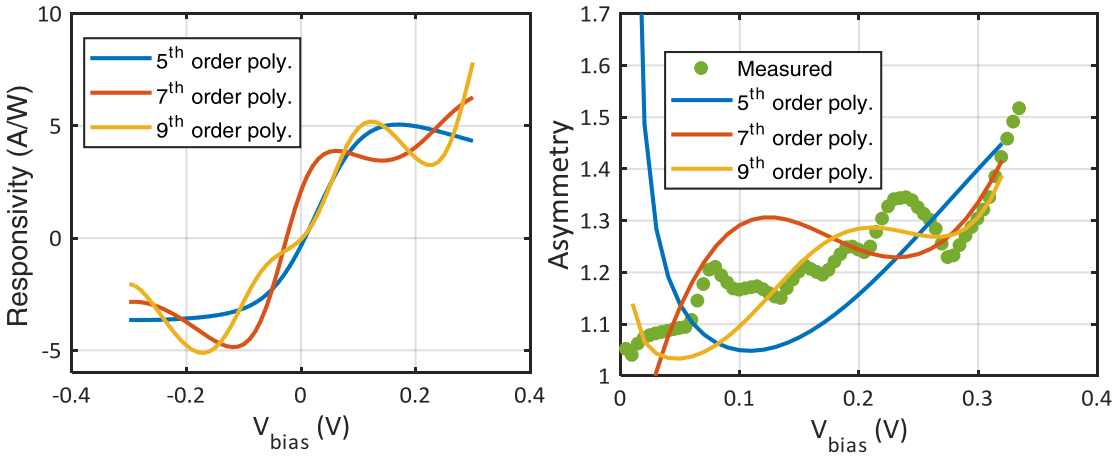

Figure 3.1: **Effects of polynomial fitting order on a moderate-resistance diode (MIM-1) (a)** responsivity as a function of voltage **(b)** asymmetry as a function of voltage.

While $R_d(V)$ and $\beta(V)$ can be calculated directly from $I(V)$ data using central difference approximation derivatives, a problem often arises when noise in the experimental data gets amplified by the derivatives. To overcome this noise amplification, it is necessary to use some sort of fitting or smoothing. A polynomial fit using least square regression is an attractive option because it is easy to differentiate and integrate, and a polynomial of high enough order can fit any curve to an arbitrarily high degree of accuracy. This arbitrarily high degree of fit accuracy, however, can give misleading results. Runge's function is one well-established example (Forsythe et al., 1977; Kreyszig, 2006). Despite the known problems with polynomial fitting, it has become common practice to fit MIM $I(V)$ data with a polynomial when analyzing MIM diodes (Ozkan et al., 2016;

Bean et al., 2009, 2011; Dodd et al., 2015; Dagenais et al., 2010; Choi et al., 2009, 2010; Gadalla et al., 2014; Sabaawi et al., 2013; Herner et al., 2017b). In this paper we expose the shortcomings of the polynomial fit for MIM diodes through the analysis of a double insulator MIM diodes. We demonstrate that an alternative fitting procedure can overcome these shortcomings.

The first diode we examine, MIM-1 ($R_d(0) \cong 16$ kΩ), is a Co-CoO_x-TiO_2-Ti double insulator MIM diode fabricated as described in Herner (Herner et al., 2017b). We fit the measured $I(V)$ data for MIM-1 with 5^{th}, 7^{th}, and 9^{th} order polynomials. These fits generate smooth responsivity curves shown in Figure 3.1 (a). However, these responsivity curves vary greatly between the different fit orders, which is evidence that these results are misleading. The asymmetry curves in Figure 3.1 (b) also show substantial variation, not only from each other, but from the data. Unlike $R_d(V)$ or $\beta(V)$, the asymmetry does not rely on $I(V)$ derivatives, and so it can be calculated directly from the interpolated $I(V)$ data. The interpolation is necessary to ensure that the currents at both the positive and negative voltage are taken at a uniform voltage distance from $V = 0$. Even though the asymmetry can be calculated from the data directly, the noise of the measurement is still clearly evident, which again demonstrates the need for quality fitting. These curves show that the polynomial fits do a particularly poor job of estimating the asymmetry at low voltages. Because of these erroneous results, we developed an alternative, more robust fitting model.

3.2 The Exponential Fit Performance Metrics

The electron tunneling responsible for the rectification in MIM diodes is fundamentally an exponential process (Simmons, 1963). To overcome limitations of the polynomial fit, we propose an alternative approach using least square regression to fit an equation based on exponentials. This fit facilitates an understanding of how well the diode will operate in a circuit (e.g., in a rectenna,) and provides a useful basis for diode improvement. The proposed exponential-based fit is:

$$I(V) = ae^{bV} + ce^{dV} = I_0(e^{bV} - e^{-dV}) \tag{3.4}$$

In practice, we use the first version of the equation to perform the fit as it is a convenient MATLAB built-in fitting function, 'exp2'. After the fit is complete, we check that the variation between a and c is less than 1% and set I_0 to the average of a and c and force the sign conventions in the second version of the equation. In this equation, parameter b strongly influences the $I(V)$ at positive voltages while parameter d affects the curve at negative voltages. The parameter I_0 scales the curve, thus modifying the diode resistance. The first indication that Eq. 3.4 is an appropriate form for a diode fit is that when $d = 0$ and $b = \frac{1}{nv_t}$, where n is an ideality factor and v_t is the thermal voltage, the equation simplifies to the Shockley diode equation, which describes an ideal semiconductor diode (Shockley, 1949). Simmons proposed a similar exponential form for a trapezoidal high-barrier diode (Simmons, 1963). We note that Simmon's equation does not describe our MIM diodes accurately because for low-barrier height MIM diodes at intermediate voltages (100 mV $\leq$ $V \leq$ 300 mV), the equation simplifies to a symmetric $I(V)$ formula and overestimates the tunnel current (Grover and Moddel, 2012). In contrast to the polynomial fits, when the exponential fit is used the resistance, responsivity, and asymmetry are directly determined by the fitting coefficients in a physically meaningful way. In this paper, we calculate resistance, responsivity and asymmetry for two MIM diodes of different material sets that were fabricated by different techniques. These different diodes show slightly different $I(V)$ curvature and fitting techniques. We demonstrate that the exponential fitting is a superior alternative to the polynomial fit.

3.2.1 Resistance

To effectively match the diode resistance, R_d, to the antenna, it is necessary to understand the relationship between the diode $I(V)$ and $R_d(V)$. Substituting the exponential equation for the diode $I(V)$, Eq. 3.4, into the diode differential resistance equation, Eq. 3.1, results in:

$$R_d(V) = \frac{1}{I_0(b\exp(bV) + d\exp(-dV))} \tag{3.5}$$

From Eq. 3.5, we can calculate the zero-bias differential resistance R_0. At $V = 0$, the exponential terms vanish and R_0 can be expressed simply as:

$$R_0 = \frac{1}{I_0(b+d)} \tag{3.6}$$

3.2.2 Responsivity

Since responsivity provides the connection between optical input power and DC output, it is useful to understand the relationship between the $I(V)$ and $\beta(V)$. Substituting the exponential $I(V)$ equation, Eq. 3.4, into Eq. 3.2, we obtain the voltage-dependent responsivity:

$$\beta(V) = \frac{1}{2}\left(\frac{b^2\exp(bV) - d^2\exp(-dV)}{b\exp(bV) + d\exp(-dV)}\right) \tag{3.7}$$

Just as with resistance, the first parameter of interest is the zero-bias responsivity, since we are often interested in rectenna operation at or near zero bias. The responsivity at zero bias is:

$$\beta_0 = \frac{1}{2}(b-d) \tag{3.8}$$

Zero-bias responsivity is dependent only on the two coefficients in the arguments of the exponentials in Eq. 3.4. From Eq. 3.4 we can see that at large voltage magnitudes, one exponential dominates the $I(V)$ equation. Similarly, from Eq. 3.7, we see that at large positive voltages $\beta(V)$ asymptotically approaches $\frac{1}{2}b$ and at large negative voltages $\beta(V)$ approaches $-\frac{1}{2}d$.

3.2.3 Asymmetry

The asymmetry gives insight into a diode's ability to efficiently rectify. Again, substituting Eq. 3.4 into Eq. 3.3 and simplifying gives the voltage dependent asymmetry:

$$A(V) = e^{(b-d)V} = e^{2\beta_0 V} \tag{3.9}$$

This asymmetry equation is rewritten in terms of β_0 using Eq. 3.8, thus showing a direct correspondence between the diode asymmetry and zero-bias responsivity.

3.3 Exponential Fit

Our interest in relatively low resistance diodes (Grover and Moddel, 2012) dictates that the MIM insulators be thin (<5 nm). Thus, the maximum measured voltage range for our diodes, to avoid dielectric breakdown, is the on the order of several hundred millivolts. For MIM-1, the exponential fit coefficients are as follows: $I_0 = 3.3 \times 10^{-6}$ A, $b = 10.0\ V^{-1}$ and $d = 8.9\ V^{-1}$. Using Eq. 3.6 and Eq. 3.8, these coefficient values correspond to a $\beta_0 = 0.55$ A/W and a $R_0 = 16$ kΩ. The quality of the fit is assessed in two ways: First, the fit residue, which is calculated from the $I(V)$ data minus the $I(V)$ fit, indicates how well the model fits the data. Second, comparing the fit asymmetry to the interpolated data asymmetry shows how closely the model estimates performance metrics.

For MIM-1, the exponential fit is of similar quality to the polynomial fit. In Figure 3.2 (a), the three polynomials (5^{th},7^{th}, and 9^{th} order fits) and exponential $I(V)$ curves are all nearly indistinguishable from the data and each other. A closer look at the fit quality in Figure 3.2 (b) reveals that all fits have comparably low residues. However, as shown earlier, changing the order of the polynomial fit results in a wide range of responsivity curves. Figure 3.2 (c) shows the exponential fit responsivity curve overlaid on Figure 3.1 (a), the polynomial fits responsivity curves. Figure 3.2 (d) shows the exponential fit asymmetry overlaid on the polynomial and interpolated data asymmetry from Figure 3.1 (b). Clearly, the exponential fit does a superior job of representing the diode asymmetry.

The second diode examined is a Ni-NiO-TiO_2-Cr double insulator diode, MIM-2. MIM-2 ($R_d(0) \cong 4$ kΩ) has a lower resistance than MIM-1 and was fabricated with a shadow-mask technique discussed in Chapter 2. Diodes with lower resistances often suffer less variation between different polynomial fit orders, but even when the polynomial fits are well behaved, the resulting polynomial equation fails to provide the same connection among diode properties that the exponential fit provides.

We now repeat the fitting procedure for MIM-2, comparing the exponential model to the

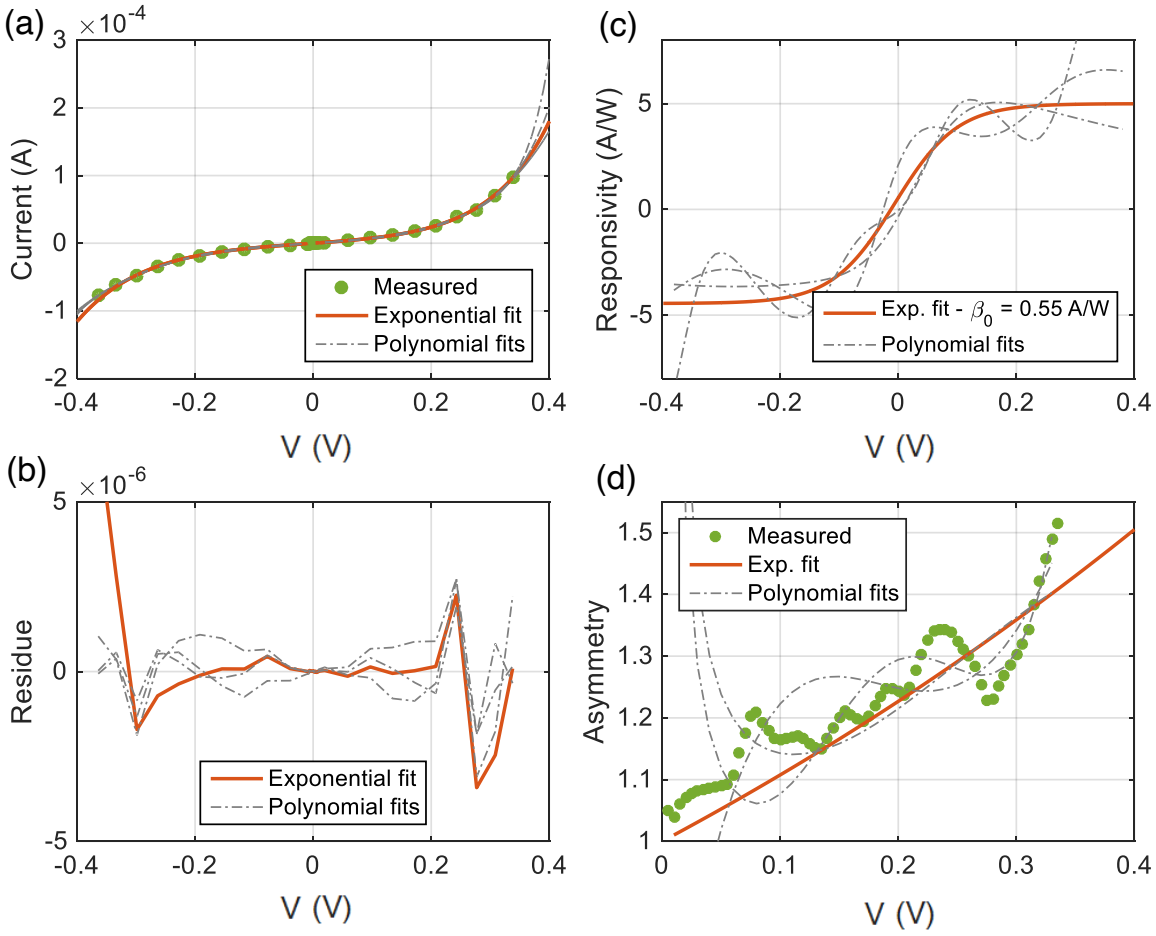

Figure 3.2: **Comparison of 5^{th}, 7^{th}, and 9^{th} order polynomial fits (dashed grey, labeled in Figure 1) and exponential fit (solid orange, $I_0 = 3.3 \times 10^{-6}$ A, $b = 10.0\ V^{-1}$ and $d = 8.9\ V^{-1}$) for MIM-1 ($R_d(0) \cong 16$ kΩ). (a)** Measured diode DC $I(V)$ characteristics (green circles) and $I(V)$ fits versus voltage, V. **(b)** Calculated fit residue. **(c)** Calculated fit responsivity. **(d)** Calculated fit asymmetry and interpolated data asymmetry (green circles).

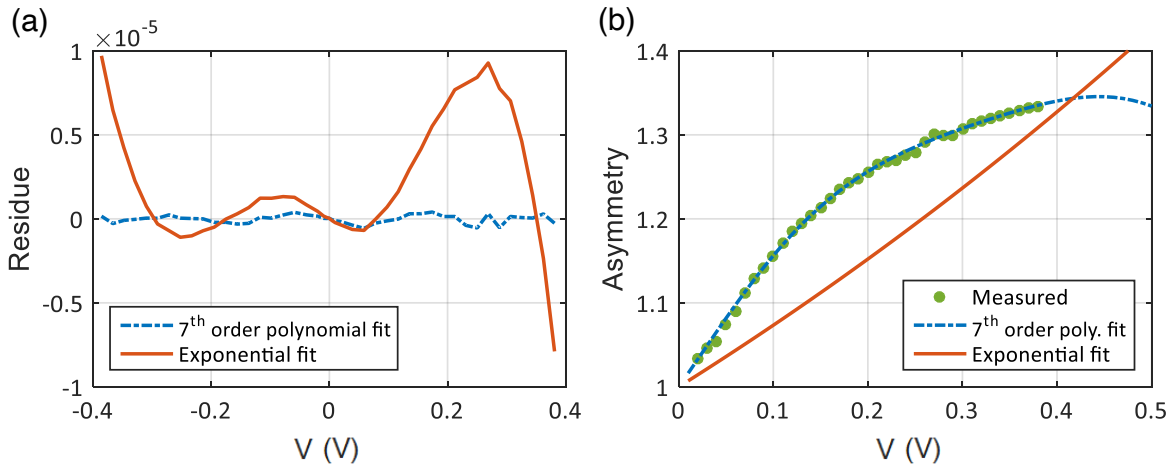

Figure 3.3: **Comparison of 7^{th} order polynomial fit (dashed blue) and exponential fit (solid orange, $I_0 = 2.65 \times 10^{-5}$ A, $b = 5.53\ V^{-1}$ and $d = 4.82\ V^{-1}$) for MIM-2. (a)** Calculated fit residue. **(b)** Calculated fit asymmetry and interpolated data asymmetry (green circles).

7^{th} order polynomial fit. Just as with MIM-1, both the 7^{th} order polynomial and exponential fits are nearly indistinguishable from the raw $I(V)$ data, and therefore are not shown. Unlike MIM-1, however, once we examine the residue plot, Figure 3.3 (a), we can see that the exponential fit is substantially less accurate than the polynomial, especially at higher voltage magnitudes. The exponential fit tends to overstate the magnitude of the current at higher voltages. This systematic error corresponds to a curvature of the $I(V)$ data that does not increase with voltage as quickly as the fit does. The fundamental nature of the exponential model does not allow for this reduction in curvature because away from $V = 0$, only one of the exponential terms in Eq. 3.4 dominates. One physical explanation of this reduced curvature of the $I(V)$ is an unaccounted for series resistance. This series resistance also accounts for the flattening of the asymmetry curve in Figure 3.1 (b), rather than the unbounded exponential growth predicted by Eq. 3.9.

A small portion of the resistance is due to the inability, in practice, to remove 100% of the parasitic lead resistance even with 4-point probe measurements, while the remainder is associated with the MIM diode junction itself. In Fowler-Nordhiem tunneling, electrons are transported through the dielectric barrier partially by tunneling, and partially by conduction in the conduction band of the insulator (Sze and Ng, 1981). This transport through the conduction band adds to the series resistance. The distance an electron travels in the conduction band depends on the insulator thickness and the energy band structure, which changes for different voltages. Therefore, the series resistance depends on the voltage, V. To fit this adequately while avoiding unnecessary complexity, we choose the simplest form that meets the physical requirements for this voltage-dependent series resistance: 1) resistance is always positive, and 2) it has a continuous first derivative. Thus, the voltage-dependent series resistance, R_v, is approximated as follows:

$$R_v(V) = R_s + \alpha V^2 \tag{3.10}$$

Where R_s is the constant portion of the series resistance, and α is the coefficient for the voltage-dependent portion. The relatively low zero-bias resistance of MIM-2 makes the inclusion of this additional voltage-dependent series resistance necessary for an accurate fit, unlike for MIM-1 where

the diode resistance was large enough that the series resistance was negligible.

3.4 Modified Exponential Fit

Previously, when Eq. 3.4 described the diode $I(V)$, it was unnecessary to distinguish between the voltage on the diode, V_D and the measured voltage, V, as $V_D = V$. With the addition of a series resistance, R_v, there is a third voltage to consider, the resistor voltage, V_R. The voltage, which is measured over the diode and resistor series combination, can be separated into two components:

$$V = V_D + V_R \tag{3.11}$$

The diode voltage, V_D, from Eq. 3.11 can be expressed in another form:

$$V_D = V - R_v(V)I \tag{3.12}$$

where V_D is the diode voltage, and $R_v(V)I$ gives the voltage across the voltage-dependent series resistor. Even though we are now including a series resistance in our analysis, the diode $I(V)$ data is still represented by Eq. 3.4, which can be rewritten to clarify which voltage the $I(V)$ relationship applies to:

$$I(V_D) = I_0(e^{bV_D} - e^{-dV_D}) \tag{3.13}$$

The relationship between the measured current, $I(V)$ and the measured voltage, V, can be found by substituting Eq. 3.12 into Eq. 3.13 for V_D and is described by:

$$I(V) = I_0(e^{b(V-I(V)R_v(V))} - e^{-d(V-I(V)R_v(V))}) \tag{3.14}$$

Since the current in Eq. 3.14 is recursive, the fit coefficients cannot be obtained through least squares regression as done for Eq. 3.4 in Section 3.3. However, with the addition of a few preliminary data manipulation steps, and a comparison of a series of least squares regression fits, we can solve for the five coefficients (R_s, α, b, d, and I_0). Appendix A explains this procedure in detail.

To compare the results of the modified exponential fit with the unmodified version, we plot $I(V)$'s, residues, responsivities and asymmetries. Figure 3.4 (a) shows that for the data, the unmodified exponential fit, and the series resistance exponential fit are all indistinguishable in the $I(V)$ plot. Figure 3.4 (b) present the fit residue for the exponential and the modified exponential fits. This shows that the addition of the series resistance improves the fit, compared to a simple exponential without an additional resistance. Figure 3.4 (c) shows the responsivity of both exponential fits, and that, as expected, the addition of the series resistance reduces the curvature of the the $I(V)$ at higher voltages. Finally, Figure 3.4 (d) shows the asymmetry for both exponentials with the interpolated asymmetry data. Clearly, the exponential with the series resistance does a much more accurate job of representing the asymmetry than the unmodified exponential.

Just as we did for the fit without the series resistance, we want to determine the relationship between our model and the diode performance metrics. Because of the complex relationship between I and V in Eq. 3.14, there are not useful analytic expressions for voltage-dependent diode resistance, responsivity or asymmetry. However, we can find expressions for zero-bias resistance and responsivity, because those complex voltage dependent expressions simplify at $V = 0\,V$.

3.4.1 Zero-Bias Resistance

The diode resistance is simply the series combination of a resistor and the exponential resistance in Eq. 3.5. At $V = 0$, the voltage-dependent resistance part of R_v vanishes and leaves only R_s. Thus the zero-bias resistance can be expressed as follows:

$$R_0 = \frac{1}{I_0(b+d)} + R_s = R_0^{exp} + R_s \tag{3.15}$$

If we refer to the resistance in Eq. 3.6 as R_0^{exp}, we get the second form, where we see the zero-bias resistance is the sum of the constant portion of the series resistance and the zero-bias resistance from the unmodified exponential. Using Eq. 3.15 for MIM-2 fitting results gives $R_0 = 4.1\ \mathrm{k\Omega}$.

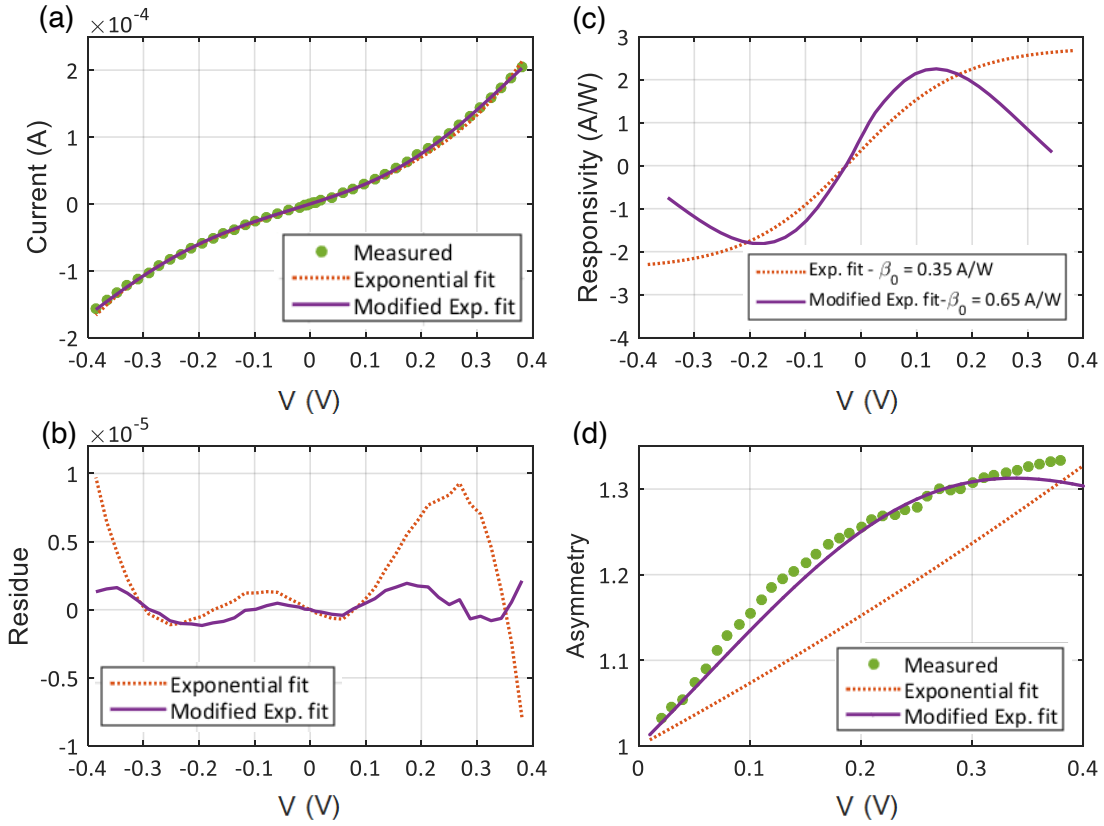

Figure 3.4: **Comparison of exponential (orange dots, with Eq. 3.4 parameters $I_0 = 2.65 \times 10^{-5}$ A, $b = 5.53\ V^{-1}$ and $d = 4.82\ V^{-1}$) and modified exponential (solid purple, $I_0 = 1.83 \times 10^{-5}$ A, $b = 8.64\ V^{-1}$, $d = 7.07\ V^{-1}$, $R_s = 334\ \Omega$ and $\alpha = 1125\ \Omega/V^2$) fits for MIM-2 ($R_d(0) \cong 4$ kΩ). (a)** Measured diode DC $I(V)$ characteristics (green circles) and $I(V)$ fits versus voltage, V. **(b)** Calculated fit residue. **(c)** Calculated fit responsivity. **(d)** Calculated fit asymmetry and interpolated data asymmetry (green circles).

3.4.2 Zero-Bias Responsivity

While the complexity of Eq. 3.14 leads to a voltage-dependent responsivity that provides little insight into the diode characteristics, the responsivity at zero-bias can be calculated as:

$$\beta_0 = \frac{1}{2}(b-d)\left(\frac{1}{1+R_s I_0(b+d)}\right)^2 \tag{3.16}$$

Using Eq. 3.16 for MIM-2, we find $\beta_0 = 0.65$ A/W. If we refer to the responsivity in Eq. 3.8 as β_0^{exp}, Eq. 3.16 simplifies to the following:

$$\beta_0 = \beta_0^{exp}\left(\frac{1}{1+R_s/R_0^{exp}}\right)^2 \tag{3.17}$$

As R_s gets large relative to R_0^{exp}, the zero-bias responsivity is reduced relative to β_0^{exp}. Of course, if $R_s = 0\ \Omega$, then $\beta_0 = \beta_0^{exp}$.

3.5 Fitting Conclusion

Inaccurate fitting of fabricated MIM didoes can lead to erroneous analyses of a diode's $I(V)$ characteristics and its performance metrics. We found that polynomial fitting can misstate responsivity and asymmetry values, two of the main metrics used to assess the performance of diodes in optical rectennas. Using the wrong order polynomial fit for a high resistance diode can drastically affect the resulting responsivity curve, and could even result in mislabeling the forward direction of the diode. Here, we have presented an exponential fitting method as an alternative to the commonly used polynomial fitting procedure. The exponential fit provides several advantages in analyzing MIM diodes such as fewer fitting parameters and a simple relationship between the fitting parameters and the diode performance metrics, while requiring a more complex fitting strategy. One example of the relationships provided is that the diode asymmetry is directly linked to the zero-bias responsivity. Another is a simple function relationship showing how series resistance degrades responsivity. This exponential model can be used to develop a broader understanding of MIM diode $I(V)$ characteristics, and the connections between performance metrics.

We have analyzed the exponential fit for two diodes, one with high resistance and one with low resistance. For the low resistance diode, an additional voltage-dependent series resistance was

necessary to get an accurate fit. The high resistance diode can be fit by either the modified or unmodified exponential fit and achieve the same results. The addition of these exponential fitting procedures to existing analysis techniques will help avoid potentially misleading results, and give added confidence to derived performance metrics.

Chapter 4

Characterization: DC Measurement and Device Imaging

After fabrication is complete, DC measurements provide valuable feedback on the quality of the MIM junction. I make an $I(V)$ measurement to get an accurate characterization of the junction nonlinearity and asymmetry. All the devices are fabricated with four-point probe contacts so the junction can be measured in isolation from contact and lead resistance. I use a Kiethley 2602 source meter to provide the source current and a HP 3478A multimeter to measure the sense voltage. A mercury switch shorts all four probes together during probe manipulation to prevent static discharge from damaging the MIM junction. Using the method described in Chapter 3, I fit the data to determine the diode differential resistance, responsivity and asymmetry. I use zero-bias responsivity, β_0, and zero-bias resistance, R_0, as comparison metrics to determine which devices are most promising for 10.6 μm (28 THz) measurement. At higher frequencies (or lower illumination intensities), as the photon energy becomes large compared AC voltage from the antenna, a quantum analysis is necessary (Joshi, 2015). Using high resolution imaging such as scanning electron micrography (SEM) and transmission electron micrography (TEM), I made measurements of device dimensions so experimental results can be compared to modeled TWD performance.

4.1 Example TWD TEM

Since TEM is costly and destructive to the device being imaged, it was preformed only on representative TWDs, similar to the ones that were measured. Figure 4.1 shows TEM results for a

TWD with an 80 nm overlap.

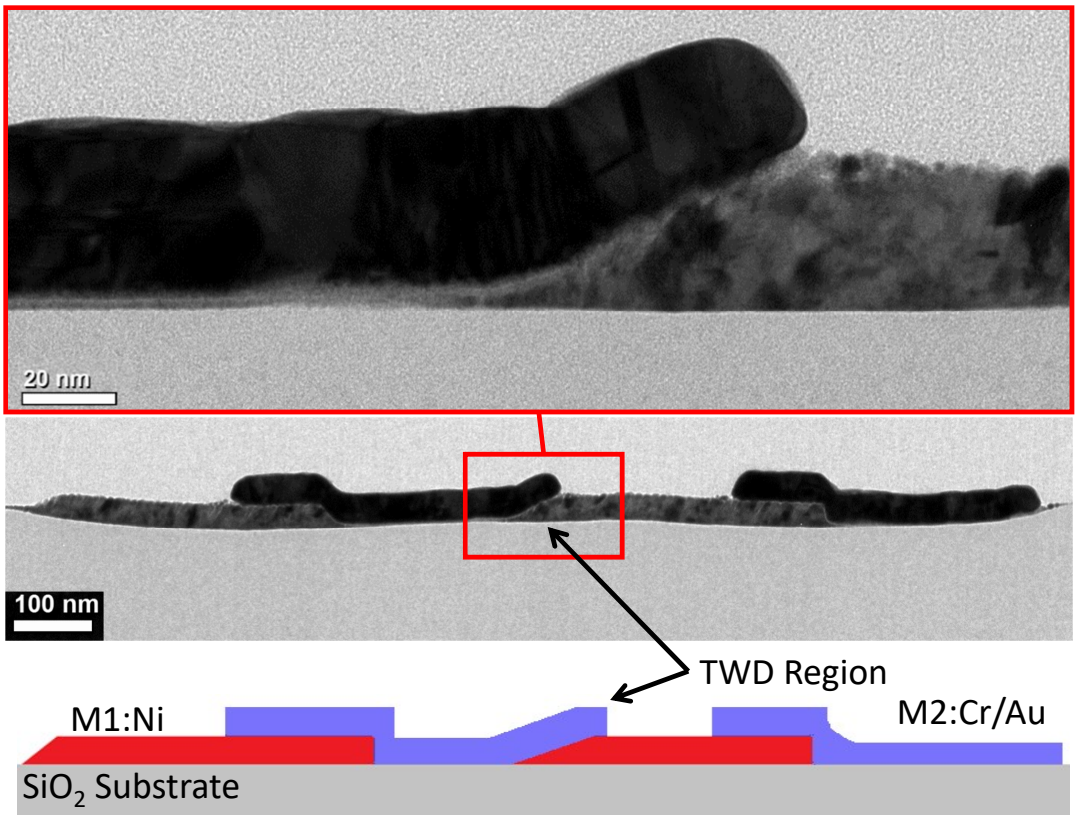

Figure 4.1: Representative TEM of a GSM fabricated TWD

As predicted by the illustration of the GSM process in Figure 2.3, there are seven regions across the cross-section of the TWD: two regions with just M1, two regions with just M2, and three regions with both M1 and M2. The middle region forms the TWD MIM junction. As expected, the junction forms at an angle due to the angled metal depositions. This prevents the problems shown in Figure 2.1 where the overlap junction has surface and edge conduction as well as a sharp metal corner in the middle of the junction. This particular device has an overlap of ~80 nm. Even in the TEM, the NiO is nearly indistinguishable from the Nb_2O_5, but the total insulator (bright white between the two metals) thickness can be estimated at ~5 nm.

4.2 Lumped-Element Diode

To completely analyze the benefits of a TWD, we built a lumped-element rectenna as a control device for optical testing and comparison. This device, having a slightly larger Ge bridge width, required two angle depositions to achieve an overlap. Figure 4.2 shows an SEM of the lumped-element rectenna. The four leads for the four-point measurement are visible, two to each end of the bow-tie antenna. The distortion due to the angle evaporation is visible. The dull gray found near the left boundaries of the structure is the Ni. The large area very bright regions are Ni/Cr/Au, and the medium bright areas at the right boundaries of the structure are Cr/Au.

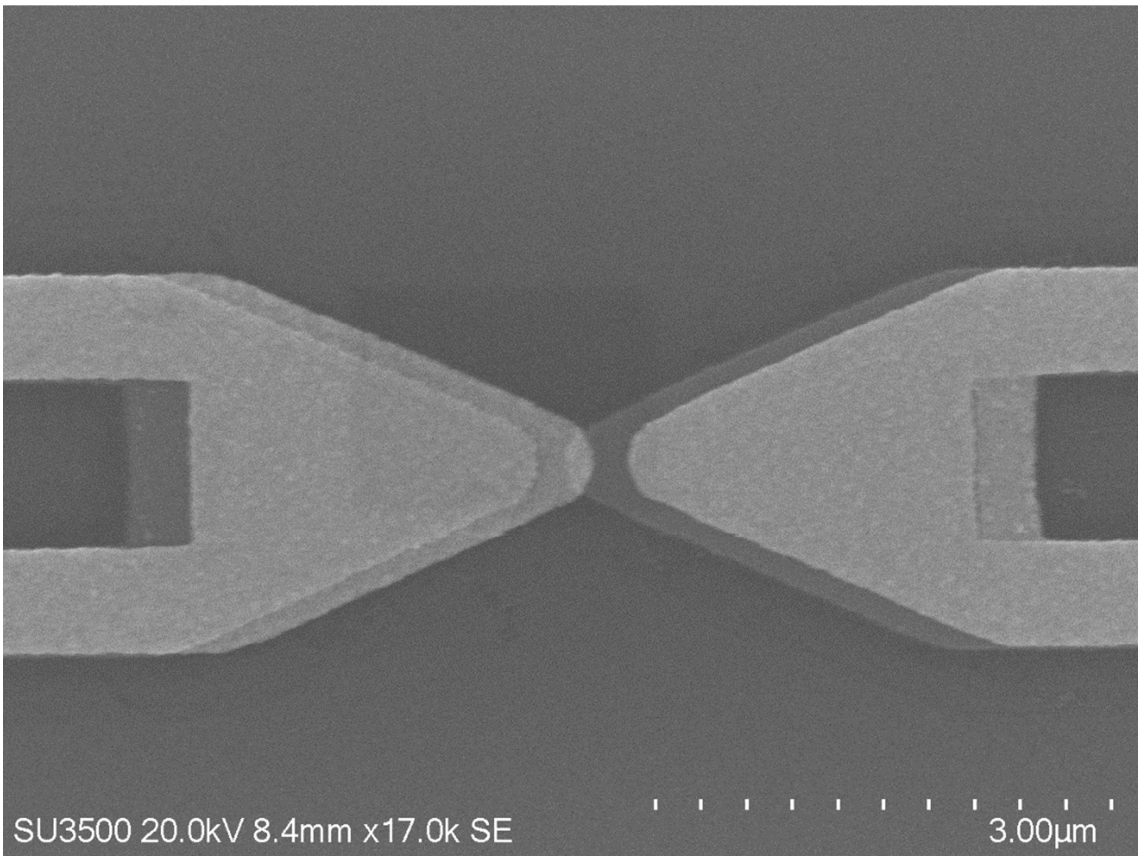

Figure 4.2: SEM of lumped-element rectenna.

The overlap MIM junction at the center measures 150 nm in the x-direction and 400 nm in the y-direction. The area is estimated at 0.7 the product of the overlap dimensions since the

overlap region is not rectangular.

Figure 4.3 summarizes the DC $I(V)$ characteristics. The plot has the raw $I(V)$ data plotted with the exponential fit. Additionally, I plot the differential resistance and responsivity versus the diode voltage. Finally, I also plot the asymmetry as calculated by the fit and the asymmetry interpolated from the raw data. Complete details of the DC $I(V)$ fitting procedure are documented in Chapter 3.

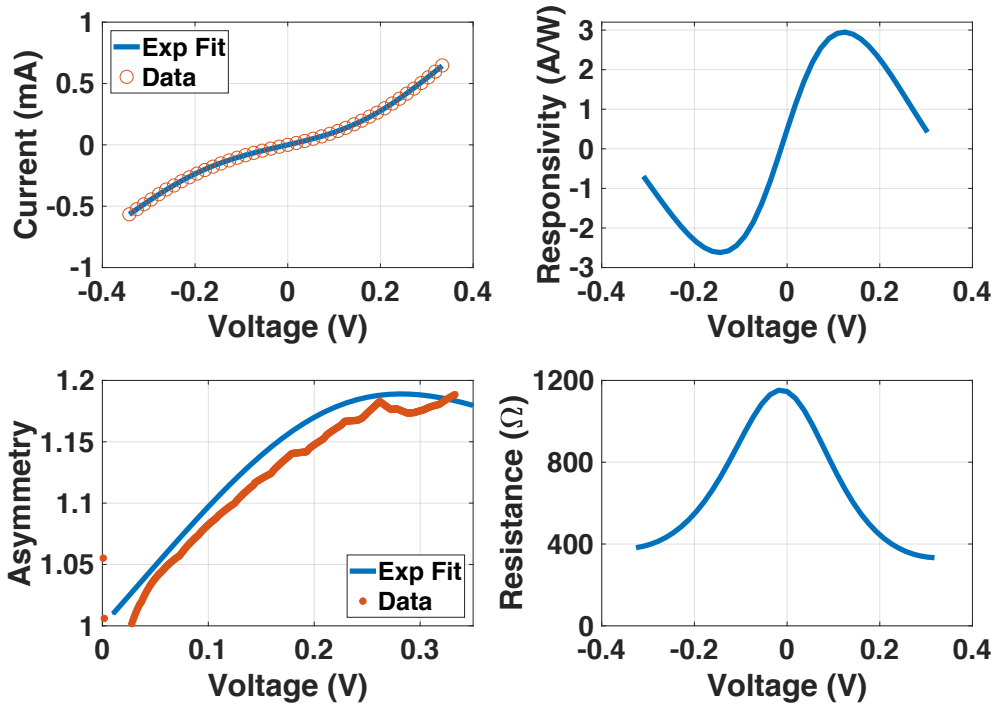

Figure 4.3: Lumped-element $I(V)$, responsivity, asymmetry, and differential resistance characteristics: $R_0 = 1151\ \Omega$ and $\beta_0 = 0.49$ A/W. The fit coefficients are as follows: $b = 10.27\ \mathrm{V}^{-1}$, $d = 9.15\ \mathrm{V}^{-1}$, $I_0 = 48\ \mu$A, $\alpha = 417\ \Omega/\mathrm{V}^2$, and $R_s = 77\ \Omega$.

The summary of the resulting fitting parameters, DC characteristics, and diode dimensions are available in Table 4.1 at the end of this chapter.

4.3 TWD1

Unfortunately, TWD1 was destroyed in the measurement process prior to taking an SEM. The device picture in Figure 4.4 is a neighboring 2 μm long device that should have representative overlap and appearance.

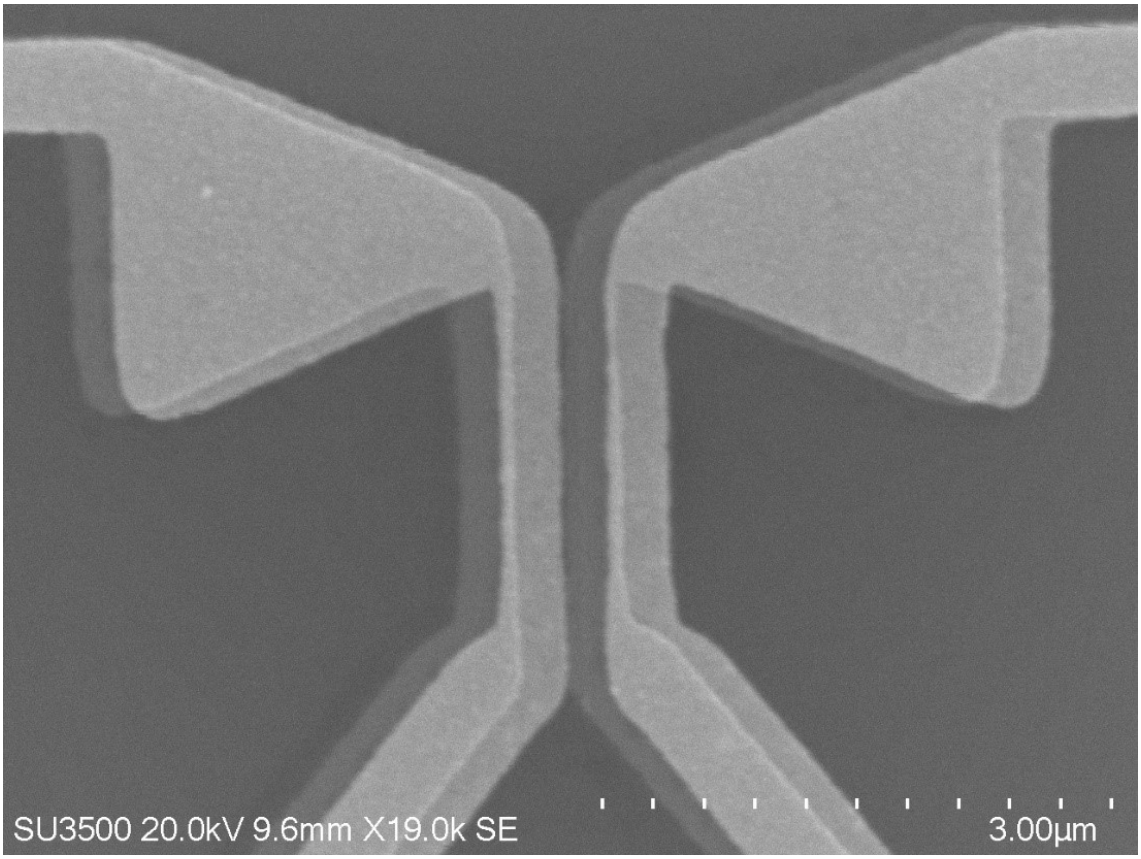

Figure 4.4: SEM of 2 μm long TWD rectenna similar to TWD1 (3 μm) used for the optical measurement.

Clearly, from the SEM, the overlap of this TWD is much smaller than the overlap in the lumped-element MIM. The overlap is very small and difficult to measure even in the SEM. Barely visible in Figure 4.4 is a slightly brighter region at the center of the TWD, this is the junction overlap. The asymmetric and non-linear $I(V)$ measurement in Figure 4.5 is the strongest proof of an MIM junction. I estimate the overlap to be $\sim$30 nm. Such a narrow nominal overlap means

that small variations in the size of the overlap will add uncertainty to the analysis of the device performance. In contrast to the lumped-element rectenna, the four-point probes are in slightly different locations; two leads are connected to the antenna, one at either end, and two connect at the end of the TWD. As I did for the lumped-element retenna, Figure 4.5 shows the $I(V)$ data for TWD1 analyzed with the exponential fit.

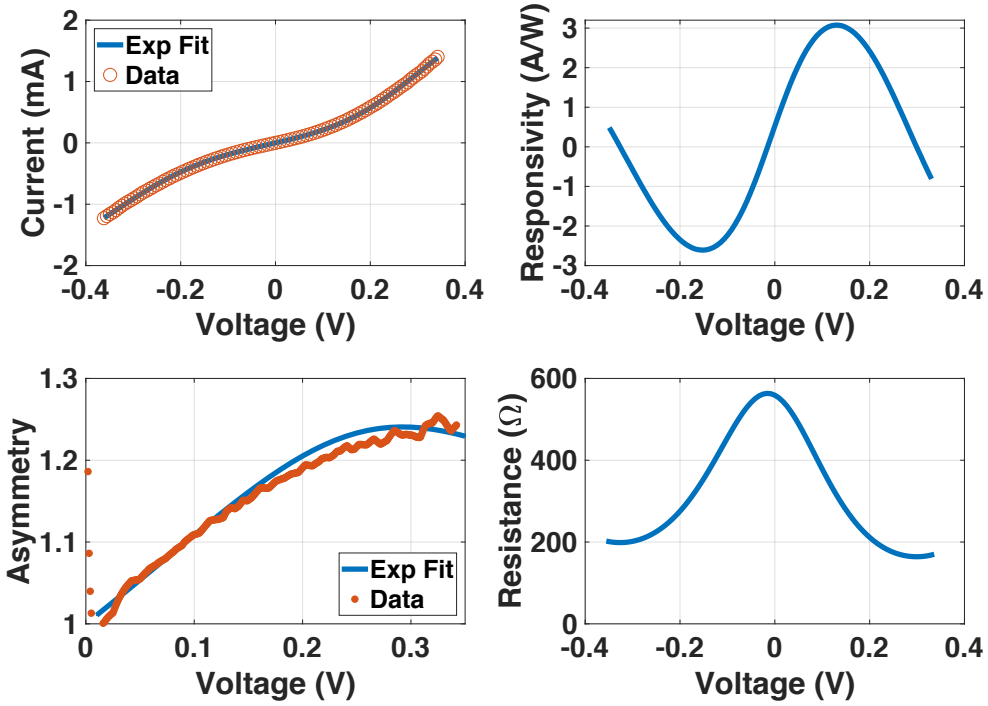

Figure 4.5: TWD1 (3 μm) $I(V)$, responsivity, asymmetry, and differential resistance characteristics: $R_0 = 559\ \Omega$ and $\beta_0 = 0.53$ A/W. The fit coefficients are as follows: $b = 9.23\ V^{-1}$, $d = 8.15\ V^{-1}$, $I_0 = 104\ \mu$A, $\alpha = 313\ \Omega/V^2$, and $R_s = 7.3\ \Omega$.

4.4 TWD2

In Chapter 5 I show that shorter TWDs have a potentially higher optical response due to resonance. Both TWD2 and TWD3 were neighboring devices on the same wafer and die, and therefore had identical processing. Additionally, both were defined in the reticle to have a length

of 1.3 μm, however, upon measurement, one appears to be slightly shorter than 1.3 μm and one slightly longer. Figure 4.6 shows an SEM of TWD2. Unfortunately, there is some minor antenna damage to this device. The four-point contacts were modified compared to TWD1. In this case, all four connect at the end of the TWD in an attempt to leave the antenna undisturbed. Unlike the TWD1 in Figure 4.4, the overlap is clearly visible in this image. The illustrated cross-section from Figure 2.3 is inset for reference; each of the seven regions from the illustrated cross-section are clearly visible in the SEM.

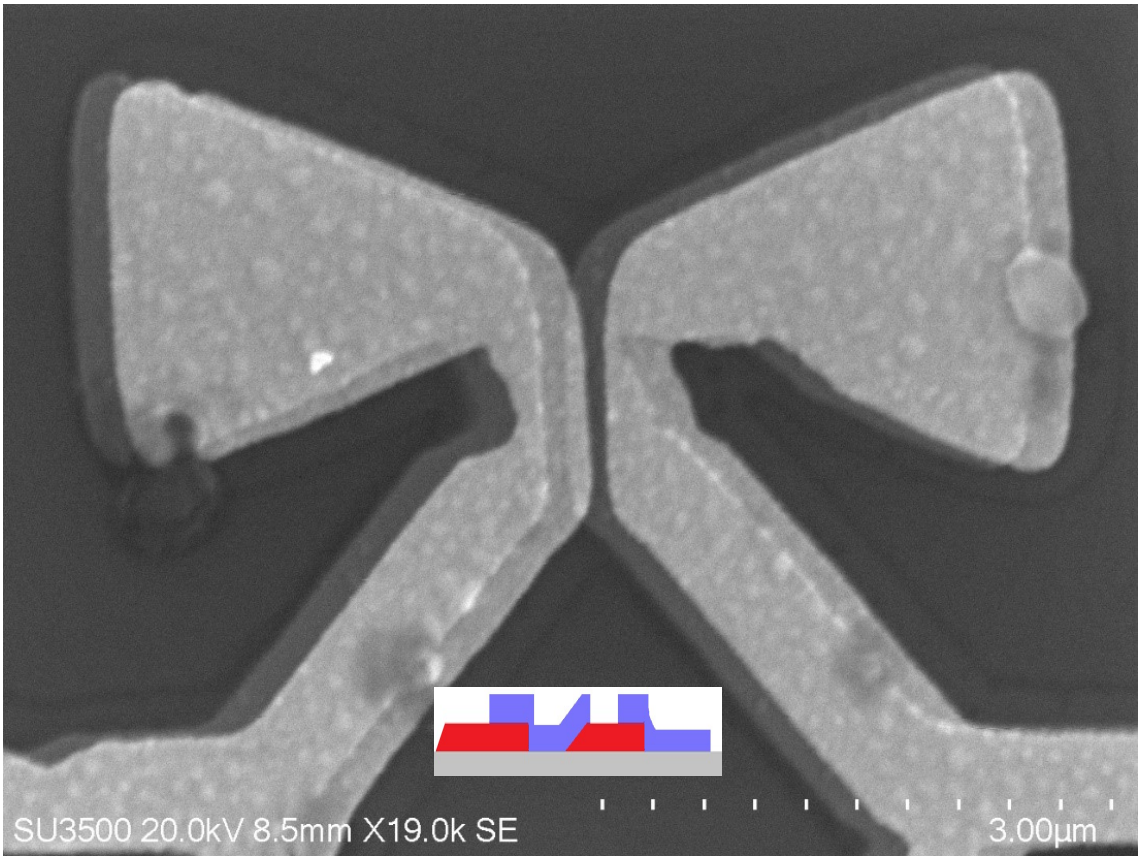

Figure 4.6: SEM of TWD2 (1.35 μm).

In addition to the antenna damage, there is some non-uniformity in the TWD region as well. Luckily, those distortions do not disturb the TWD MIM junction. I estimate this overlap to be 115 nm and the length to be 1350 nm. As I did for the previous diodes, Figure 4.7 summarizes the DC

$I(V)$ characteristics for TWD2.

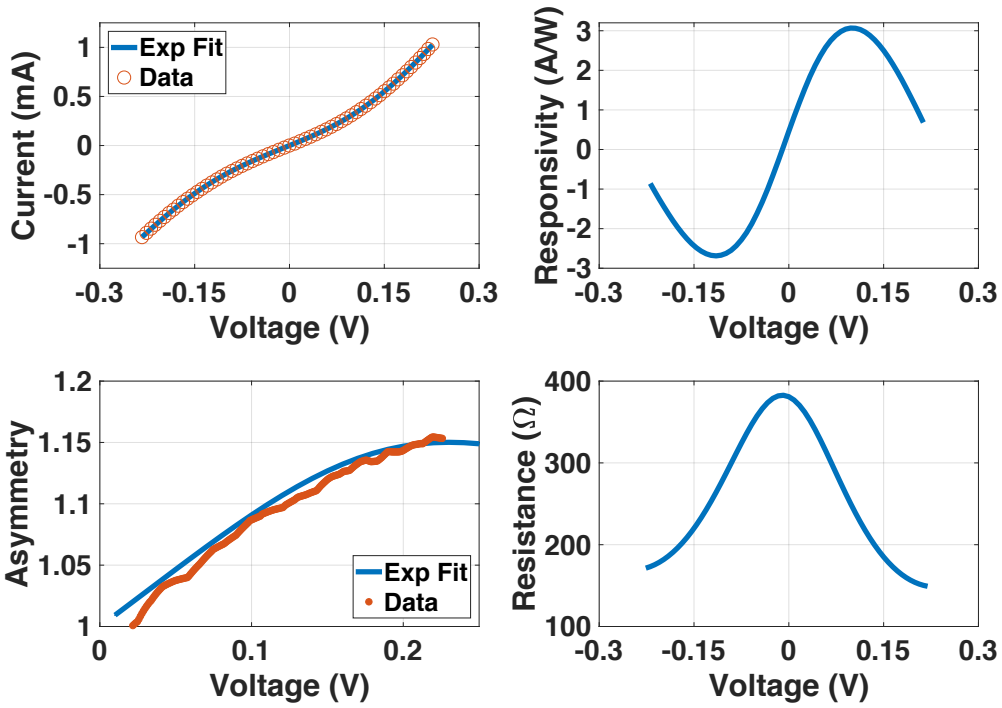

Figure 4.7: TWD2 (1.35 μm) $I(V)$, responsivity, asymmetry, and differential resistance characteristics: $R_0 = 381$ and $\beta_0 = 0.46$ A/W. The fit coefficients are as follows: $b = 11.0$ V^{-1}, $d = 10.0$ V^{-1}, $I_0 = 131$ μA, $\alpha = 386$ Ω/V^2, and $R_s = 16.5$ Ω.

4.5 TWD3

In Figure 4.8, I show the SEM of the another similar rectenna from the same die as TWD2, TWD3. Unfortunately, this rectenna also has antenna damage, specifically on the upper edge of the right bow-tie leaf and lower edge of the left leaf. The TWD region on the other hand, has the expected structure.

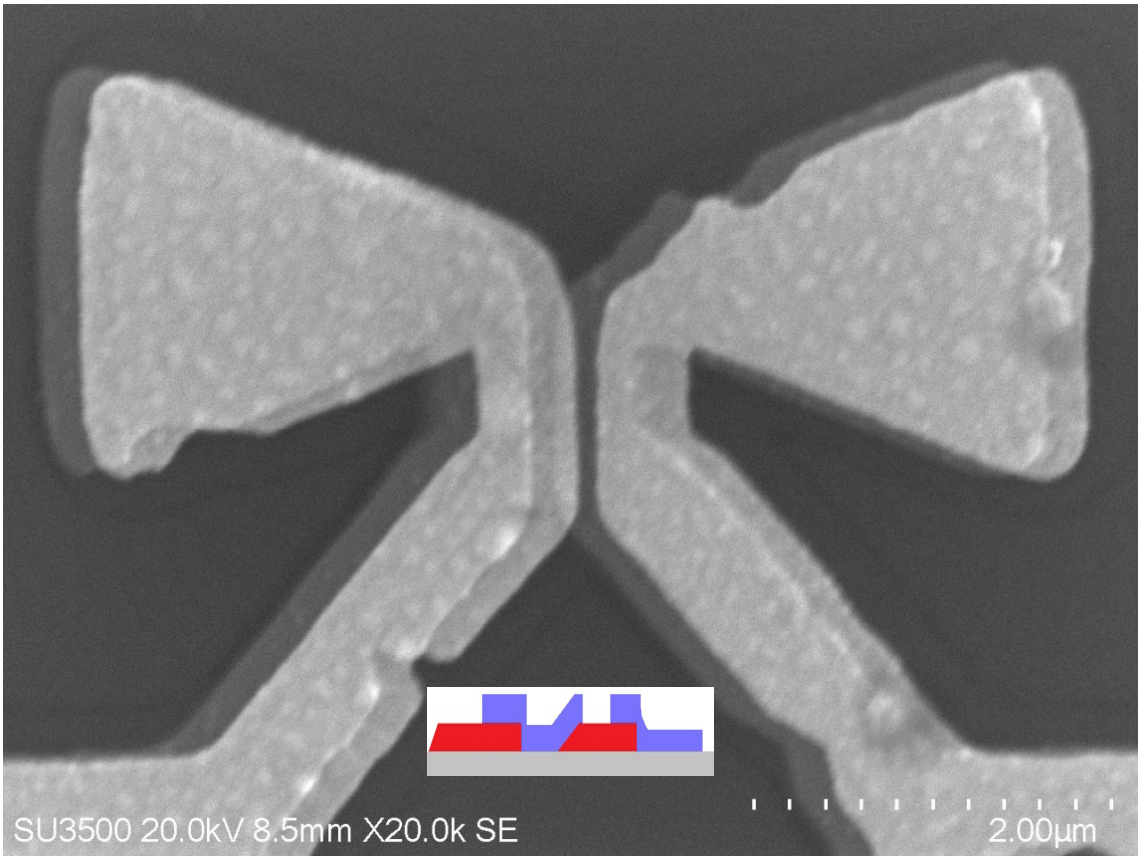

Figure 4.8: SEM of TWD3 (1.25 μm).

For TWD3, estimated diode overlap is 110 nm and the length is 1250 nm. Again, the junction characteristics are measured with an current-voltage sweep and fit with the exponential fit.

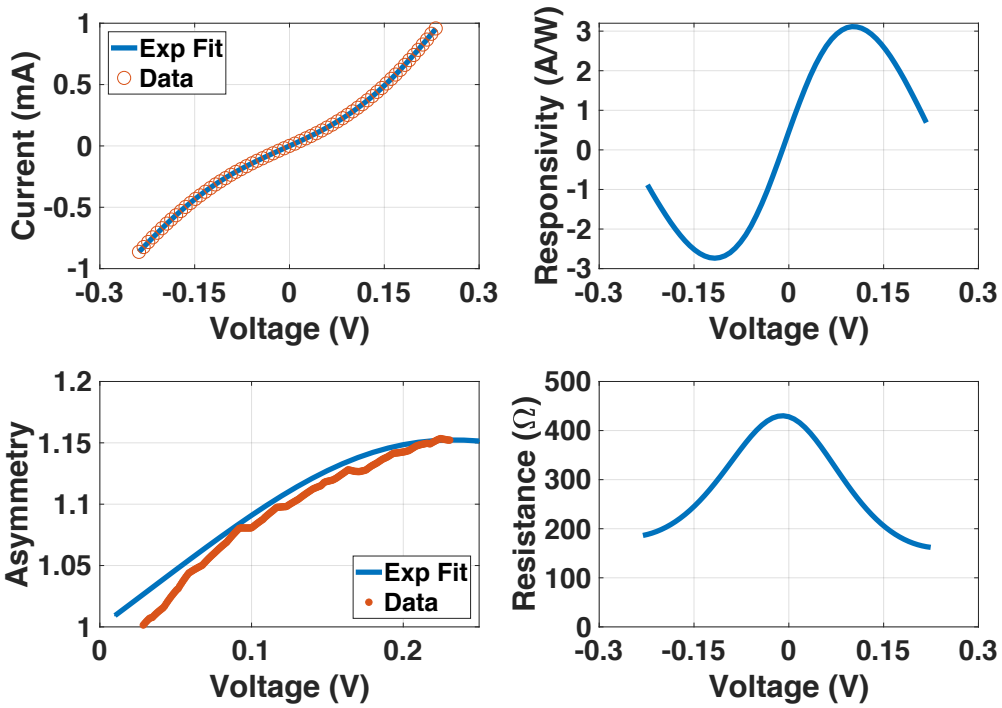

Figure 4.9: TWD3 (1.25 μm) $I(V)$, responsivity, asymmetry, and differential resistance characteristics: $R_0 = 430$ and $\beta_0 = 0.46$ A/W. The fit coefficients are as follows: $b = 10.97$ V^{-1}, $d = 9.97$ V^{-1}, $I_0 = 116$ μA, $\alpha = 406$ Ω/V^2, and $R_s = 18.1$ Ω.

4.6 TWD4

The final TWD I present is the 1.0 μm long TWD4. As the experimental results in Chapter 6 show, this device has the highest detectivity of the four TWDs presented. The germanium bridge on this wafer was wider than for the previous devices shown in this chapter. The wider bridge required that both M1 and M2 be evaporated at an angle (39.3°) from opposite directions to ensure an overlap. As Figure 4.10 shows, this results in a wider spread in the TWD region. In this case, rather than continuous metal across the TWD region, there are gaps where the substrate is visible between M1 and M2. In this device I also experimented with the lead location; in this case all four leads extend from the end of the bow-tie antenna. This change in the lead structure likely led to the wider bridge, as the reduced exposure area at the end of the TWD led to smaller

openings in the germanium. This also caused the rounding at the ends of the TWD lines, and a shorter than defined length. In the reticle, the TWD length is 1.5 μm, in the SEM, the maximum length is $\sim$1.3 μm, and the overlap region is estimated to be $\sim$1.0 μm long.

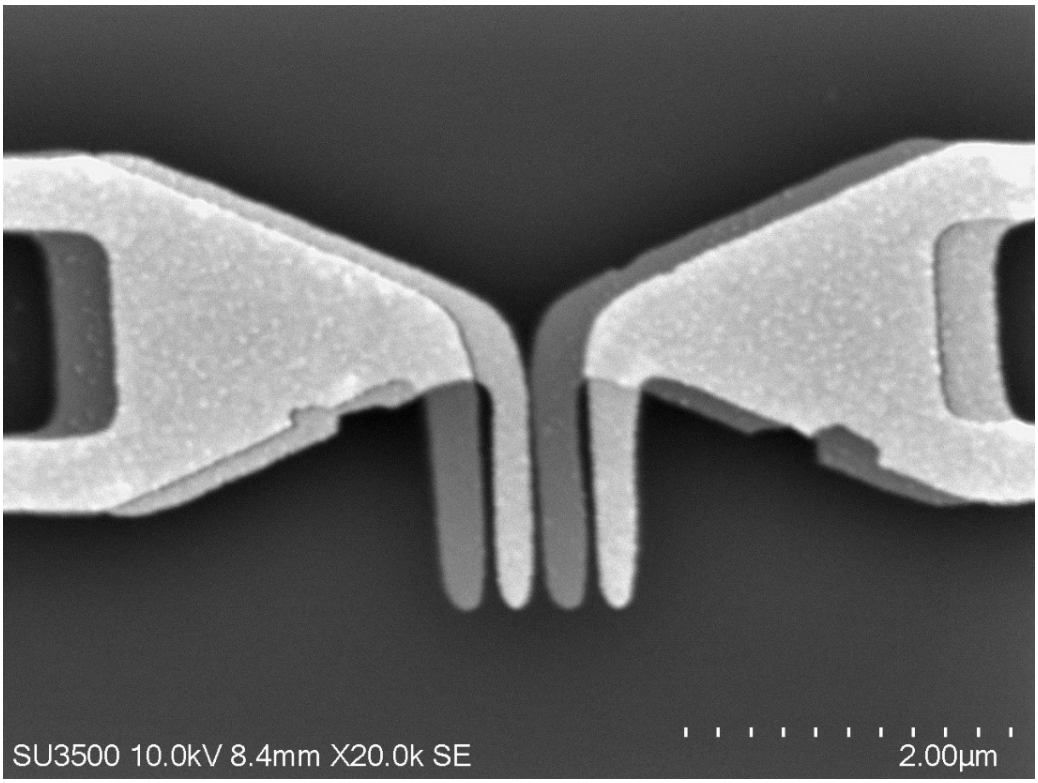

Figure 4.10: SEM of TWD4 (1.0 μm).

Similar to TWD1, it is not clear that there is an overlap in TWD4. In this particular image, there actually is not an overlap. Unfortunately, this SEM image was taken approximately one year after the device was fabricated and measured (DC and infrared illumination). At that time of the SEM, the device DC measurement showed that the MIM was no longer conductive (GΩ), probably due to some shock during measurement. Given the positive $I(V)$ measurement results shown in Figure 4.11, I know there was a conductive MIM junction at the time of fabrication and optical measurement. Given the geometries of the shadow mask, I roughly estimate the overlap was $\sim$30

nm.

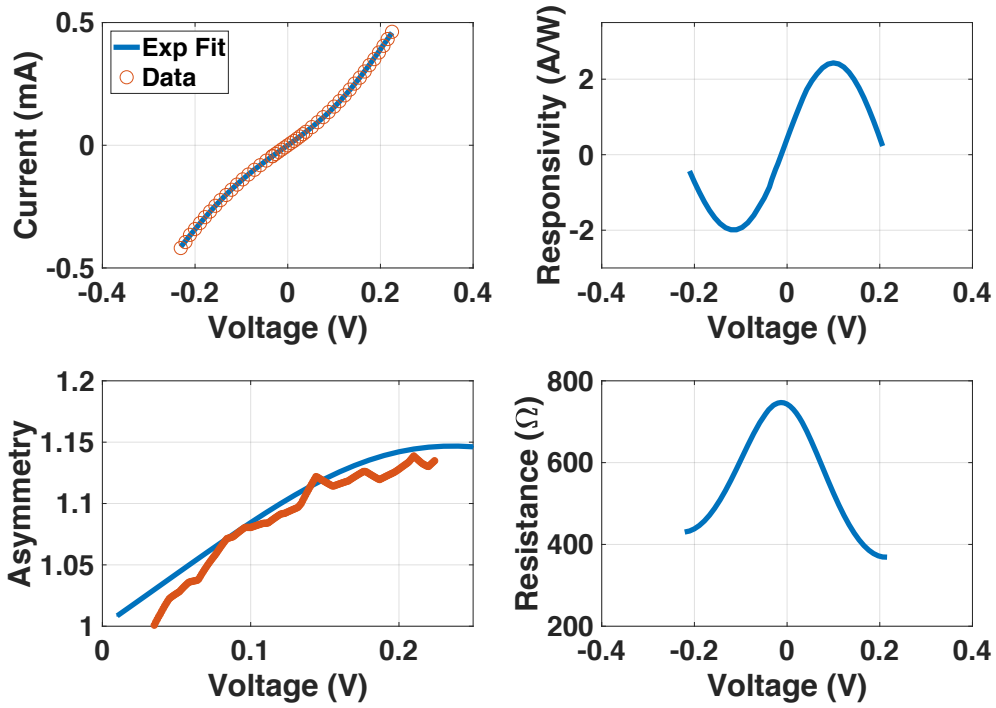

Figure 4.11: TWD4 (1.0 μm) $I(V)$, responsivity, asymmetry and differential resistance characteristics: $R_0 = 743\ \Omega$ and $\beta_0 = 0.42$ A/W. The fit coefficients are as follows: $b = 9.18\ \mathrm{V}^{-1}$, $d = 8.33\ \mathrm{V}^{-1}$, $I_0 = 77\ \mu$A, $\alpha = 1153\ \Omega/\mathrm{V}^2$, and $R_s = 0\ \Omega$.

4.7 DC Measurement Summary

All dimensions and $I(V)$ characteristics for all five devices are summarized below in Table 4.1. These values are used later to make estimates of expected rectenna performance for comparison to actual measured optical response.

Table 4.1: Summary of DC $I(V)$ measurements.

		Devices				
		LE[a]	TWD1 (3 μm)	TWD2 (1.35 μm)	TWD3 (1.25 μm)	TWD4 (1.0 μm)
Exponential Fitting Parameters	b (V^{-1})	10.27	9.23	11.0	10.97	9.18
	d (V^{-1})	9.15	8.15	10.0	9.97	8.33
	I_0 (μA)	48	104	131	116	77
	α (Ω/V^2)	417	313	386	406	1153
	R_s (Ω)	77	7.3	16.5	18.1	0
DC characteristics	R_0 (Ω)	1151	559	381	429	743
	β_0 (A/W)	0.49	0.53	0.46	0.46	0.42
Dimensions	Length (nm)	400[b]	3000	1350	1250	1000
	Overlap (nm)	150[b]	30	115	110	30
	Area (nm^2)	42,000	90,000	155,250	137,500	30,000

[a] Lumped-element

[b] Area is $\sim$0.7$\times$length$\times$overlap for the lumped-element diode because of the rounding of the corners.

Overall, the GSM technique meets the requirements for TWD MIM rectenna fabrication. It allows for small feature size (<100 nm) and clean MIM interfaces. The results are repeatable, and have a quick turn around. Figure 4.12 shows the distribution of diodes from the die on which both TWD2 & TWD3 were built. I plot cumulative distribution plots for both zero-bias responsivity vs zero-bias resistance. Since the wafer had varying device lengths, all the diode resistances were normalized to the shortest length, 1 μm. The relatively vertical nature indicates the small diode variations across the wafer and illustrates the GSM's ability to fabricate uniform MIM diodes.

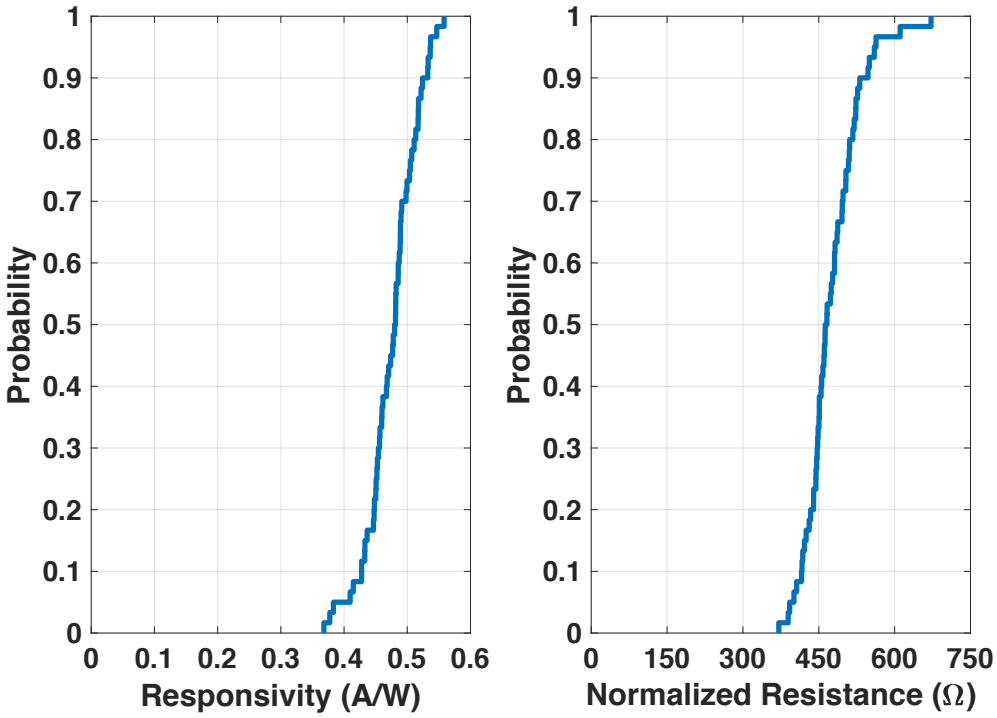

Figure 4.12: Cumulative distribution plots summary of $I(V)$ measurements.

Chapter 5

Simulation

5.1 Traveling-Wave Structure

Simulating the TWD provides insights into aspects of the device operation that cannot be easily demonstrated experimentally. I model the TWD with a slightly simplified geometry for ease of meshing the model and making controlled geometry variations. Figure 5.1 shows an implementation of TWD rectenna with a bow tie antenna, which is similar to the experimentally fabricated devices in Chapter 4. The device is fabricated on a silicon substrate coated with a 300 nm thick layer of silicon dioxide. The space above the device is air. Coherent, plane-wave, 10.6 μm radiation illuminates the device from the top xz-boundary, port 1, on the air side of the antenna. The vertical boundaries (xy and zy) are periodic (effectively a two-dimensional array) on a 10 μm by 14 μm pitch in the x and z directions respectively. This maintains the plane-wave nature of the illumination and provides a slight boost to antenna performance over non-periodic boundary conditions. The illumination is polarized along the x-direction, in line with the antenna axis, for maximum absorption. The antenna length, L_{ant}, is 5.2 μm, and the antenna flare angle, θ_{ant}, is 42.5°. We consider the transition at the feed point to be part of the antenna for the discussion of impedance matching between the antenna and TWD. This transition uses 250 nm wide metal traces that make 90° turns about a rotation point 250 nm from the edge of the trace. We use a gold bow-tie antenna and hold the geometry constant.

To understand the effects of the TWD dimensions, we varied the TWD length, L_{twd}, from 300 nm to 2 μm. We also explored the effect of the metal thickness, t_m (60 nm, 120 nm, and

240 nm), which is effectively the transmission line width because the diode is formed on the edge. Finally, we explored a small range of insulator thickness, t (2.5 nm and 5 nm). While changes in t have some effect on the TWD transmission line characteristics, the diode $I(V)$ characteristics are extremely sensitive to changes in the insulator thickness. Because of this sensitivity, t is chosen primarily to achieve the desired $I(V)$ characteristics, namely low resistance and high asymmetry. Generally, for practical, low-resistance, MIM didoes, the diode total insulator thickness must be between 2-6 nm. The metal trace width of the TWD, w_m, is held at a constant value of 250 nm.

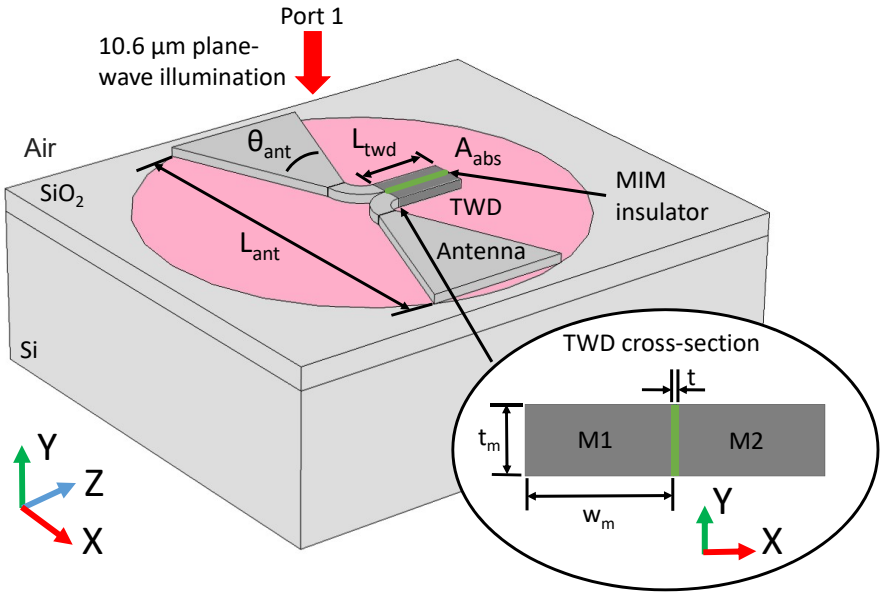

Figure 5.1: Illustration of TWD rectenna geometry and illumination conditions. The TWD is the dark gray part of the rectenna structure; the antenna is the light gray part. From each leaf of the antenna, a curved trace extends. These two curved regions are the transition region, which is considered to be part of the antenna.

For these simulations, we use a double-insulator MIM diode to take advantage of enhanced asymmetry and responsivity compared to a single insulator (Grover and Moddel, 2012; Maraghechi

et al., 2011). The diode $I(V)$ curve is based on an experimentally measured Ni-NiO(3 nm)-Nb_2O_5(2 nm)-Cr diode similar to the experimentally measured TWDs from Chapter 4. The $I(V)$ data is fit with the exponential fit in Chapter 3 and (Pelz et al., 2017), described by the following two (simplified) equations:

$$I(V) = I_0(e^{bV_D(\alpha,R_s,V)} - e^{dV_D(\alpha,R_s,V)}) \tag{5.1}$$

$$V_D(\alpha, R_s, V) = V - I(V)(R_s + \alpha V^2) \tag{5.2}$$

where V_D is the voltage on the exponential characteristic of the diode and V is the voltage on the series combination of the exponential part of the diode and its series resistance. I is the diode current, and the remaining variables (I_0, b, d, α, and R_s) are the fit coefficients. The fit parameters for the $I(V)$ curve used for this work are as follows:

$$\begin{aligned} b &= 9.30\ V^{-1} \\ d &= 8.31\ V^{-1} \\ I_0 &= 1.51 \times 10^{-4}\ A \\ \alpha &= 320\ \frac{\Omega}{V^2} \\ R_s &= 0\ \Omega \end{aligned} \tag{5.3}$$

To estimate the input power, P_{in}, we approximate the antenna absorption area, A_{abs}, to be the circle that circumscribes the antenna. Therefore, P_{in} is simply the product of A_{abs} (24 μm^2) and illumination intensity, I (10^5 W/m^2, based on our measurement system). Because the illumination is coming from the low-index side of the antenna, the antenna directivity is poor in the direction of illumination, and the maximum absorption is limited to ~13%. While the free-space-to-antenna coupling is relatively poor, it is sufficiently absorptive to provide the plasmonic excitation to explore the effects of TWD dimensions on rectenna performance. Therefore, even though antenna

optimization is important for efficient overall rectenna operation, it remains outside the scope of this work.

In the electromagnetic (EM) model, the two insulators are combined into an single insulator with the total combined thickness, t, and an average effective relative permittivity. We use $\epsilon_r = 8.5$ for NiO and $\epsilon_r = 20$ for Nb_2O_5. The low terahertz dielectric constant values measured by Thacker et al., while slightly higher, should be the upper limit for the values at 10.6 μm (Thacker and Pinhero, 2016). When exploring variations in the insulator thickness, a constant thickness ratio of 2:3 for Nb_20_5 to NiO is maintained, giving an effective relative permittivity, $\epsilon_d = 11$, calculated from series equivalent capacitance. Using effective permittivity is a valid approximation as the field confinement in the insulator is normal to the insulator interfaces, as we show in section 5.3. In practice, a thin ($\sim$3 nm) Cr layer is sufficient to achieve the desired $I(V)$ characteristics. A metal, such as Au, with better plasmonic properties can be added over the thin Cr to improve TWD rectenna performance. Two dimensional modeling of the TWD cross-section shows that the inclusion of the 3 nm layer of Cr has a small effect on plasmonic propagation characteristics compared to Au only. Specifically, without the Cr layer, the decay length is 1.36 μm, with a 3 nm layer of Cr, it is reduced to 1.31 μm, a reduction of less than 5%. In the model with no Au, the decay lenght is only 570 nm. Therefore, in this simulation, we ignore the thin Cr layer and make one lead of the TWD Au (ϵ_r = -2842 -1339*j)(Palik, 1998) for enhanced plasmon propagation. The other TWD trace is Ni (ϵ_r = -1416 -545*j) (Palik, 1998).

5.2 Solving For a Nonlinear $I(V)$ Element Within a Finite Element Solver

Linear FEM solvers are unable to incorporate the nonlinear $I(V)$ characteristics of a diode. Therefore, TWD tunneling and rectification cannot be included in the EM simulation and must be incorporated during post processing. Without the inclusion of the diode $I(V)$ characteristics, the MIM insulator is modeled as perfectly insulating in the EM simulation. Therefore, the decay of the surface plasmon is solely the result of plasmonic resistive decay, i.e., resistive heating of the TWD. In reality, electron tunneling through the insulator also consumes power from the plasmonic wave and

increases the rate of decay. This means that by ignoring the tunneling in the EM simulation, we are making an approximation that underestimates the total plasmonic decay. For this approximation to be valid, the total power taken from the plasmonic wave due to tunneling, P_{tunnel}, must be much smaller (<5%) than the plasmonic power, P_{spp}, the power that enters the TWD at the boundary between the TWD and antenna. In the case this condition is not met, the resulting fields from the EM simulation require modification during the post processing to reflect the additional decay due to tunneling.

Figure 5.2 illustrates the power flow through the rectenna system and where we make the distinction between the EM modeling and the post-processing rectification calculation. First, in the EM portion of the simulation, a free-space wave is incident on the antenna. A portion of the incident power, P_{in}, is either transmitted or reflected, while the rest is absorbed, P_{abs}. Of the absorbed power, some is lost to resistive heating in the antenna; the rest is transmitted to the TWD, P_{spp}, based on the impedance match with the antenna. Of the power that is transmitted to the diode, some is lost to plasmonic resistive decay. The remainder drives both forward and reverse tunneling current. This power flow, P_{tunnel}, is represented by a dashed arrow in Figure 5.2 because it is excluded in the EM model due to the exclusion of tunneling. The net DC output, P_{dc}, is calculated from the net current due to the asymmetric electron tunneling in the MIM junction, also know as short-circuit current, I_{sc}. The difference between P_{tunnel} and the output power is the power lost to reverse leakage. In this paper, we will direct our analysis to finding the detectivity, D^*, which is a detector metric calculated using I_{sc}, shown in detail in section 5.5.

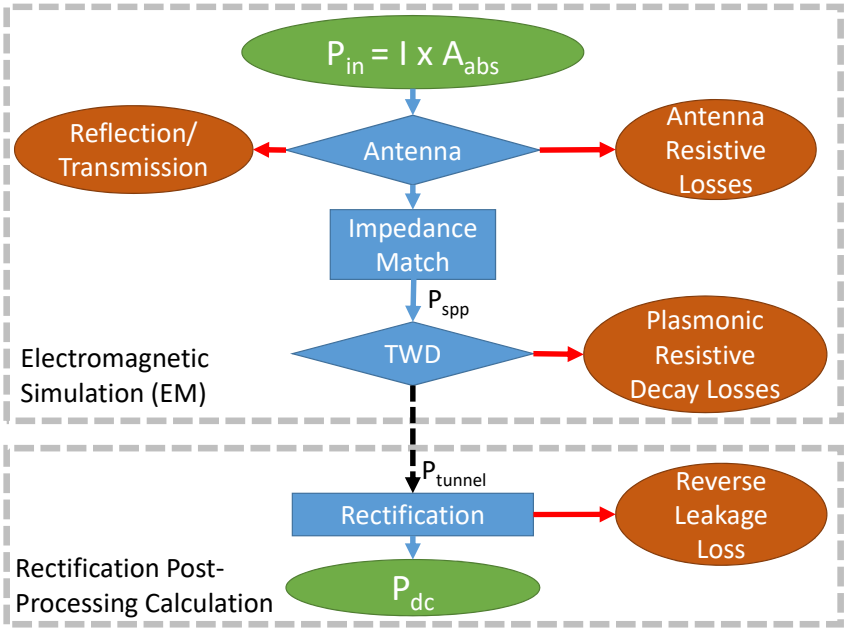

Figure 5.2: Power flow in TWD operation and the separation of the EM simulation and post processing calculations. The total input power, P_{in}, is calculated from the product of radiation intensity and absorption area. Loss mechanisms include: radiation not absorbed due to reflection or transmission past the antenna, resistive heating of the antenna and TWD, and electron tunneling in the reverse direction.

5.3 TWD Surface Plasmon Theory

A metal-insulator interface supports a confined electromagnetic mode, known as a surface plasmon polariton (SPP) (Woolf et al., 2009). When two metal-insulator interfaces share a thin insulator, the SPPs on the two interfaces couple into either a symmetric mode or an antisymmetric mode. This coupling usually occurs when the separation between the two metal-insulator interfaces is less than 100 nm. Figure 5.3 shows the dispersion relationship for a Au-insulator-Au MIM structure calculated using the Drude model. We use the same effective insulator as in our TWD, ϵ_d = 11 with a thickness of 5 nm. While a Ni-insulator-Au structure has slightly different dispersion characteristics due to the asymmetry in the structure, the concepts remain the same and the

Au-Insulator-Au configuration is a good approximation. The dashed curve represents the single interface plasmon dispersion relationship. The single surface plasmon mode is confined to the area below the light line and below the surface plasmon frequency, f_{spp}:

$$f_{spp} = \frac{\omega_p}{2\pi\sqrt{1+\epsilon_d}} \tag{5.4}$$

where ω_p is the plasma frequency of the metal. When two single surface modes couple, the symmetric and antisymmetric modes split from the single surface dispersion curve. The smaller the metal separation, the further the coupled modes move from the single surface. For a metal-to-metal separation much smaller than the wavelength, the symmetric mode exists above the surface plasmon frequency. The Coulomb repulsion prohibits SPP of the same charge to travel in phase without high energy, thus the symmetric mode dispersion is found at high frequency. This quasi-static treatment of the transverse field is generally valid for TEM transmission lines, assuming negligible variation in the transverse fields. Therefore, one can say the "natural" mode of operation at low frequencies is the antisymmetric mode, which is equivalent to differential transmission line modes, hence the traveling wave behavior of the surface plasmon. Given the smaller effective wavelength (larger k_z) for the plasmon relative to free-space, a transmission line that supports an antisymmetric SPP mode in the THz region is equivalent to what is known as a "slow-wave" transmission line in RF.

The symmetric and antisymmetric modes are depicted next to their respective dispersion curves. From the figure, it is clear that at 10.6 μm (~28 Thz), only the antisymmetric mode is accessible. In this mode, there is a very large field confinement in the direction perpendicular to the insulator, E_x, as shown in the Figure 5.3 lower insert. This is crucial to the operation of a TWD, as it is this field that drives the electron tunneling through the asymmetric junction. The symmetric mode has an electric field null down the center of the insulator and cannot drive tunneling. Since the antisymmetric mode never intersects the light-line, it cannot be excited directly from a free-space wave, but rather require some sort of structure to achieve a momentum match (Nicol, 2005). In our case, the antenna fulfills this function (Muehlschlegel et al., 2005; Knight et al., 2011; Novotny and

Van Hulst, 2011). The inclusion of the transition region, shown in Figure 5.1, adds sharp curvature that allows charge concentration with alternating charges at smaller than the free-space wavelength periodicity, i.e. the larger k_z necessary for a momentum match.

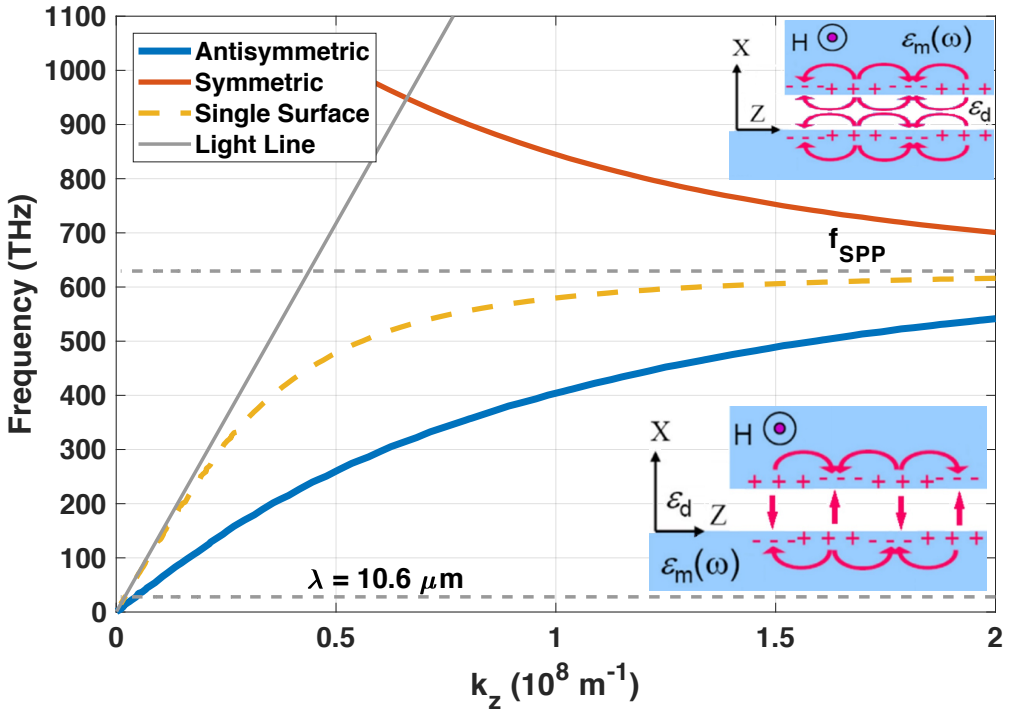

Figure 5.3: Au-Insulator-Au dispersion characteristics for an MIM structure with a 5 nm insulator. The antisymmetric and symmetric mode field characteristics are illustrated next to their respective dispersion curves.

5.4 EM Simulation Results

We examine the field distribution at the center of the insulator and along the length of the TWD structure for an illuminated antenna to see what mode has been excited. Figure 5.4 shows the field strength in the insulator along the TWD length. The alternating polarity of E_x confirms the excitation of the antisymmetric mode described in section 5.3. At the beginning of the TWD, $z = 0$, E_x starts in phase with H_y showing that power is propagating in the positive z-direction.

Only at the end of the TWD, we see a shift in the relative phases of E_x and H_y due to reflections at the open transmission line termination. The reflection off the end of the TWD also explains why the field exceeds the expected decay envelope, represented by the dashed black line in Figure 5.4. We can see that the plasmonic wavelength, λ_{spp}, is ~928 nm and the decay length, ℓ, is ~1.34 μm. A larger ℓ is desirable as it indicates less resistive plasmonic decay loss.

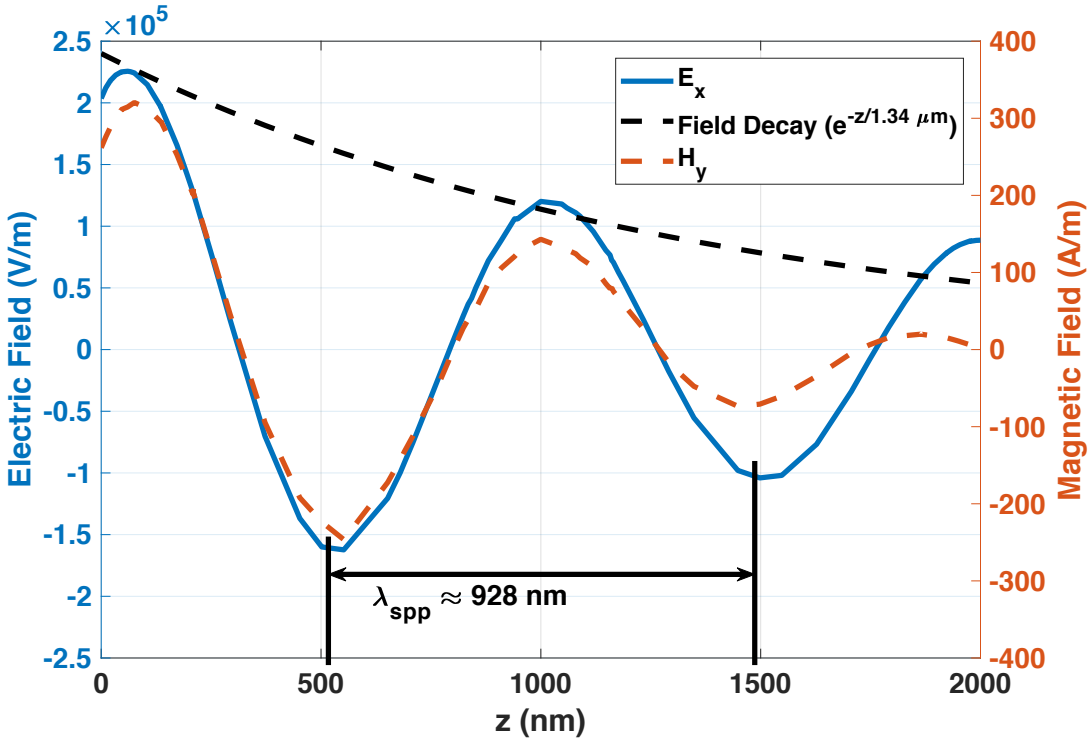

Figure 5.4: Electric and magnetic fields (E_x and H_y) at the center of the MIM insulator along the length of the TWD (z-dimension) with insulator thickness (t) of 5 nm, metal thickness (t_m) of 120 nm, and TWD length (L_{twd}) of 2.0 μm, for $I = 1 \times 10^5$ W/m^2 illumination condition.

Table 5.1 summarizes the plasmoinc wavelength, λ_{spp}, and decay length, ℓ, for the four TWD cross-sections considered. This table shows us that as t_m is reduced both ℓ and λ_{spp} increase. As t is reduced, both ℓ and λ_{spp} decrease too.

Table 5.1: Simulated TWD plasmonic wavelength and decay length

Insulator Thickness (t)	Metal Thickness (t_m)		
	60 nm	120 nm	240 nm
t = 2.5 nm	Not Simulated	ℓ = 760 nm λ_{spp} = 631 nm	Not Simulated
t = 5.0 nm	ℓ = 1.42 μm λ_{spp} = 1.06	ℓ = 1.34 μm λ_{spp} = 928 nm	ℓ = 1.26 μm λ_{spp} = 850 nm

We can calculate the total power absorbed in the rectenna, P_{abs}, as the sum of the antenna resistive loss, the plasmonic resistive decay loss, the reverse leakage loss, and the rectified output. In addition to the xz upper boundary port where the plane wave is excited, there is a second xz boundary port, port 2, on the bottom of the silicon substrate. This port calculates the through power, that is the power that is transmitted past the device and through the substrate. The air, SiO_2 and Si are all modeled as lossless at 10.6 μm; therefore, the power absorbed in the rectenna can be approximated as the total power absorbed in the system. The total power absorbed in the system is the difference between the input power to the system and the sum of the power that exits the upper and lower ports.

$$P_{abs} = IA_{p1}(1 - |S_{11}|^2 - |S_{21}|^2) \tag{5.5}$$

where I is the input intensity and A_{p1} is the area of port 1. S_{11} and S_{21} are the S-parameters for ports 1 and 2 respectively.

Length has an important effect on the total absorbed power, as Figure 5.5 shows. We see that the length of the TWD can establish a resonant behavior. These resonant peaks occur at $\sim \lambda_{spp}/2$ intervals. The size of the resonant peaks decreases for longer TWDs. Additionally, the height of the resonant peaks decreases faster for increased length when the cross-sectional geometry has a shorter decay length, as is the case for the 2.5 nm insulator. From an impedance perspective, narrow transmission lines, which corresponds to smaller t_m, result in a better coupling efficiency to the

antenna. This is due to the capacitive nature of the antenna impedance. Perfectly matched source and load impedances are complex conjugates of each other. With a narrower TWD, the input impedance becomes more inductive, and therefore a better match to the antenna. We observe a similar effect with insulator thickness, as t increases, the TWD capacitance is reduced, and the match is improved. As the TWD becomes substantially longer than the decay length, the variations in impedance with length decrease as the antenna no longer sees the open circuit termination of the line.

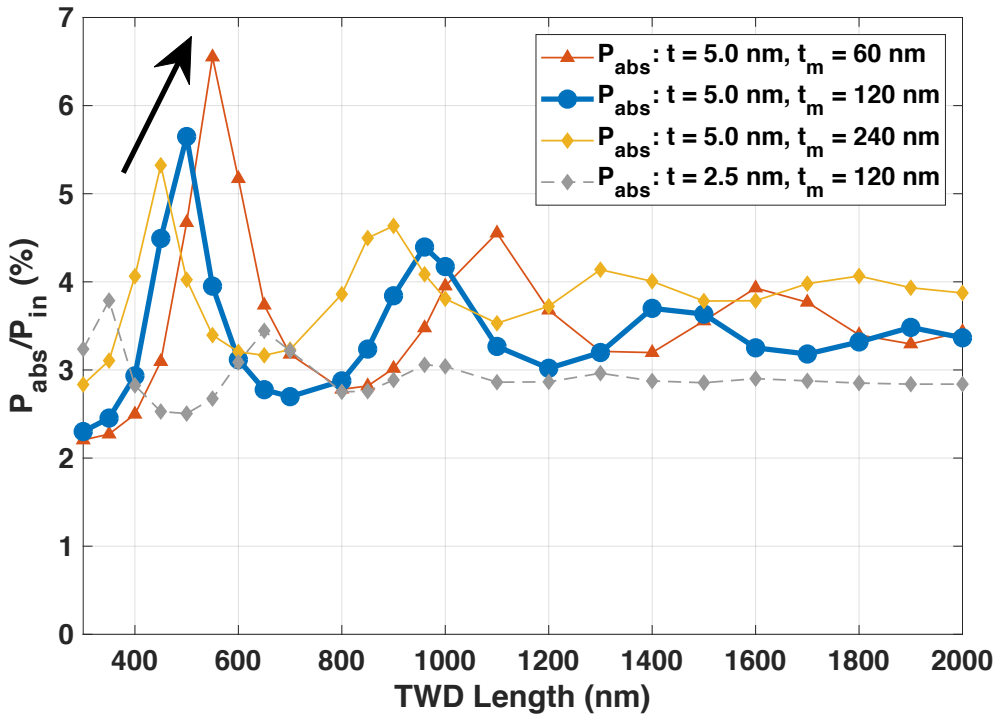

Figure 5.5: Fraction of the incident illumination power that is absorbed in the TWD rectenna vs TWD length for different cross-sectional geometries (insulator and metal thicknesses).

To confirm that the resonance behavior we see in Figure 5.5 is due to impedance match, we model the antenna and the diode separately. We excite each structure at the interface where they meet, illustrated by the TWD cross-section in Figure 5.1, using a lumped-port voltage excitation. The voltage is applied from the Ni (M1) to the Au (M2) across the TWD insulator. This allows us

to estimate the impedance of the two individual elements so we can calculate the coupling efficiency. Of the three TWD dimensions we vary, the two cross-section dimensions affect the antenna: t_m and t. While we keep the antenna geometry mostly constant, we make the small changes necessary to prevent sharp steps at the transition boundary between the antenna and TWD. The antenna impedance for the four sets of TWD cross-section dimensions are summarized in table 5.2:

Table 5.2: Simulated antenna impedance

Insulator Thickness (t)	Metal Thickness (t_m)		
	60 nm	120 nm	240 nm
t = 2.5 nm	Not Simulated	61-95j Ω	Not Simulated
t = 5.0 nm	117-112j Ω	80-104j Ω	45-82j Ω

From the decoupled TWD simulation, the real part of TWD input impedance for our geometries varies from 6 to 95 Ω and the imaginary part varies from -8 to 63 Ω. This variation comes largely from the TWD length dependence. In Figure 5.6 below, I show the real and imaginary components of the input impedance versus TWD length for both a 120 nm overlap TWD and a 60 nm overlap TWD. As expected, the input impedance approaches a constant value (the characteristic impedance) when the TWD length becomes much longer than the plasmonic decay length. At short lengths I see a similar resonant behavior as Figure 5.5.

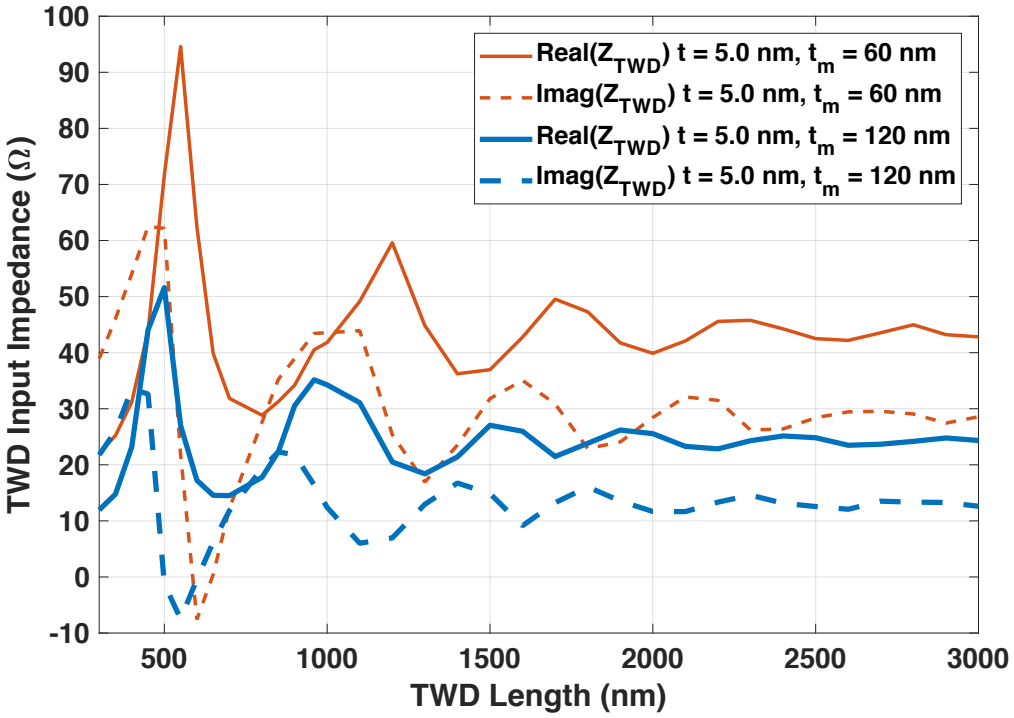

Figure 5.6: Input impedance for TWDs with t=5.0 nm and t_m=120 nm and 60 nm versus TWD length, L_{twd}.

Figure 5.7 shows the dependence of TWD characteristic impedance on TWD width, t_m. As the TWD width decreases, both the real and imaginary parts of the TWD characteristic impedance increase, i.e. the characteristic impedance become more inductive (less capacitive). Given the capacitive nature of the antenna, and the need for a conjugate match, this narrower width results in better coupling.

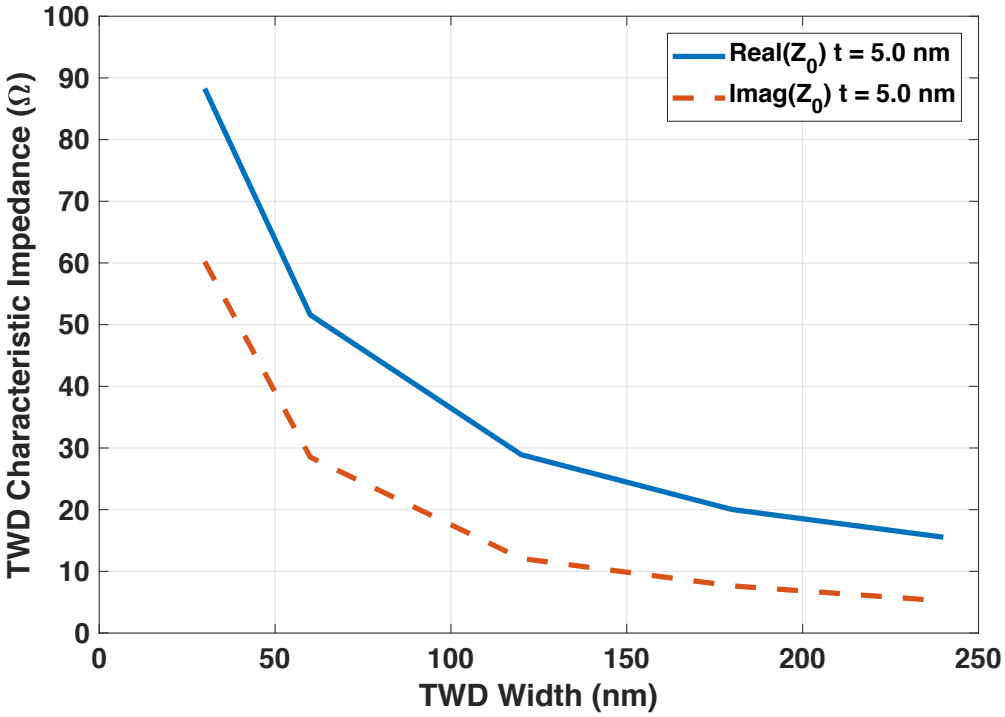

Figure 5.7: TWD characteristic impedance, Z_0, for TWDs with t=5.0 nm and t_m from 30 to 240 nm versus TWD width, t_m. The characteristic impedance is equal to the input impedance for TWD lengths much longer than the plasmonic decay length.

These values are consistent with the input impedances shown by Figure 5.6 when the TWD length becomes much longer than the decay length. Using the antenna and TWD impedances, the coupling efficiency is calculated using the following equation:

$$\eta_c = \frac{4R_{twd}R_{ant}}{(R_{twd}+R_{ant})^2+(X_{twd}+X_{ant})^2} \tag{5.6}$$

where R_{ant} and X_{ant} represent the real and imaginary parts of the antenna impedance, respectively. R_{twd} and X_{twd} are the real and imaginary parts of the TWD input impedance, respectively, not to be confused with the diode DC resistance calcuated by Eq. 5.14 and used in Eq. 5.13 and Eq. 5.15. The resulting coupling efficiency from Eq. 5.6 is plotted in Figure 5.8 versus TWD length for the cross-section variations of interest.

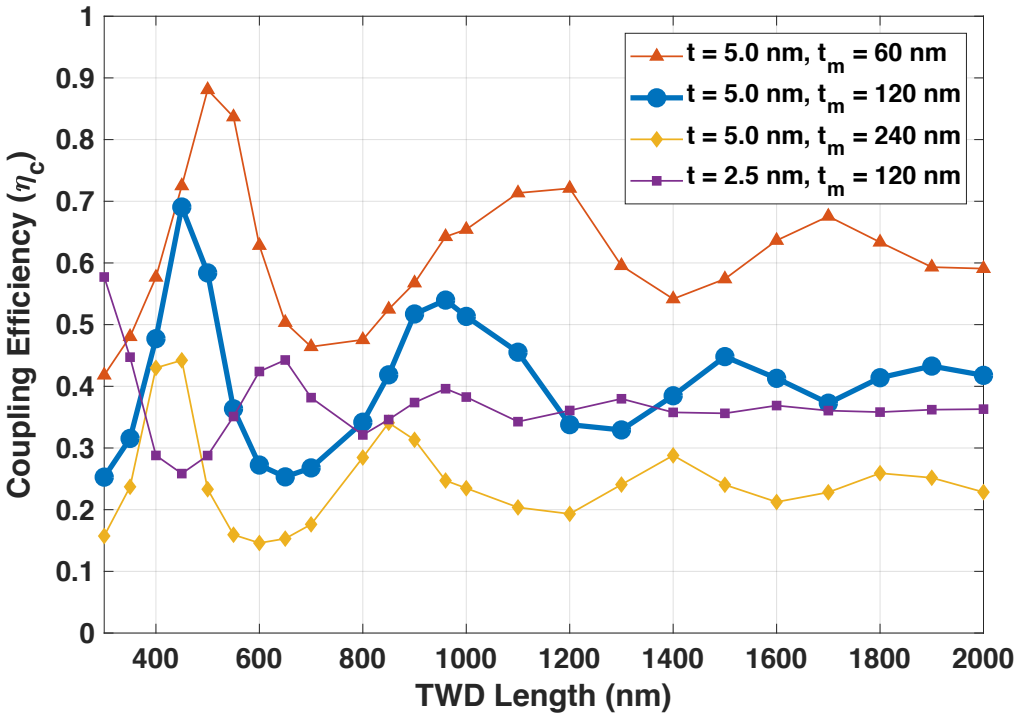

Figure 5.8: Decoupled calculated impedance match efficiency for different TWD geometries versus length of the TWD.

While the impedance coupling efficiency results are informative, and show what sort of effect we should expect from TWD geometry variations, they are more qualitative than quantitative due to the method of excitation. Comparing Figure 5.5 and Figure 5.8, the geometry effects are much more pronounced in the decoupled impedance match calculation (Figure 5.8). Figs. 5.9 (a) and (b) show the surface currents at the cross-sectional boundary between the antenna and TWD, illustrated in Figure 5.1, from the decoupled antenna and TWD simulations respectively. These modes look very similar as both were excited by applying a potential difference at the inner edges of the diode metals. In both cases, the modes are contained tightly around the diode insulator gap, where the excitation occurred. Figure 5.9 (c) shows the coupled antenna/TWD simulation, and the surface currents on the antenna/TWD interface are much more distributed. This is because in the coupled model, the entire rectenna is excited by a 10.6 μm plane-wave. In this case, all the surfaces of the metal in the transition region, not just the surfaces at the MIM junction, are used to carry

current as the antenna concentrates the plasmonic energy to the feed point and MIM insulator. Because of the more concentrated current in the decoupled simulations, Figure 5.8, compared to Figure 5.5, exaggerates the effect of changes in geometry on the calculated impedance match.

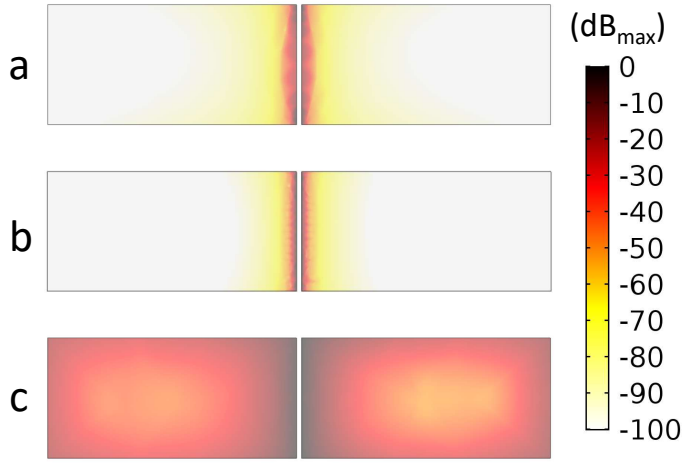

Figure 5.9: Normalized current density in dB for cross-section at TWD/antenna interface (a) Antenna only simulation (b) TWD only simulation (c) Coupled simulation.

5.5 Post Processing and Rectification Performance

The MIM asymmetric tunneling characteristics are added in post processing using the $I(V)$ equation generated by Eq. 5.1 to calculate the tunneling currents. We use a TWD rectenna without an external DC bias, as it has an experimental advantage of avoiding possible bolometric effects in a measurement. Since we have a TWD, the MIM junction does not have the same voltage everywhere. Therefore, we must use the DC $I(V)$ characteristics of the diode and the modeled electric field to calculate the current through the insulator. Given the relative uncertainty of the insulator thickness from the measured MIM diode, we want the tunneling estimate in the post-processing calcuation to be dependent on the area of the simulated TWD but independent of the insulator thickness chosen in the EM simulation. Therefore, we define a voltage dependent conductance per unit area, G_a(V),

rather than a conductivity. To convert $I(V)$ to G_a(V), we use the following:

$$G_a(V) = \frac{I(V)}{V L_{twd} t_m} \tag{5.7}$$

where L_{twd} is 3 μm and t_m is 115 nm for the experimental device on which the $I(V)$ characteristic is based. Before proceeding to analyze the rectification performance of the TWD rectenna with metrics like detectiviy and short-circuit current, we need to check that our assumptions are valid; specifically, that P_{tunnel} is much less than P_{spp} (<5%). The plasmonic power, P_{spp}, is the power that enters the TWD in the form of a surface plasmon at the boundary between the diode and the antenna. The amount of power transfered is determined by the impedance match. It is calculated using the Poynting vector integrated over the cross-sectional area of the diode insulator in the plane normal to the propagation direction.

$$P_{spp} = \frac{1}{2} \int_0^t \int_0^{t_m} Re(\overline{E}_x \times \overline{H}_y^*) \cdot \hat{z} dx dy \tag{5.8}$$

Given the current distribution in Figure 5.9 (c), this calculation tends to understate P_{spp} as it only includes the power on the MIM interface. To calculate P_{tunnel}, we take the average over a full 2π cycle of incident radiation of the tunneling power density (voltage times current density) integrated over the yz cut-plane at the center of the MIM insulator.

$$P_{tunnel} = \int_0^{2\pi} \int_0^{L_{twd}} \int_0^{t_m} \frac{G_a(E_x t) E_x^2 t^2}{2\pi} dy dz d\phi \tag{5.9}$$

where E_x is the electrical field in the x-direction, normal to the MIM interface, and is a function of position (y and z), and phase of the illumination wave, ϕ. From evaluating Eq. 5.8 and Eq. 5.9, at a maximum, P_{tunnel} is 3.9% of the P$_{spp}$. Therefore, the additional plasmonic decay due to tunneling can be ignored. Now that we have confirmed the validity of our initial assumptions, we can calculate the final performance metrics such as short-circuit current and detectivity. The first metric to calculate is short-circuit current with an equation very similar to Eq. 5.9 for P_{tunnel}. We integrate the current density over the insulator area and average over a full 2π cycle of incident

radiation.

$$I_{sc} = \int_0^{2\pi} \int_0^{L_{twd}} \int_0^{t_m} \frac{G_a(E_x t)E_x t}{2\pi} dydzd\phi \tag{5.10}$$

Using short-circuit current, system responsivity can be calculated as:

$$\beta_{sys} = \frac{I_{sc}}{P_{in}} \tag{5.11}$$

System responsivity is the ratio of DC current and optical AC input power. From system responsivity we calculate specific detectivity (Rogalski, 2003):

$$D^* = \sqrt{A_{Abs}\Delta f}\frac{\beta_{sys}}{I_n} \tag{5.12}$$

where Δf is the detector bandwidth, A_{abs} is the rectenna absorption area, and I_n is the noise current calculated in Eq. 5.13 from the Johnson noise due to the diode resistance and the shot noise due to DC bias.

$$I_n = \sqrt{\Delta f(2qI_{bias} + \frac{4kT}{R_0})} \tag{5.13}$$

In Eq. 5.13 k is the Boltzmann constant, q is the electron charge, and T is temperature, taken to be 300 K for this work. I_{bias} is the DC bias current, taken to be zero for this work as we have modeled an asymmetric MIM designed to operate at zero-bias. The zero-bias diode resistance, R_0, is calculated from Eq. 5.7 evaluated at $V = 0$.

$$R_0 = (G_a(0)L_{twd}t_m)^{-1} \tag{5.14}$$

The detectivity from Eq. 5.12 can be simplified by combining Eq. 5.12 and Eq. 5.13. The detector bandwidth terms cancel and leaves the following:

$$D^* = \beta_{sys}\sqrt{A_{Abs}}\sqrt{\frac{R_0}{4kT}} \tag{5.15}$$

Figure 5.10 shows detectivity versus length of various TWDs and a lumped-element rectenna with the equivalent MIM area and junction characteristics as the TWD with $t = 5$ nm, $t_m = 120$ nm, for any given length. For the lumped-element (LE) diode, short-circuit current was calculated with the following:

$$I_{sc/LE} = P_{in}\eta_{ant}\eta_c\beta_0 \tag{5.16}$$

where η_{ant} is the maximum antenna absorption given in section 5.1, ~13%, and β_0 is the zero-bias responsivity, 0.49 A/W, calculated from the DC $I(V)$ fit. The coupling efficiency, η_c, comes from Eq. 5.6, where the TWD impedance is replaced with the series equivalent of the diode resistance in parallel with the diode capacitance ($R_0||1/\mathrm{j}\omega C_d$), described in detal in Appendix B. The capacitance of the diode, C_d, is calculated as the planar geometric capacitance. As expected, the lumped-element and the equivalent TWD detectivities converge for extremely short TWDs. For the thin (2.5 nm) insulator TWD, the detectivity is substantially lower than the TWDs with 5 nm insulators. This is primarily because of the shorter plasmon propagation length along a thinner insulator. This validates our intuition that for a given $I(V)$ characteristic, a thicker insulator will have better overall rectenna performance. For the two variations of the 5 nm insulator shown, the detectivies exhibit the same trend established by the diode impedance match in Figure 5.8.

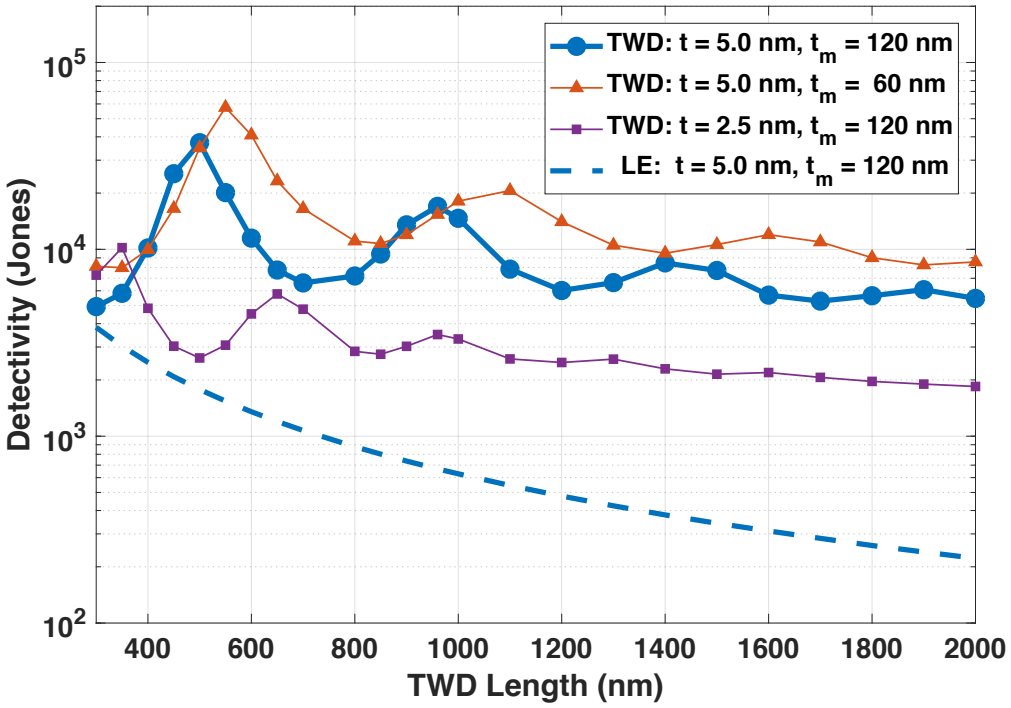

Figure 5.10: TWD detectivity vs TWD length for varying TWD cross-sections and a comparison lumped-element (LE) rectenna.

If we modify the $I(V)$ equation exponential fit parameters from Eq. 5.3, we can see the effects of improved diode $I(V)$ characteristics. For example, we can double the responsivity and leave the resistance unchanged by increasing b and reducing d by identical amounts and doubling the difference between them (Pelz et al., 2017). This leads to doubling the detectivity for any given length. Likewise, we could reduce the resistance by a factor two by doubling I_0. This increases the detectiviy by $\sqrt{2}$ for any given TWD length.

We compare the TWD detectivity reported by Grover et al. (Grover et al., 2010) for a 2D model with $t = 2.0$ nm, $t_m = 100$ nm and assuming L_{twd} greater than decay length, to the most similar device from this work ($t = 2.5$ nm, $t_m = 120$ nm, $L_{twd} = 2000$ nm). The detectivity reported in Figure 5.10 is lower by a factor of ∼1600; Grover reported 3×10^6 Jones at 10.6 μm and we observed 1.85×10^3 Jones. This difference stems from three fundamental expansions in this work. First, Grover assumes a perfectly efficient antenna while our maximum absorption is ∼13% due to

the illumination from the low index side of the antenna. Grover also assumes perfect impedance match while our coupling efficiency is calculated explicitly, simulated directly, and found to be ∼22% (out of the maximum ∼13% absorption for our antenna, 2.8% was observed in Figure 5.5). Finally, Grover uses a biased responsivity from a simulated $I(V)$ curve that we estimate to be 14 times larger than the zero-bias responsivity we use with our unbiased detector. Using Eq. 5.13 we estimate our noise current to be 5.5 pA. From Eq. 5.12 we can estimate Grover's noise current to be 3.3 pA, a factor of ∼1.7 times lower than ours. The combined effects of these assumptions result in a reduction of responsivity by a factor of ∼860 (8, 4.5, 14, and 1.7 respectively). The additional factor of ∼2 could be due to any combination of a number of factors (slight variations in cross-section, different materials). Considering Grover et al.'s idealistic assumptions Grover's predictions are are consistent with our results.

Using the design techniques in this paper, we observed a ∼31× increase in detectivity, from 1.85×10^3 to 5.75×10^4 Jones, from a device with a thicker insulator, narrower overlap, and shorter length (t = 5.0 nm, t_m = 60 nm, L_{twd} = 550 nm). This improvement derives from four improvements: First, the improved coupling efficiency accounts for a factor of ∼2.3 based on the higher absorption in Figure 5.5 (2.8% increased to 6.5%). Second, the reduced area (2000 nm × 120 nm decreased to 550 nm × 60 nm) leads to a proportionally higher resistance. From Eq. 5.15, detectivity scales as the square root of resistance for a detectivity increase by a factor of ∼2.7. Third, the thicker insulator and narrower overlap leads to a longer decay length from Table 5.1. We can estimate the improvement in detectivity due to increased decay length from Figure 5.5 and Figure 5.10. For the change in TWD cross-section, holding the length constant at 2000 nm, the detectivity increases by a factor of 4.64 (1.85×10^3 Jones to 8.56×10^3 Jones). This increase is due to the product of the improved coupling efficiency and the longer decay length. The same comparison for absorption yields a factor of ∼1.2 (2.84% to 3.4%) which is is unaffected by the increased decay length. Therefore, we estimate the improvement due to increased decay length is ∼3.9 (4.64/1.2). These first three factors combine for an overall improvement by the observed ∼24 (2.3, 2.7 and 3.9 respectively). The final improvement of ∼1.3 is the result of higher electric fields

due to reflections at the open termination of the TWD. When the device length is shortened, more power is reflected. This increased refection leads to higher fields and larger voltage swings on the $I(V)$ curve and better rectification. Thus, we demonstrate how to design a TWD with coupling characteristics near Grover's idealistic assumptions.

5.6 Simulation Conclusion

We have presented a comprehensive analysis of the interaction between the antenna and the TWD. The analysis has taken into account the nonlinear transmission line loading as a first order approximation. We showed that such an approximation is valid for low tunneling currents. We use this method to study the effects of TWD cross-section dimensions and TWD length. At lengths greater than the decay length of the surface plasmon, the effect of length is minimal. However, when the length is shortened to less than a decay length, resonant peaks that appear as a function of length become very pronounced. When the TWD input impedance is well matched to the antenna impedance, we see resonance peaks that improve the overall operation of the rectenna.

Chapter 6

Optical Measurement

Once the devices have been fabricated and DC tested to confirm quality MIM interfaces with good nonlinearity and asymmetry, I make illuminated measurements to check the high-frequency response. I analyze the open-circuit voltage response and compare the results to simulation and the estimated lumped-element rectenna response for a lumped-element diode with an equivalent area. This lumped-element estimated response is described in detail in Appendix B.

6.1 Optical Measurement Setup

To test the high-frequency response of the TWD rectenna, I illuminate it with 10.6 μm linearly polarized radiation from a CO_2 laser. Most of my measurements were made with a SYNRAD 48-1SWJ, which is pulse-width modulated (PWM). Unfortunately, this is a less than ideal source as it was designed to be a cutting tool, and the beam stability is marginal. The laser is modulated with a function generator (Agilent 33220A) at 20.0 kHz. The reference for the lock-in amplifier is generated by a mechanical chopper (SR540) around 2 kHz as shown in Figure 6.1. A few of the measurements were made with a continuous wave (CW) Access L4SL CO_2 laser, but the lower intensity of the CW laser made establishing a good signal-to-noise ratio more difficult. Therefore, I will generally focus the analysis on measurements using the PWM laser.

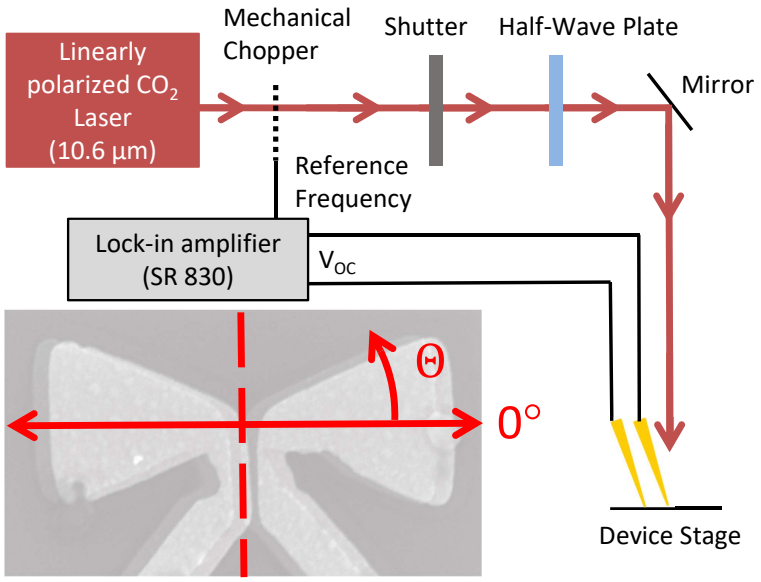

Figure 6.1: Infrared optical illumination measurement setup with linearly polarized CO_2 laser.

The infrared beam passes through a shutter (ThorLabs SH05) and and a half-wave plate (Gooch and Housego XC13) prior to illuminating the TWD. The shutter allows monitoring the baseline noise level read by the lock-in amplifier (SR830) under dark conditions. The half-wave plate rotates the polarization of the incident beam relative to the antenna axis with a motorized rotational stage (ThorLabs PRM1Z8). In the starting position of the half-wave plate, $\Theta = 0°$, the laser polarization is aligned with the antenna axis. The half-wave plate rotates the beam in the counter-clockwise direction relative to the rectenna as shown in Figure 6.1. By rotating the incident polarization, I can confirm that the rectenna has the expected $\cos^2$ response from a bow-tie antenna.

The open circuit-voltage, V_{oc}, is measured by the lock-in amplifier. I choose V_{oc} over short-circuit current so that lead resistance will not load the rectenna and reduce the measured signal. Just as with the DC measurement, there is a mercury switch to keep the two probes shorted together until the measurement is made. This prevents static discharge during the preparation steps from damaging the device. Most of the equipment (lock-in amplifier, shutter, half wave plate)

is computer controlled to standardize the measurement process. The software takes 20-30 data points for each polarization and averages the values for each polarization data point shown in the following sections.

6.2 Laser Beam Characterization

6.2.1 Beam Profile Measurement

An accurate calibration of the input illumination conditions is essential to analyzing rectenna performance. I start by assuming the beam has a Gaussian profile and that the beam intensity can be represented by the following equation:

$$I(x,y) = I_0 exp(-\frac{(x-x_0)^2 + (y-y_0)^2}{2\sigma^2}) \tag{6.1}$$

where x and y are the coordinates of the cross-sectional plane of the beam, x_0 and y_0 are the position of the beam center in that plane, and I_0 is the maximum beam intensity. The beam radius, defined as the radius with I_0/e intensity, is σ. I characterize the laser beam profile with a knife edge measurement illustrated in Figure 6.2, which assumes the beam is radially symmetric.

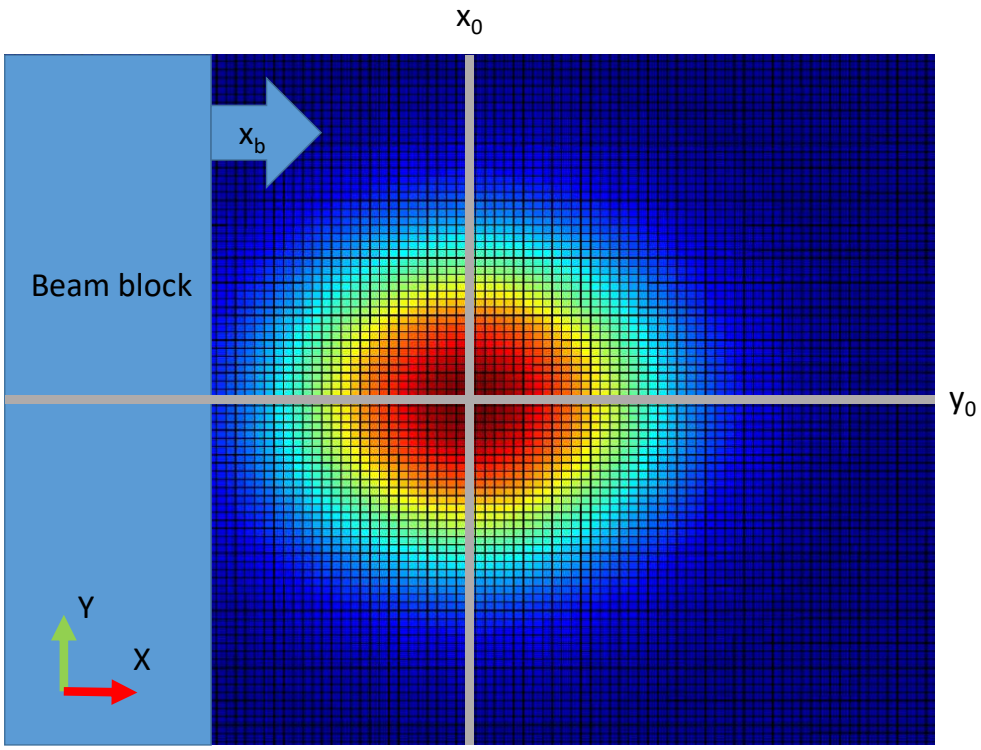

Figure 6.2: Beam profile knife-edge measurement with arbitrary Gaussian profile where red and blue are high and low intensity respectively.

For this measurement, the laser is directed into calorimeter (Scientech Astral AI310) with a large aperture (~20 mm), so that the entire beam reaches the detector. Then using a motorized linear translational stage (ThorLabs MTS25-Z8), I block a portion of the beam in 0.25 mm steps with a thin square plate (the "knife-edge") and record the corresponding power versus linear position of the beam block (x_b). After the measurement is complete, I shift the data so that the beam is centered in the coordinate plane, i.e. $y_0 = 0$ and $x_0 = 0$. In other words, when $x_b = x_0$ ($x_b = 0$), the measured power is 50% of the maximum. The resulting power should fit the Gaussian curve from Eq. 6.1 integrated from -∞ to the position of the beam block in the x-direction and from -∞ to +∞ in the y-direction. This calorimeter power versus beam block position can be described by

the following equation:

$$P_{calorimeter}(x_b) = \frac{\pi}{4} I_0 \sigma^2 (1 - erf(\frac{\sqrt{2}r}{\sigma})) = \int_{-\infty}^{\infty} \int_{-\infty}^{x_b} I(x,y) dx dy \tag{6.2}$$

In Eq. 6.2, erf() is the Gaussian error function. The measured power for the PWM laser versus the position of the beam block is shown in Figure 6.3 (a). The data fits the integrated Gaussian in Eq. 6.2, and has a coefficient of determination, R^2, 0.999.

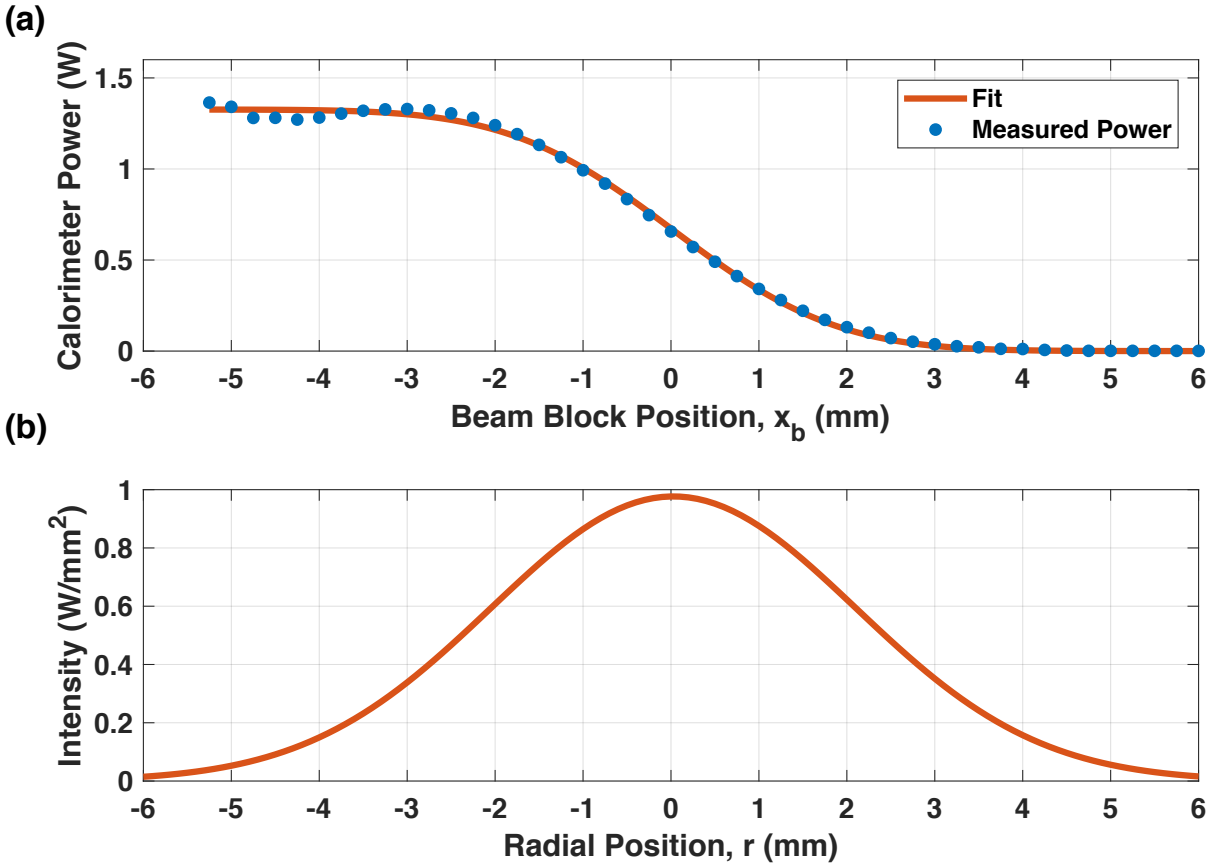

Figure 6.3: PWM beam profile measurement

Figure 6.3 (b) shows the beam intensity versus the radial position from the beam center, r, where $r = \sqrt{x^2 + y^2}$. This figure shows that pulsed laser has a maximum intensity of ~1 W/mm^2.

The beam is large enough that we can confidentially align our device at the center of the beam where it will receive the maximum intensity from the incident radiation. Inside a 1.6 mm diameter circle, the intensity is within 10% of the maximum. For the CW laser, measured with the same technique, the maximum intensity is $\sim$0.04 W/mm^2.

6.2.2 Laser Beam Stability

To check the stability of the PWM laser beam, I modified the setup in Figure 6.1. I replaced the TWD rectenna with a photodiode with an integrated current amplifier (Boston Electronics PVM-10.6, HgCdTe). Since the laser beam has such a high intensity, the photodiode was placed near the edge of the beam, rather than the center, to prevent damage. The photodiode current amplifier was connected to the input of the lock-in amplifier. Since the photodiode response is polarization independent, I added a linear polarizer after the half-wave plate. The combination of the linearly polarized laser, the half-wave plate, and the linear polarizer forces the response to have a $\cos^2$ polarization dependence. Figure 6.4 shows the photodiode response from two identical measurements that were run consecutively. I ran the measurements from 0° to 720° so that the half-wave plate will have rotated a full 360° (half-wave plates rotate polarization by twice the relative angle between incident polarization and the fast axis of the wave plate).

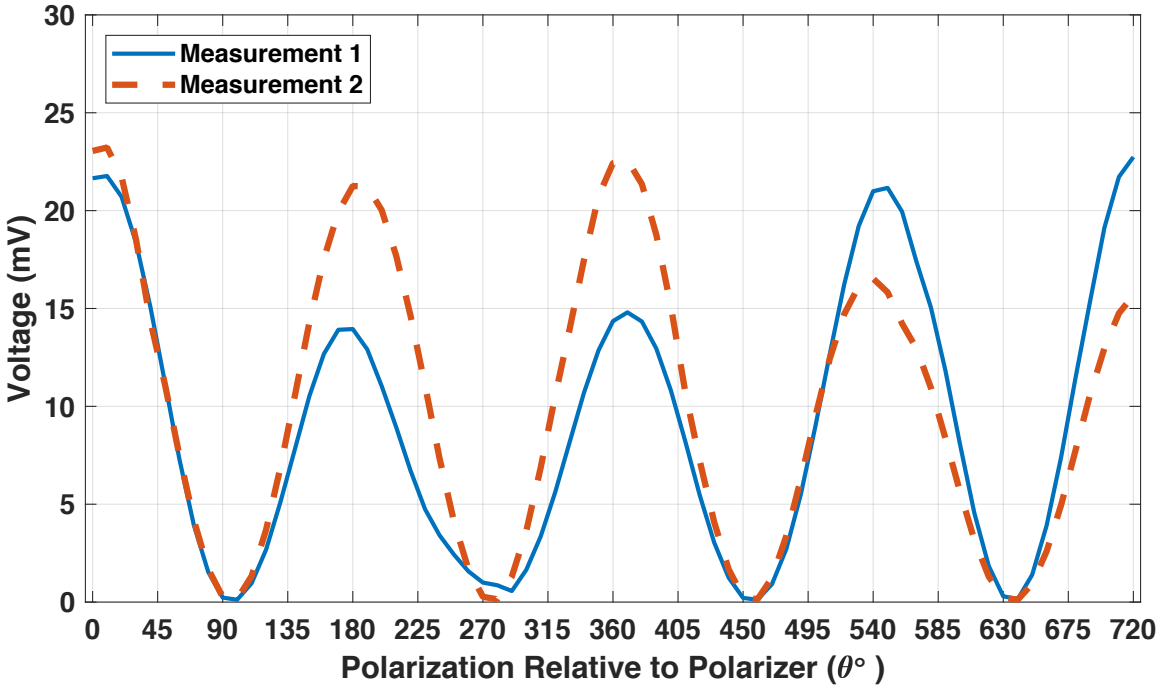

Figure 6.4: Photodiode response for two measurements with identical illumination conditions demonstrating beam wander in the PWM laser. Each measurement ran for about 25 minutes.

As expected, the peaks occur when the polarization aligns with the linear polarizer and nulls when the polarization is perpendicular to the linear polarizer. However, the change in the peak magnitude by as much as 40% was not expected. From Figure 6.3 (a), specifically from -5.25 mm to -4 mm, before the beam block has intercepted a substantial portion of the beam, the power output of the laser is relatively stable (∼10% variation). Since the measurement was taken twice, and the peak variation was different each time, this variation is not due to some defect in the half-wave plate or polarizer. This means that the variation (beyond the ∼10% power output fluctuation) is due to instability of the laser beam, specifically, beam wander. This conclusion is also supported by the fact the nulls in the photodiode response are found at consistent polarizations, but the peaks can shift several degrees from one measurement to the next.

6.3 Interpreting Lock-in Amplifier Response

As discussed at the beginning of the chapter, I want to measure the open-circuit voltage of the illuminated rectenna. The lock-in amplifier, however, measures the RMS voltage, V_{rms}, of the fundamental sine wave of the input signal at the reference (modulation) frequency. The input signal to the lock-in is a PWM square wave with a duty cycle, D, at the frequency set by the function generator, $1/T_L$, also known as the repetition rate for the PWM laser, usually 20 kHz. This signal is further modulated by the mechanical chopper with a 50% duty cycle and a period, T, which provides the reference for the lock-in. The open-circuit voltage, V_{oc}, of the rectenna has the same shape as the laser pulses through the mechanical chopper, and is represented by the dotted blue pulse train in Figure 6.5.

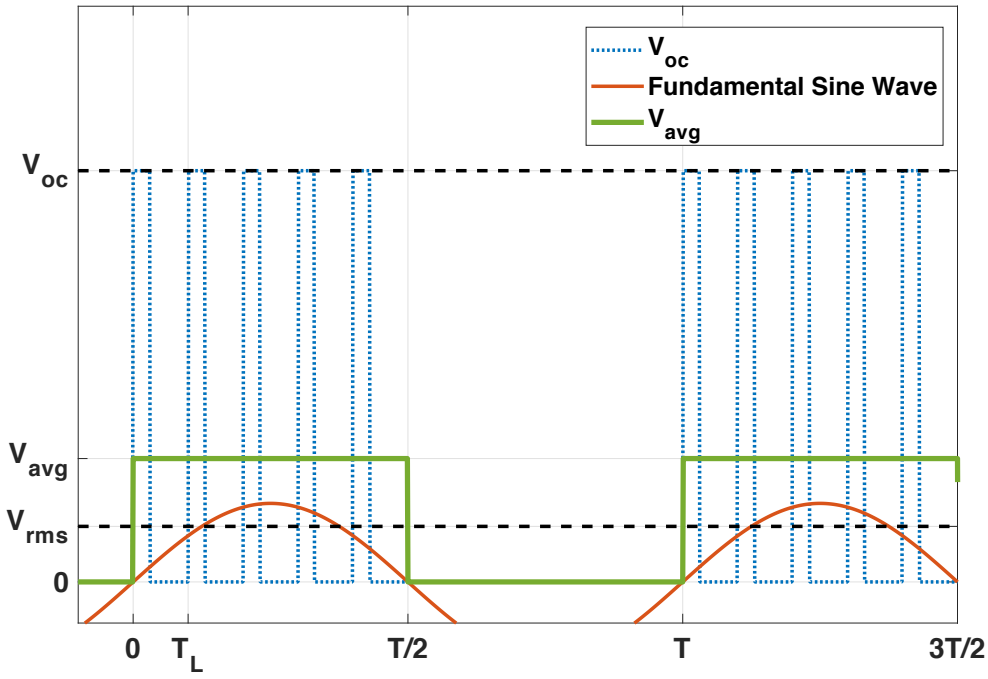

Figure 6.5: Calculating open-circuit voltage form lock-in amplifier response. The dotted blue pulse train is the rectenna V_{oc} into the lock-in amplifier. The green square wave with period T is the average of V_{oc} at the reference frequency, $1/T$. The red curve is the fundamental sine wave of the the average voltage signal.

The open-circuit voltage is the input to the lock-in amplifier, and the pulses are at a 10 times higher frequency than the lock-in amplifier reference signal. Therefore, the lock-in amplifier will display the RMS value of the fundamental sine wave of the average voltage of the pulses, V_{avg}. This is a square wave at the mechanical chopper frequency with an amplitude V_{avg}. V_{oc} and V_{avg} are related by the duty cycle.

$$V_{oc} = \frac{V_{avg}}{D} \tag{6.3}$$

The relationship between the amplitude of a 50% duty cycle square wave and the RMS voltage of

the fundamental sine wave of its Fourier series is the following:

$$V_{avg} = \frac{V_{rms}\pi}{\sqrt{2}} \tag{6.4}$$

Therefore, V_{rms} and V_{oc} have the following relationship:

$$V_{oc} = \frac{V_{rms}\pi}{D\sqrt{2}} \tag{6.5}$$

This equation is also valid with for the CW laser as well, in which case, $D = 1$, and $\pi/\sqrt{2}$ can be estimated as $\sim$2.22.

In an alternative configuration using a pulsed laser, the mechanical chopper can be eliminated and the function generator sync output can be used as a reference for the lock-in amplifier. In this case the correction for V_{oc} is slightly different. Now there is no longer a distinction between the repetition rate and the modulation frequency, so $V_{oc} = V_{avg}$. However, the amplitude of the fundamental Fourier series sine wave remains dependent on the duty cycle. V_{oc} and V_{rms} are now related as follows:

$$V_{oc} = \frac{V_{rms}\pi}{\sqrt{2}sin(\pi D)} \tag{6.6}$$

For Eq. 6.6, when $D = 50\%$, $sin(\pi D) = 1$, the equation simplifies to Eq. 6.4 where $V_{oc} = V_{avg}$.

6.4 Open-Circuit Voltage Polarization Dependence

A bow tie antenna is expected to have a $\cos^2$ polarization response where 0° is illumination polarization aligned with the antenna axis and 90° is where the polarization is perpendicular to the antenna axis. However, during measurements of some TWD rectennas, I observed an off-axis response. This unexpected signal is a thermal response due to heating of the MIM junction from direct absorption in the TWD. The TWD is orientated perpendicular to the antenna axis, and has a length on the same order as the wavelength of the illumination. Therefore, the TWD can

act like a monopole antenna and absorb radiation directly. This type of absorption cannot excite the antisymmetric surface plasmon mode, discussed in Chapter 5, necessary for rectification, but can result in resistive heating. Since I do not apply any external bias to my devices, the thermal effect cannot be bolometric and must be due to the Seebeck effect. With the consideration of this additional absorption mechanism, the appropriate fit for the optical measurement will be based on the sum of a $\cos^2$ (polarization parallel to the antenna axis) and a $\sin^2$ (polarization perpendicular to the antenna axis) terms. One example is the Ni-NiO-TiO_2-Cr/Au diode optical response shown in Figure 6.6. This device has a relatively high zero-bias resistance and responsivity ($R_0 = 1.60$ kΩ and $\beta_0 = 0.79$ A/W) compared to the Nb_2O_5 diodes explored in Chapter 4.

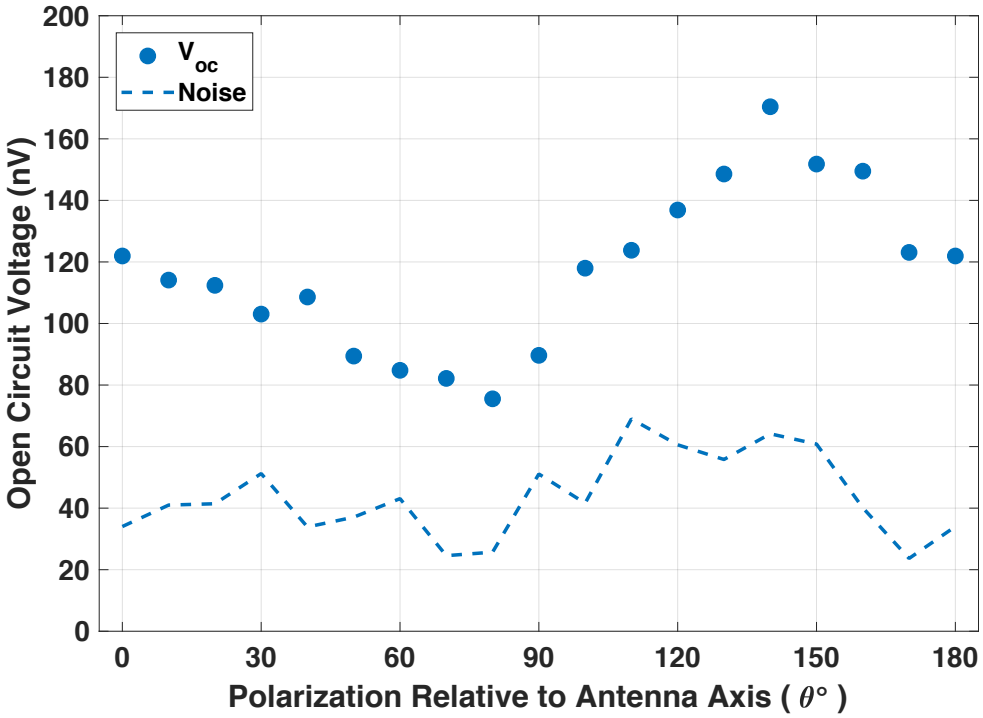

Figure 6.6: Combination rectification and Seebeck thermal TWD illumination open-circuit voltage response as a function of 10.6 μm illumination polarization for a Ni-NiO-TiO_2-Cr/Au TWD.

This device was measured with the CW laser, which has a maximum intensity of ~0.04 W/mm^2, and modulated by the mechanical chopper at 691 Hz. The open-circuit voltage response

is represented by the blue circles, and the noise level by the dashed line. Upon first examination, this voltage response doesn't appear to represent either a $\cos^2$ or $\sin^2$ response. Therefore, in addition to the $\sin^2$ thermal response, I must account for several sources of angular shift to the polarization response. First, one comes from the alignment of the rectenna on the stage to the 0° polarization angle, which is done by eye through a microscope with 100× magnification. I refer to this angular shift as ϕ_{align}, and it will effect absorption in both the TWD and the antenna. I estimate that ϕ_{align} is within ±5°. Second, looking back at Chapter 4, some of the device SEMs, shown in Figure 4.8 have antennas with jagged edges due to fabrication non-uniformity. Simulations suggest that extreme cases of this unintentional antenna asymmetry can shift the antennas absorption response by as much as 30°. Practically, I expect ϕ_{ant} to be ±20°. Similar to ϕ_{ant}, there is possibly a shift for the TWD absorption too, ϕ_{twd}. Finally, since the rectenna response measurement takes anywhere from 30 to 90 minutes, the beam wander can also contribute some additional shift in the response peaks. Given the randomness of the beam wander, I cannot account for it in the optical response fit, and from Figure 6.4, the angular shift of the peaks appears to be minimal (±5°). Given these effects, the preferred fit of the optical response would be with the following equation:

$$V_{oc}(\theta) = A_{\parallel} cos(\theta + \phi_{ant} + \phi_{align})^2 + A_{\perp} sin(\theta + \phi_{twd} + \phi_{align})^2 \tag{6.7}$$

Since cosine and sine are identical functions phase shifted by 90°, it is difficult to establish an accurate confidence interval for fit coefficients where the angular shifts are not strictly independent as in Eq. 6.7. Therefore, I limit the angular shift to a single term, which limits the degrees of freedom and provides reasonable confidence intervals.

$$V_{oc}(\theta) = A_{\parallel} cos(\theta + \phi)^2 + A_{\perp} sin(\theta)^2 \tag{6.8}$$

I use Eq. 6.8 to fit the data in Figure 6.6 and get the following result with 95% confidence intervals listed in parenthesis.

$$A_{\parallel} = 138\ nV\ (129, 147) \qquad A_{\perp} = 95\ nV\ (85, 105) \qquad \phi = 13.1^{\circ}\ (9.8, 16.5) \qquad R^2 = 0.8249$$

I added the resulting fit line with the 95% confidence intervals to the data in Figure 6.6 and show the result below.

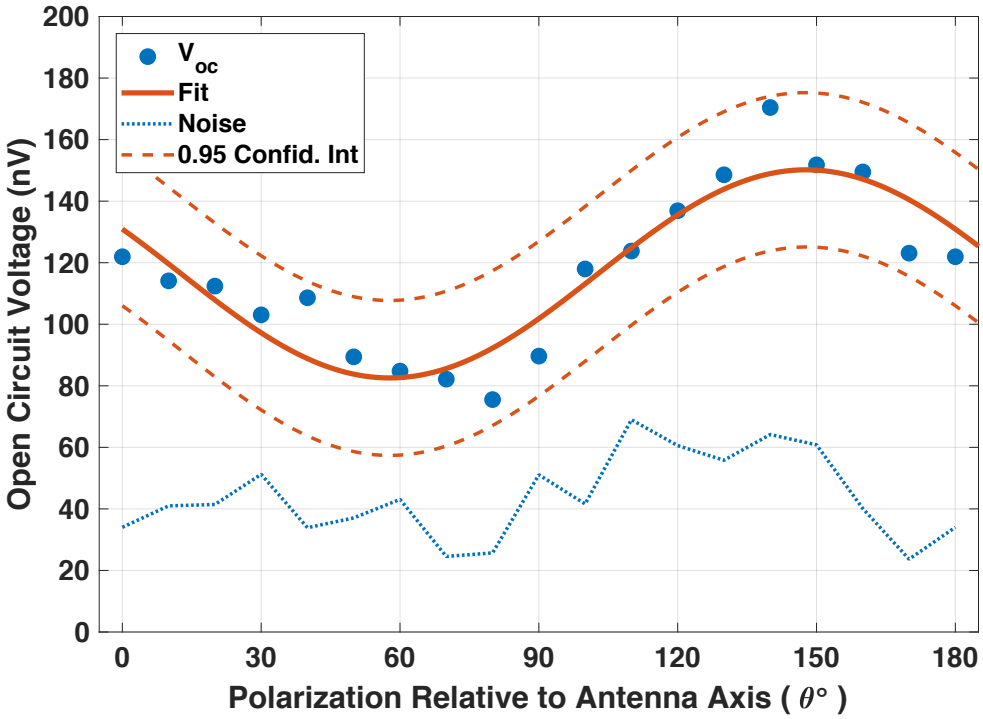

Figure 6.7: Open-circuit voltage response of Ni-NiO-TiO_2-Cr/Au TWD from Figure 6.6 fit to Eq. 6.8.

Clearly, given the high noise level in this data, there is quite a wide confidence interval. The wide confidence interval shown on the plot does not rule out a fit that is nearly flat versus polarization. Since $\sin^2 + \cos^2 = 1$, a flat response is theoretically possible in the case that $A_{\parallel} = A_{\perp}$ and ϕ=0°.

Ideally, I would like to eliminate the thermal response from the measurement. To prevent the lock-in amplifier from measuring the thermal response, the modulation frequency needs to be much

faster than the thermal time-constant. In Appendix C, I estimated the thermal time-constant, $\tau_{thermal}$, by estimating the heat capacity of the metal and the thermal resistance through the 300 nm of SiO_2. I estimate $\tau_{thermal}$=52 ns, which corresponds to a 19 MHz modulation frequency. In these measurements the mechanical chopper reference frequency is generally ∼1-2 kHz. Therefore, the thermal fluctuations are much faster than the low kHz modulation and cannot be eliminated from the measurement.

To confirm the proposed distinction between rectification and thermal Seebeck response, I built a metal-only TWD structure. I fabricated a 2 μm long TWD as described in Chapter 2, with the exception that the diode oxide processing steps were excluded. Without the oxides, the device has a very low resistance and liner $I(V)$ characteristic, this ensures this device cannot have a rectification response (Bareiß et al., 2013). Nor can it be bolometric because there is no external bias. Figure 6.8 shows the optical response of this device to the PWM laser with a 9% duty cycle and modulated by the mechanical chopper at 1.70 kHz.

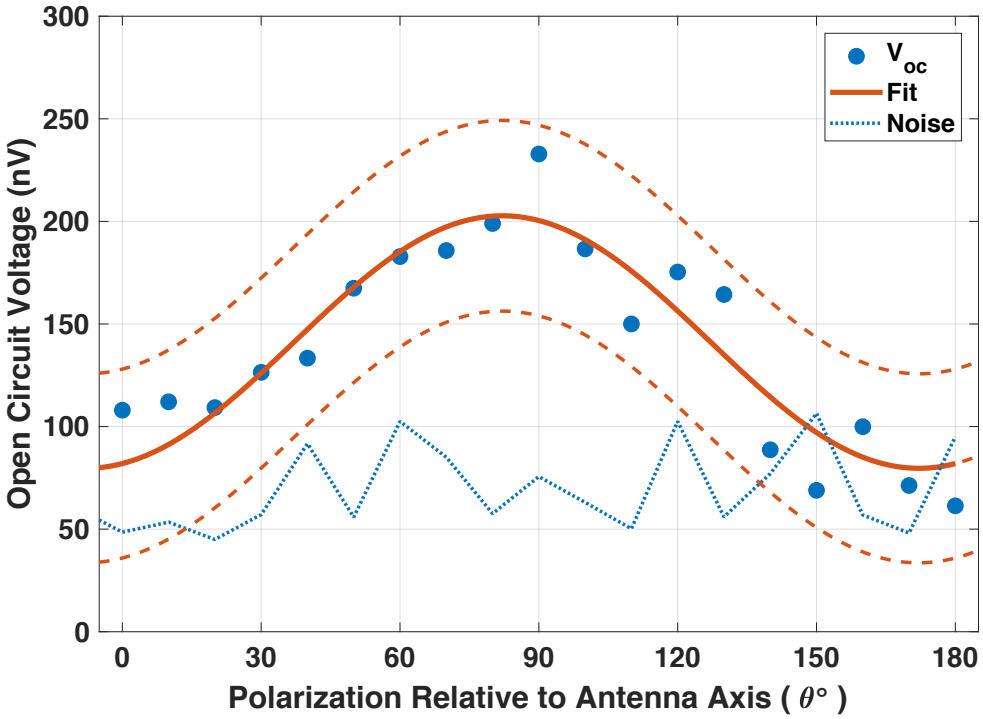

Figure 6.8: Metal-metal (Ni-Cr/Au) junction open-circuit voltage illumination response due to the Seebeck effect and direct heating of the traveling-wave region.

Since there is experimentally almost no $\cos^2$ response, I adjusted the fit equation (Eq. 6.8) so that the polarization shift term, ϕ, was part of the $\sin^2$ term rather than the $\cos^2$ term, as ϕ cannot have any meaningful effect if the amplitude coefficient is very small. Below I list the fit coefficients with the 95% confidence intervals in parenthesis:

$$A_{\parallel} = 85\ nV\ (69, 102) \quad A_{\perp} = 197\ nV\ (179, 215) \quad \phi = -11.5^{\circ}\ (-21.4, -1.8) \quad R^2 = 0.8312$$

As the figure shows, there is no on-axis response, only off-axis, as $A_{\parallel}$ is near the noise level of ~66.7 nV. This suggests that any heating in the antenna absorption is not strong enough to result in a thermal response, which supports the conclusion that the $\cos^2$ response from MIM TWD rectenna is indeed optical rectification. Direct heating due to off-axis absorption in the TWD, on

the other hand, can result in a thermal signal. Seebeck coefficients for Ni, Cr and Au are -15 μV/K, 22 μV/K, and 6.5 μV/K respectively (Moore et al., 1977). Therefore, it would only take a very small temperature difference, 0.03 K, to account for the voltages measured. The angular shift, ϕ, is within the expected range, and the coefficient of determination, R^2, is moderately close to 1, indicating this fit accurately represents the data.

6.5 Optical Measurement Results

In this section I present the infrared optical response of a lumped-element rectenna and four TWD rectennas. Of the TWD rectennas, one is 3 μm long (TWD1), two are $\sim$ 1.3 μm long (TWD2 and TWD3), and the final one (TWD4) is $\sim$1 μm long. I compare the measured response to the expected lumped-element response for a given diode, calculated as described in Appendix B. I expect that the measured lumped-element rectenna will have a response close to the predicted value, and the the TWD rectennas should have a higher response than the estimated lumped-element. Several optical measurement results have suggested that the relative dielectric constant for NiO is less than 8.5. For my lumped-element estimation I used a relative dielectric constant of 7. The simulation results in Chapter 5 suggest that the optimal TWD length is $\sim$500 nm. Unfortunately, given the concurrent nature of the experimental and modeling research, I do not have measurements for TWD rectenna with lengths in that range.

6.5.1 Lumped-Element Rectenna

To effectively analyze TWD rectenna performance, I use a lumped-element rectenna as a benchmark. The lumped-element rectenna was measured with the PWM laser at a 7% duty cycle, modulated by the mechanical chopper at 1.69 kHz. In Figure 6.9, I plot the V_{oc} response versus polarization angle. The raw data from the lock-in amplifier is corrected with Eq. 6.5 and plotted with the blue dots. The noise level, which is the reading from the lock-in (also corrected by Eq. 6.5) while the shutter was closed between different polarization responses, is the dotted blue line at $\sim$100 nV.

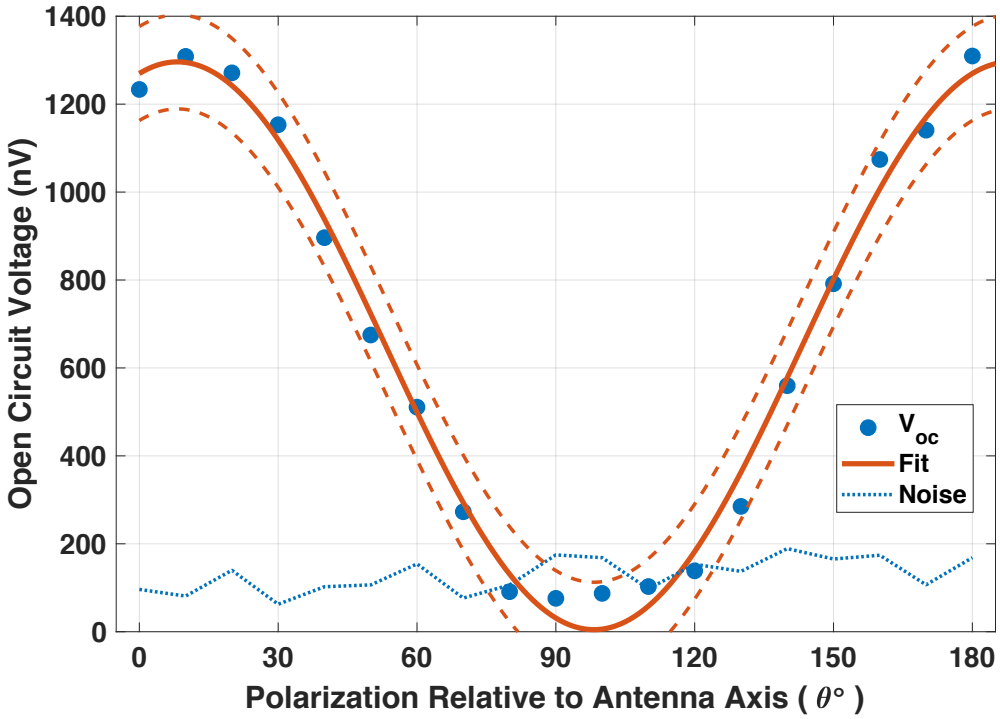

Figure 6.9: Lumped-element illumination open-circuit voltage response.

The data is fit using Eq. 6.8, resulting in the following fit coefficients, again with the 95% confidence intervals listed in parenthesis:

$$A_{\parallel} = 1296\ nV\ (1258, 1334) \quad A_{\perp} = 4.8\ nV\ (-37, 46) \quad \phi = -8.2^{\circ}\ (-9.7, -6.7) \quad R^2 = 0.9903$$

The off-axis response, $A_{\perp}$, is below the noise level of ~130 nV. The angular shift, ϕ, falls within the expected range, and R^2 value is very close to 1. The on-axis response, $A_{\parallel}$, is the open-circuit voltage, V_{oc}. The predicted open-circuit voltage for a lumped-element based on the calculations in Appendix B is 1196 nV. The measured value is within 10% of the estimate value which suggests the estimation technique in Appendix B is sufficiently accurate.

6.5.2 TWD1

This is the device reported in Pelz et al. (2016). There was a correction factor missing in this work due to the fact the source was a pulsed laser modulated by a mechanical chopper at 1.53 kHz. Thus, both the reported intensity and V_{oc} were low by a factor of 5, (Duty Cycle = 20%)$^{-1}$. Additionally, the optical setup had a 50-50 beam splitter that split the incident beam for real-time power monitoring. This reduced the illumination intensity by 50% compared to the other PWM laser optical measurements (Lumped-element, TWD2, and TWD3).

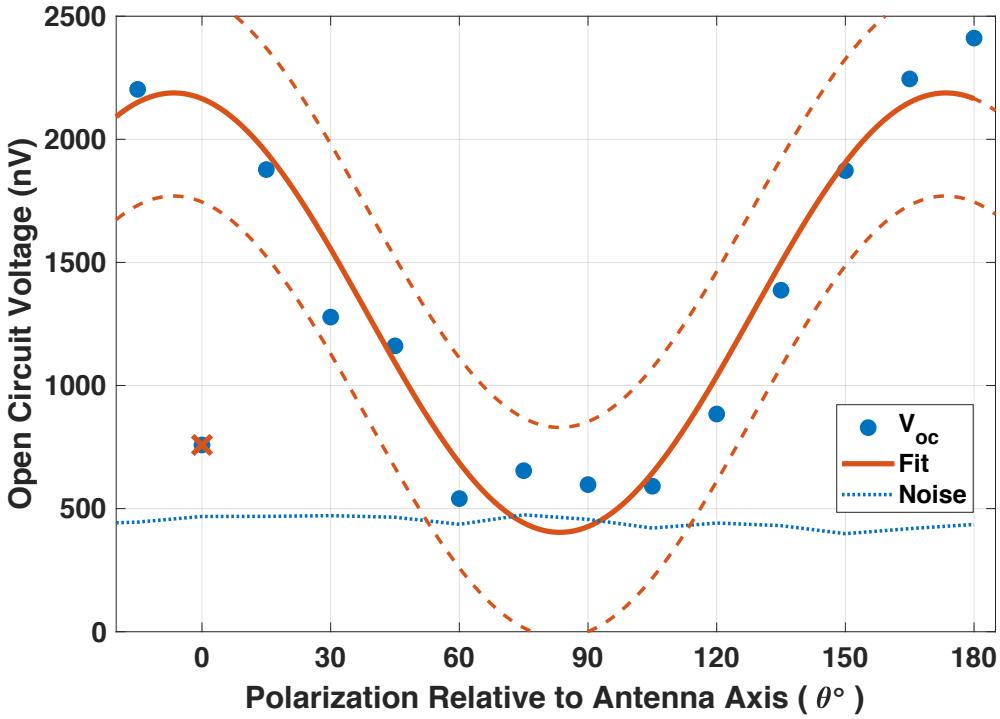

Figure 6.10: TWD1 illumination open-circuit voltage response.

In Figure 6.10, the 0° data has a much lower voltage than expected. The measurement is automated, so I was not present during the taking of this data, but I suspect that the home-made shutter being used at the time malfunctioned, and did not open for the part of the measurement. Therefore, that point was omitted from the fit as indicated by the red 'x'. This is the only measurement presented that was taken prior to upgrading the shutter to the ThorLabs SH05. The

resulting polarization response had the following fit coefficients:

$$A_{\parallel} = 2184\ nV\ (2011, 2357) \quad A_{\perp} = 408\ nV\ (217, 599) \quad \phi = 5.4^{\circ}\ (1.3, 9.4) \quad R^2 = 0.9387$$

Again, $A_{\perp}$ is near the noise level of 445 nV, this time however, the confidence interval is much wider, suggesting that it is possible that I have observed a small thermal response. The coefficient of determination, R^2 indicates a good fit, and ϕ is within the expected range. The predicted lumped-element response for this diode is only 146 nV. The substantially higher measured response ($\sim$14.9$\times$) is a good indication that the TWD structure is improving the impedance match to the antenna and enhancing the overall response.

6.5.3 TWD2

TWD2 has the cleanest response, with the highest R^2 and a very low noise level $\sim$39 nV. Figure 6.11 shows the 95% confidence intervals are very close to the fit line. This rectenna was measured with the PWM laser at a 20% duty cycle and modulated by the mechanical chopper at 1.69 kHz. The fit coefficients are as follows:

$$A_{\parallel} = 1224\ nV\ (1194, 1255) \quad A_{\perp} = 95\ nV\ (63, 128) \quad \phi = -4.3^{\circ}\ (-5.5, -3.0) \quad R^2 = 0.9918$$

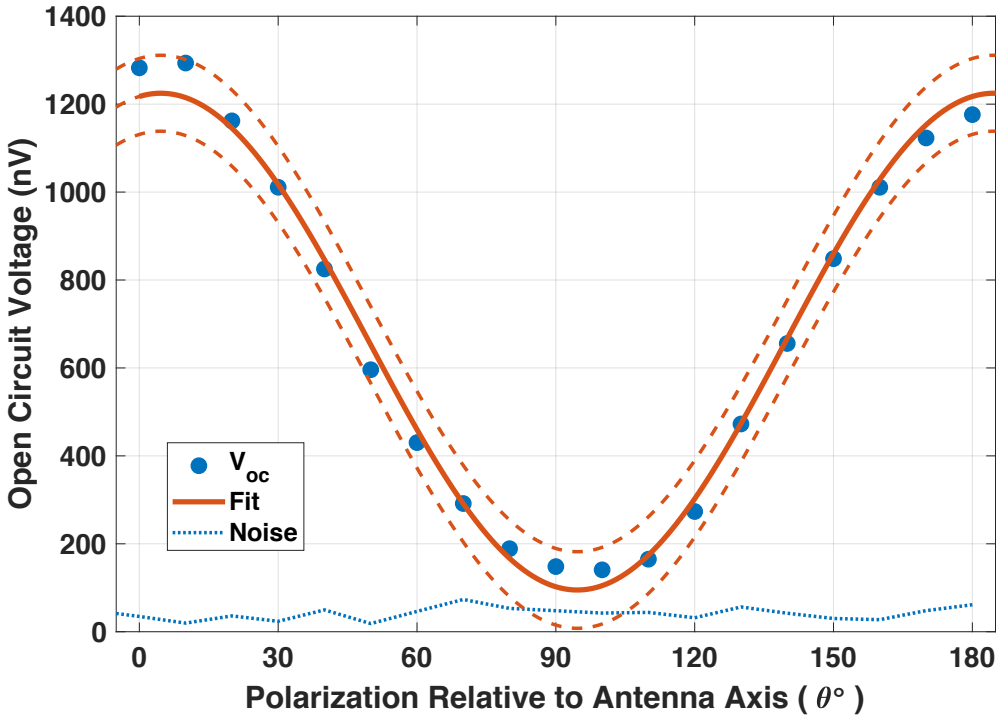

Figure 6.11: TWD2 illumination open-circuit voltage response.

Again, the thermal response is minimal, and the angular shift falls in a reasonable range. The estimated lumped-element response for this diode is only 87 nV. This makes the measured TWD response 14.1 times higher that the equivalent lumped-element.

6.5.4 TWD3

As Figure 6.12 shows, TWD3-Measurement A has the largest open-circuit voltage response of all infrared optical measurements, with $V_{oc} = 3055$ nV. I measured the device through 360° of polarization rotation. In the first 90°, the data shows, what appears to be, the negative effects of poor beam stability. Because of the stability explanation, the data was omitted from the fit, indicated by red x's on top of the data points.

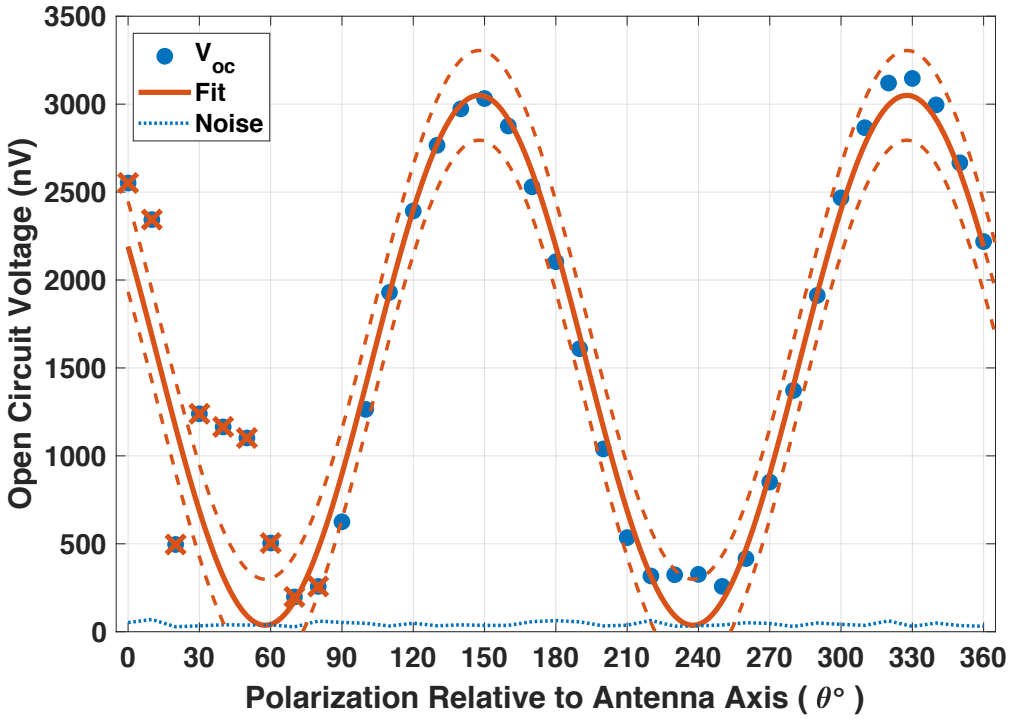

Figure 6.12: TWD3 illumination open-circuit voltage response - Measurement A.

Below, the resulting fit parameters, for the optical response in Figure 6.12 using Eq. 6.8:

$$A_{\parallel} = 3035\ nV\ (2944, 3127) \quad A_{\perp} = 51\ nV\ (-78.6, 181) \quad \phi = 31.9^{\circ}\ (30.1, 33.6) \quad R^2 = 0.9870$$

What we see from both the figure, and the fitting parameters, that there is a $\sim$32° angular shift in the polarization response. In Section 6.4, I discussed several issues that could account for a shift in the polarization response. However, 32° is larger than the expected maximum. The R^2 is extremely close to one, and the thermal signal, $A_{\perp}$, is at the noise level, $\sim$43 nV.

Given the large voltage magnitude, but questionable polarization dependence, I repeated the measurement several times. In contrast to the other optical measurements, the repeat measurements of TWD3 eliminated the mechanical chopper and used the sync from the function generator as the reference source for the lock-in amplifier with a repetition rate of 5 kHz and a duty cycle of 10%.

The response shown in Figure 6.13, while lower magnitude than the first measurement, has minimal shift relative to the expected $\cos^2$ response. The fit coefficients for the fit in Figure 6.13 are listed below:

$$A_{\parallel} = 928\ nV\ (896, 960) \quad A_{\perp} = 29\ nV\ (-5.7, 63) \quad \phi = -8.8^{\circ}\ (-10.6, -7.2) \quad R^2 = 0.9881$$

With an average noise level of 94 nV, the off-axis polarization response can be ignored. The rectification open-circuit voltage response is 928 nV, which is 8.4 times higher than the estimated response from an equivalent lumped-element rectenna of 110 nV.

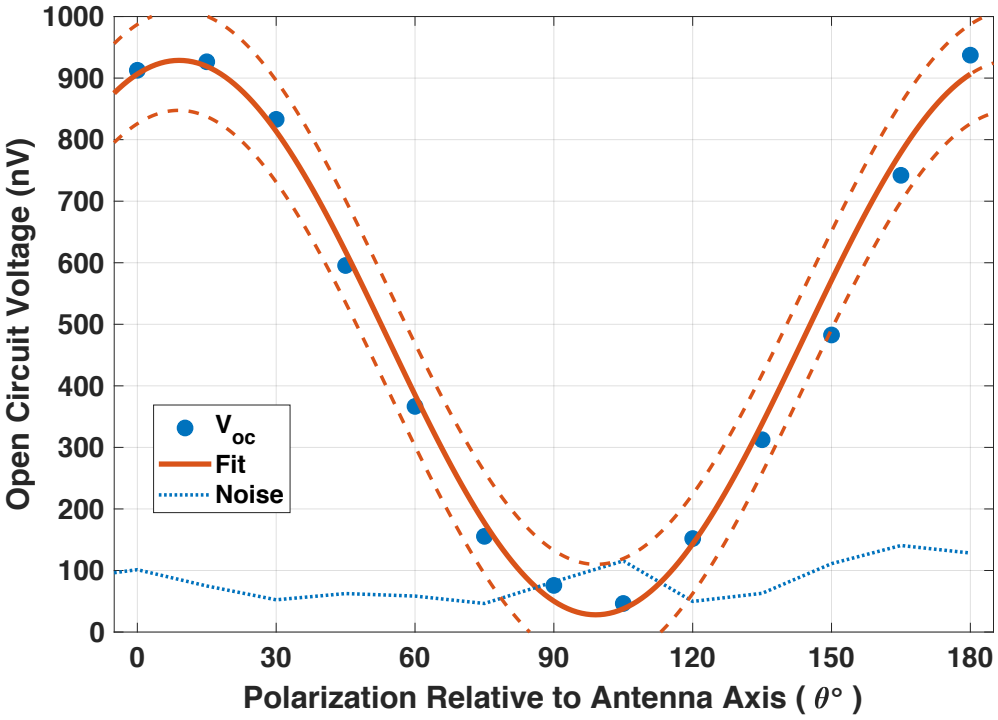

Figure 6.13: TWD3 illumination open-circuit voltage response - Measurement B.

Figure 6.14 shows a final measurement of TWD3. Just as with the previous measurement, the lock-in amplifier was locked directly to the PWM laser modulation signal at 5 kHz and 10%

duty cycle. There is a large difference between the 0° polarization response and the 180° response, roughly 40%. This is consistent with the effects of beam wander shown in Section 6.2.2. This is the only infrared rectenna measurement where beam wander had such a large effect. The fit coefficients for the fit in Figure 6.14 are listed below:

$$A_{\parallel} = 1617\ nV\ (1383, 1851) \quad A_{\perp} = 62.6\ nV\ (-189, 314) \quad \phi = 4.1°\ (-3.3, 11.4) \quad R^2 = 0.7919$$

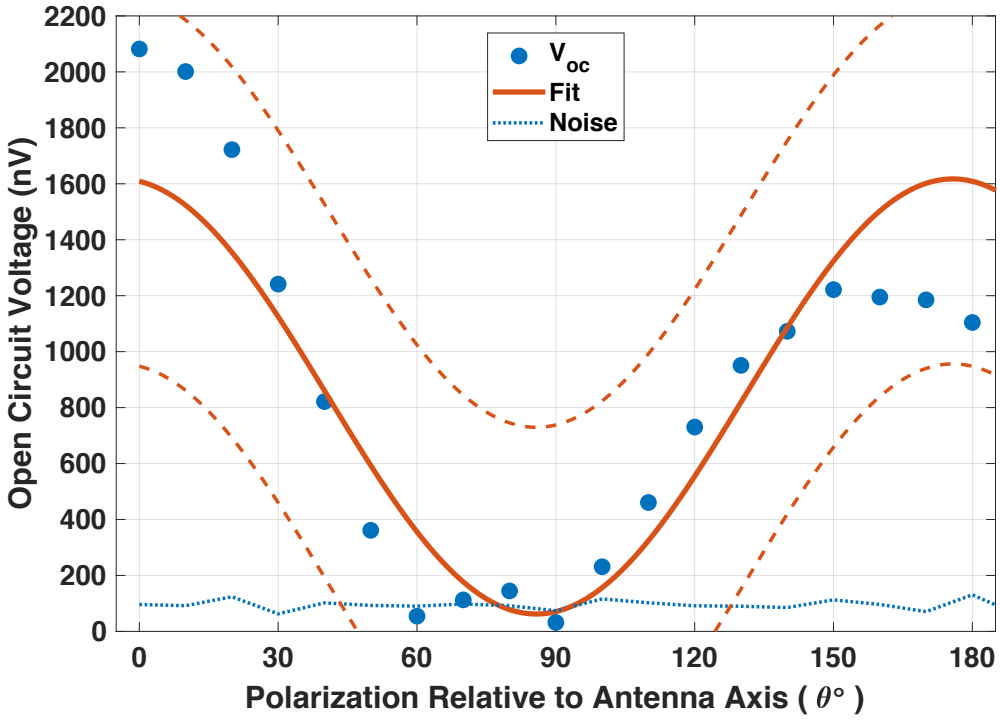

Figure 6.14: TWD3 illumination open-circuit voltage response - Measurement C.

The beam wander has led to quite wide 95% confidence intervals, but even with the wide intervals, the result fits within the bounds of the previous two measurements (A&B). The repeatability of the polarization responses adds confidence to the conclusion that I have observed 28 THz rectification with a TWD. Additionally, all three measurements exceed the calculated lumped-

element response of 110 nV. Going forward, I will use the average open-circuit voltage of 1860 nV as the observed response for TWD3, which is 16.9 times larger than the estimated lumped-element rectenna.

6.5.5 TWD4

This is the final TWD presented. It was measured with the CW laser and modulated by the mechanical chopper at 1.36 kHz. The lower open-circuit voltage from infrared optical measurement in Figure 6.15 reflects that the illumination intensity from the CW laser is 25 times lower than that of the PWM laser. The fit coefficients are as follows:

$$A_{\parallel} = 334\ nV\ (328, 340) \quad A_{\perp} = 28.6\ nV\ (21.8, 35.3) \quad \phi = -28.2^{\circ}\ (-29.1, -27.3) \quad R^2 = 0.9869$$

The off-axis response is near the average noise level of 19.4 nV, and the R^2 value is quite high. The shift in the polarization response is near the end of the range of acceptable values. As was done with TWD3, additional measurements would help confirm the response, however, the junction became open-circuited before those measurements could be performed. The TWD V_{oc} = 334 nV is 4.3 times larger than the estimated lumped-element open-circuit voltage response (78 nV).

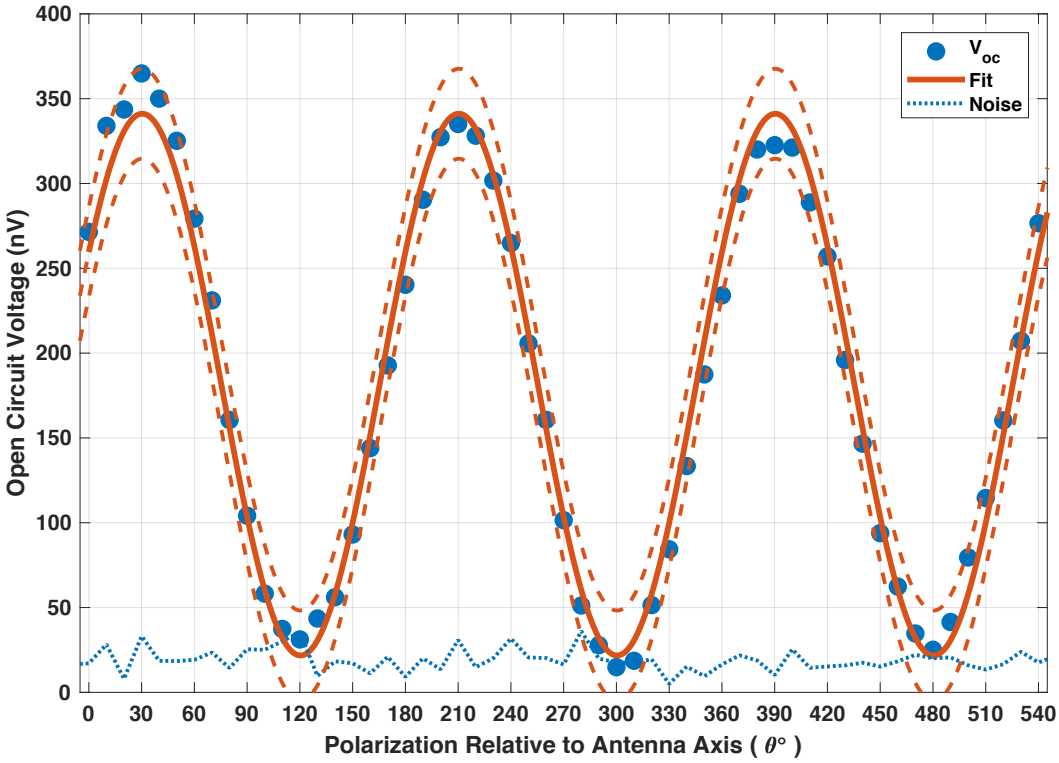

Figure 6.15: TWD4 illumination open-circuit voltage response

To summarize, all four measured TWD rectennas performed better than their estimated lumped-element counterparts. The detailed implications of these measurements are discussed in Chapter 7. However, preliminarily, given the TWD measured responses are approximately an order of magnitude higher than the estimated response from equivalent lumped-element diodes, the TWD can offer some performance improvement over its lumped-element counterpart. Similar performance across different TWD rectennas with different lead configurations shows that any absorption in the lead structure has a negligible effect.

Chapter 7

Discussion and Conclusion

7.1 Summary of Optical Measurement Results

Table 7.1 summarizes the optical measurements made in Chapter 6. As stated earlier, for comparison, I use Appendix B to calculate the estimated response for an equivalent area lumped-element diode. Additionally, I present simulation results for each device using the method from Chapter 5. I modified the relative dielectric constant used for NiO from 8.5 to 7 for both the lumped-element estimation and the TWD device simulation as simulated fits to experimental lumped-element results suggest it is lower than the value used for the simulation work in Chapter 5. I compare open-circuit voltage (V_{oc}), short-circuit current (I_{sc}), DC output power (P_{dc}), system responsivity (β_{sys}), detectivity (D^*), and overall efficiency (η_{total}) for the experimental measurement, the estimated lumped-element, and the TWD simulation. Details of the relationships between these metrics can also be found in Appendix B. The bottom two rows of the table show the ratio of the measured TWD to calculated equivalent lumped-element for both D^* and η_{total}. The D^* ratio is the same for V_{oc}, I_{sc}, and β_{sys}; the η_{total} ratio is the same for P_{dc}. For TWD3, I made multiple measurements, I show values based on the average open-circuit voltage of the three reported measurements.

There are several important conclusions from Table 7.1 listed below:

(1) The lumped-element estimation method is quite accurate. The measured lumped-element response is within ~10% of the estimated response (~20% for power terms because of the dependence on squared voltage or current). This estimation method has been con-

Table 7.1: Summary of lumped-element (LE) and TWD optical measurement results

		Device				
		LE	TWD1	TWD2	TWD3 (Averaged)	TWD4
Geometry	Length (nm)	400[a]	3000	1350	1250	1000
	Overlap (nm)	150[a]	30	115	110	30
DC	R_0 (Ω)	1151	559	381	429	743
	β_0 (A/W)	0.49	0.53	0.46	0.46	0.42
Laser Input	Laser	PWM	PWM	PWM	PWM	CW
	Pin (μW)	24	12	24	24	0.96
V_{oc} (nV)	**Measured[b]**	**1296**	**2184**	**1224**	**1860**	**334**
	LE calcuated	1196	146	87	110	78
	TWD simulated	x	3752	2297	1668	155
I_{sc} (nA)	Measured[c]	1.13	3.91	3.21	4.33	0.45
	LE calcuated	1.04	0.261	0.227	0.255	0.106
	TWD simulated	x	6.73	6.03	3.87	0.21
P_{dc} (aW)	Measured[c]	365	2130	983	2016	37.5
	LE calcuated	311	9.55	4.92	7.03	2.1
	TWD simulated	x	6290	3460	1610	8.1
β_{sys} (μA/W)	Measured[c]	47	325	134	180	471
	LE calcuated	43	22	9	11	110
	TWD simulated	x	558	251	161	219
D^* (Jones) (cm $\sqrt{Hz}$W^{-1})	Measured[c]	6.03×10^3	2.89×10^4	9.95×10^3	1.42×10^4	4.88×10^4
	LE calcuated	5.59×10^3	1.96×10^3	7.03×10^2	8.41×10^2	1.14×10^4
	TWD simulated	x	5.03×10^4	1.87×10^4	1.27×10^4	2.26×10^4
η_{total} ($\times10^{-12}$)	Measured[c]	15.5	177	41.0	83.6	39.4
	LE calcuated	12.9	0.80	0.21	0.29	2.15
	TWD simulated	x	524	144	67	8.48
D^* (Measured[c]/LE$_{calc}$)		**1.08**	**14.9**	**14.1**	**16.9**	**4.28**
P_{dc} (Measured[c]/LE$_{calc}$)		**1.16**	**222**	**199**	**286**	**18.3**

[a] area is ~0.7×length×overlap for the LE because of the severe rounding of the corners.
[b] measured by the lock-in amplifier.
[c] calculated from measured V_{oc} as shown in Appendix B.

sistent with other lumped-element infrared illumination measurements made by other lab members.

(2) TWD rectennas have a response that is ∼5-20 times larger than the estimated lumped-element of an equivalent size and $I(V)$ characteristic. This, in conjunction with the first point, indicates that the observed response is a traveling-wave optical response; the TWD configuration improves coupling between the antenna and the diode. This is also consistent with the expected improvement based on simulation results as shown by Figure 7.1. Simulation of TWDs with overlaps from 60 nm to 120 nm generally predict improvements over lumped-element rectennas by factors ∼5-25, with the improvement factor increasing for longer TWD lengths (i.e., larger device areas, which quickly reduce the expected lumped-element response due to reduced coupling efficiency). Unfortunately, I do not have enough experimental data to confirm the resonant trends suggested by the simulation results. However, Figure 7.1 shows an approximate agreement between experimental and simulation results.

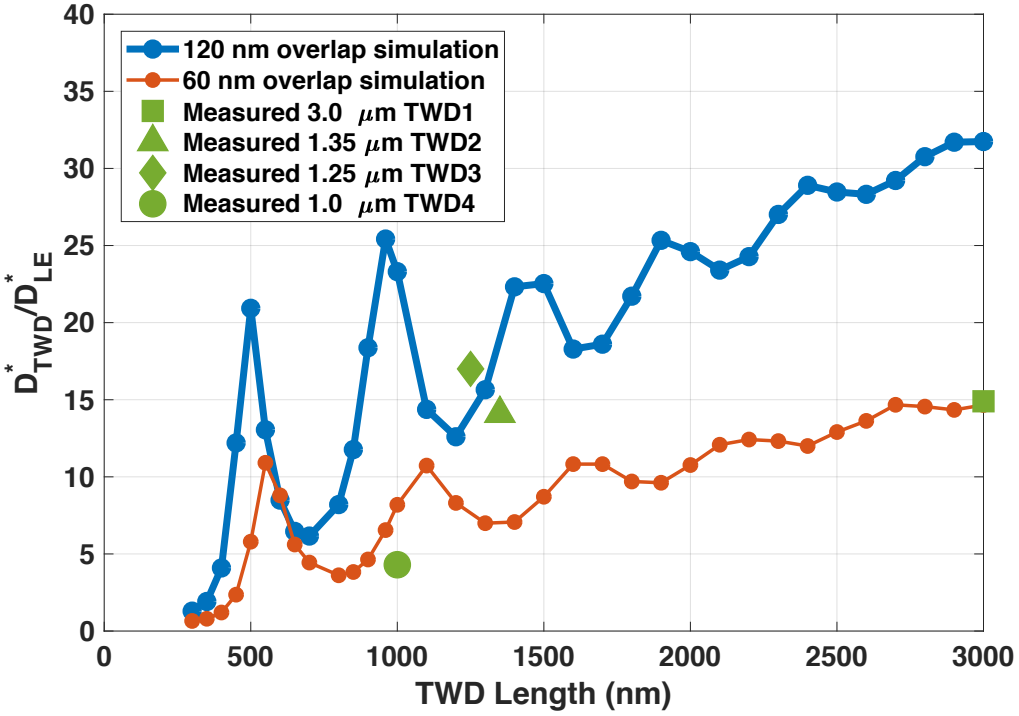

Figure 7.1: Simulated and experimental ratio of TWD to lumped-element (LE) detectivity (D^*) versus the length of the TWD. The measured overlap for experimental devices ranges from 30 nm to 115 nm, see Table 7.1.

(3) All of the measured TWD rectennas have higher detectivies, by factors ranging from 1.65 to 8.09, than the measured lumped-element. This also indicates that the TWD configuration enhances antenna/diode coupling and improves rectenna performance.

(4) The simulation method in Chapter 5 estimates the actual TWD response generally within a factor of ∼2. This is another indication that the fabricated devices are preforming as intended, rather than simply coupling to the antenna like a lumped-element diode. The deviation of simulated values from measured ones likely originates from small differences in the simulated and fabricated structures. In the simulation, any given TWD has a uniform junction width along its entire length. The experimental devices on the other hand, as shown in Figures 4.6 and 4.8, the overlap region starts at zero and gradually increases to

the reported width (over a distance of ∼100 nm). The effect of this tapered region might provide insight to possible design improvements (see Section 7.3). Likewise, the estimated insulator thickness could be different from the actual values, and the DC $I(V)$ curve may deviate from the $I(V)$ characteristic at high frequency. All of these variations can add up to account for the difference between the simulated and measured values.

I have shown that a Ni-NiO-Nb_2O_5-Cr/Au rectenna in a TWD configuration can improve the response of a MIM rectenna compared to its lumped-element counterpart. The TWD achieves this by modifying the impedance seen by the antenna from a parallel RC of the MIM diode to the input impedance of a TWD transmission line. This modification results in a much higher coupling efficiency. For example, the highest detectivity from a simulated TWD (t=5 nm, t_m=60 nm, L_{twd}=550 nm) has an estimated coupling efficiency of 50% and the estimated equivalent area lumped-element has a coupling efficiency of 3×10^{-4}. This makes the TWD coupling efficiency nearly 1700 times higher than the lumped-element rectenna. Yet the estimated detectivity improvement from Figure 7.1 is only ∼11. The TWD improvement over the lumped-element is limited by the fact that despite the higher coupling efficiency, there is an additional loss mechanism: the propagation of the surface plasmon along the MIM interface. The thin insulator required to support electron tunneling leads to very high field confinement and lossy plasmonic propagation. In a lumped-element rectenna, once the AC power enters the diode, all of it is available to be rectified. Alternatively, in a TWD, since all the rectification does not occur at the same location, the field that couples to the diode must still propagate along the MIM interface, and this propagation loss becomes costly.

Given the enhancement of the TWD structure is not as large as initially projected, it is possible there are cases where the TWD is actually worse than its lumped-element counterpart. For example, Al_2O_3 has a very low dielectric constant at 10.6 μm. This low dielectric constant reduces the plasmonic resistive decay loss in the TWD, but also means the capacitance of a Al_2O_3 based MIM lumped-element rectenna will be quite low. If the coupling between the antenna and

lumped-element diode is high enough, it is possible the improvement in coupling efficiency for the TWD will not outweigh the cost of propagation loss. In this case, the lumped-element will out perform the corresponding TWD for that material set.

7.2 Comparison to Other Detectors

Aside from rectennas, there are a few other common options for detection of 10.6 μm radiation: low bandgap photodiodes, microbolometers and strained superlattice detectors. Using cryogenic cooling, detectivities in the range of 10^8-10^{10} Jones have been reported (Rogalski, 2002, 2010; Ting et al., 2009; Plis, 2014). The need for cryogenic cooling adds substantially to the cost of such detectors and limits practical application. Therefore, it is desirable to have efficient room temperature infrared detectors, and it can be misleading to compare the detectivies of cryogenic detectors to ones that operate at room temperature.

Microbolometers at room temperature have been reported to have detectivies around 10^7 Jones (Chi-Anh et al., 2005). In Chapter 6 I used an uncooled HgCdTe photodiode for laser beam characterization measurements. This photodiode has a detectivity of 1.5×10^7 Jones, a responsivity of 3.2 mA/W, and an absorption area of 1 mm^2. In Appendix D, I confirm the responsivity by measuring the photodiode with the same optical measurement setup as used for the MIM rectennas. Below is a table that summarizes the detection characteristics of the TWD compared with the alternative room temperature detectors. (Zhu et al., 2014)

Table 7.2: Detector comparison: TWD, photodiode, bolomter, and graphene geometric diode

	Detector Type				
	Simulated TWD	Experimental TWD	Boston Electronics Photodiode HgCdTe	Bolometer	Geometric Diode Rectenna
D* (Jones) (or cm$\sqrt{Hz}$W^{-1})	6×10^4	4.9×10^4	1.5×10^7	1.1×10^7	$(\sim 5 \times 10^4)^a$
$\sqrt{A_d}$	4.9 μm	4.9 μm	1000 μm	70 μm	6.1 μm
$I_n(\Delta f)^{-0.5}$	2.06 pA	4.72 pA	21 pA	4.38^b pA	2.35 pA
β_{sys}	0.239 mA/W	0.471 mA/W	3.2 mA/W	6.9^b mA/W	0.20 mA/W
R_d	3,921 Ω	743 Ω	37 Ω	27,000 Ω	3,000 Ω

[a] Corrected from published value based on correctly reported β_{sys}.

[b] Calculated from bias current and device resistance as shown in Appendix B.

The TWD rectenna yields detectivies similar to those for the geometric diode but a couple hundred times lower than photodiodes or bolometers. However, there is a $\sqrt{Area}$ factor in the calculation of detectivity, see Eq. B.10. The substantially smaller absorption area of a rectenna (compared to either a photodiode or a bolometer) accounts for the majority of the difference. Simply employing an array of TWD rectennas to achieve a larger area will yield a higher detectivity. When the area of the detector is ignored, I observe TWD system responsivitys that are within ~10 of the photodiode and bolometer. Rectennas have an additional advantage over bolometers of a much faster response time. Given the possible improvements for infrared rectennas (TWD or alternatives) outlined in the following section, rectennas have the potential to surpass existing technology.

7.3 Potential TWD Rectenna Improvements

7.3.1 Increase Electric Field

Increasing the electric filed in the diode provides a higher AC voltage to the MIM interface. MIM diodes become more nonlinear and asymmetric at higher voltages. Therefore, the efficiency of the diode rectification is improved with a higher voltage input. There are several ways to achieve higher electric field intensity.

(1) **Double antenna:** A second antenna can be added to the open end of the TWD. In this way, two surface plasmon waves will be launched down the TWD, one from each end, propagating in opposite directions. Since the waves are propagating in opposite directions, there will be both constructive and destructive interference, regardless of the phase relationship of the illumination to each antenna. The net result will be a higher field intensity and more efficient rectification.

(2) **Tapered TWD:** In this I explored the effects of length and width independently. Tapering the TWD overlap region, at either the beginning or the termination of the TWD, can potentially help tune the diode input impedance as well as enhance field confinement. Better impedance control will allow for higher coupling between the antenna and the diode and enhanced field confinement will lead to higher AC voltages and more efficient rectification.

(3) **Better antenna:** My work focused mainly the TWD design. I performed basic antenna analysis, but design was held constant. Antenna optimization can improve the antenna in several ways. First, since the antenna is illuminated from the low index side, the directivity is poor. Embedding the antenna in a higher index material and matching to free space can increase the amount of optical power absorbed by the antenna. Second, just as I engineered the TWD impedance characteristics, the antenna's impedance can be engineered as well. Finally, the SiO_2 can be grown to a thickness so that it is quarter-wave matched for the illumination wavelength providing enhanced antenna absorption (Tiwari et al., 2009).

(4) **MIM surface roughness:** A better understanding of the effects of MIM surface roughness on TWD plasmonic propagation. Intuitively, the rough interfaces likely inhibit the plasmon propagation, but a specific study to quantify this effect would help optimize TWD rectenna performance.

7.3.2 Decrease Plasmonic Resistive Decay Loss

One potential way to decrease plasmonic resistive decay loss is to add sharp metal tips inside the TWD MIM insulator. This would allow the insulator to become thicker (reduced plasmonic resistive decay loss), while the electron tunneling can be confined to small areas at the sharp tips. The primary limitation here is the ability to fabricate such a structure. Despite demonstrations of single sharp tips with MIM structures (Choi et al., 2009; Miskovsky et al., 2012; Piltan and Sievenpiper, 2017), I do not know of any way that could be reliably fabricate sharp tips within a TWD.

A second option is to load a lumped-element diode at the feed point of an antenna with a low-loss, transmission line matching structure to compensate for the capacitance of the diode. In this way, the impedance mis-match between the antenna and lumped-element diode can be compensated in a low-loss way. This concept begins to deviate from the original TWD concept, as it is no longer a rectifying transmission line. However, similar to the improved coupling efficiency I demonstrated with the TWD, this concept utilizes a transmission line structure for improved impedance matching between the antenna and diode.

7.3.3 Better Diodes

Most importantly, improving the MIM diode. Examining the MIM diode $I(V)$ curves, clearly there is room for improvement. With the low resistance diodes I fabricate, the maximum asymmetry I observe is less than 2 over the entire measured voltage range (several hundred millivolts). Enhanced diode asymmetry and nonlinearity will improve overall rectification. Experimentation with different materials and improved deposition techniques can potentially improve the MIM diode

$I(V)$ characteristics.

7.4 Measurement Improvements

While improving the performance of the rectenna is the primary goal, improving the optical measurement configuration can help achieve that goal. More accurate measurement will enhance feedback on specific design choices and allow for better comparison between rectenna devices. For example, simulations in Chapter 5 suggest shorter devices should have a higher response. However, experimentally, I do not have enough data to confirm or refute this observation.

(1) **Direct lock-in to laser:** Modulating a pulsed laser near the repetition rate is a less-than-ideal way to make these measurements. With the ∼2 kHz modulation frequency and the 20 kHz repetition rate, the variation of the power to the recetnna could as much as 20% each cycle of the the mechanical modulation based on the number of pulses that pass through the chopper each cycle. Preliminary testing with our current SYNRAD laser appears this is an option without any equipment upgrades and is the preferred measurement technique moving forward.

(2) **Faster modulation:** While the rectennas measured in this work appear to be genuinely rectifying the 10.6 μm radiation, there are only two ways to rule out a thermal response: increase the modulation frequency or laser mixing. Both of which would require substantial measurement system upgrades. Increasing the modulation rate above the thermal time constant will eliminate thermal signals from the measurement. Given the thermal time constant is in the megahertz, there are two options for increasing the modulation rate: replace the mechanical chopper with an acousto-optic modulator or direct lock-in to a pulsed laser with a megahertz repetition rate. As stated by the first point, the preferred method would be to lock into the laser modulation.

(3) **Non-reflecting wafer holder:** In this work, the devices were mounted on a metallic, re-purposed, SEM stage for the optical measurement. This means the beam that illuminates

the device is reflected off the stage back through the substrate an could cause distortion in the measurement.

(4) **Better laser stability:** Clearly, from the data presented in Chapter 6, the laser stability can cause errors in the measurement. Any inaccuracy in measured beam size and intensity will manifest as uncertainty in calculated performance metrics. Switching to a laer with better stability will improve the measurement accuracy.

(5) **High frequency diode $I(V)$ measurement:** I use the DC $I(V)$ characterization to make predications about the high-frequency performance. It is well established that the dielectric constants of these materials can vary at optical frequencies, so it is likely the $I(V)$ characteristics vary as well. Unfortunately, without terahertz electronics, there is no way to measure an $I(V)$ at THz frequencies.

(6) **Illuminated $I(V)$ measurement:** Because of the resistive lead structure connecting my electrical probes to my TWD devices, I could not make short-circuit current measurements. Changes to the probe configuration could possibly allow for short-circuit current measurements or full illuminated $I(V)$ sweeps. This could confirm the accuracy of my linear approximation of the illuminated $I(V)$ curve.

7.5 Final Thoughts

TWD rectennas do provide an improvement over lumped-element rectennas. Table 7.1 shows that I observed higher detectivity and efficiency for all of the measured TWD rectennas than the experimentally measured lumped-element device. However, the enhancement is not as large as initially projected because of the additional loss associated with plasmonic decay. Even with substantial innovation, TWDs probably will not achieve the efficiencies necessary to be effective energy harvesters, but may be practical for detection with some additional development.

Despite the limitations of the TWD rectenna, the knowledge gained through fabricating, measuring and analysis TWD recetnna performance can provide insight for future infrared rectenna

work. I have confirmed through simulation and experimentation that MIM diode rectennas are not fundamentally limited by the capacitive nature of the diode. I have shown that the diode can in fact be modified to achieve a high coupling efficiency to the antenna. This means infrared optical rectennas with some alternative, low-loss, compensation structure should show promise as energy harvesters.

Bibliography

Bailey, R. L. (1972). A proposed new concept for a solar-energy converter. Journal of Engineering for Power, 94(2):73–77.

Bareiß, M., Krenz, P. M., Szakmany, G. P., Tiwari, B. N., Kalblein, D., Orlov, A. O., Bernstein, G. H., Scarpa, G., Fabel, B., Zschieschang, U., et al. (2013). Rectennas revisited. IEEE Transactions on Nanotechnology, 12(6):1144–1150.

Bean, J. A., Tiwari, B., Bernstein, G. H., Fay, P., and Porod, W. (2009). Thermal infrared detection using dipole antenna-coupled metal-oxide-metal diodes. Journal of Vacuum Science & Technology B, 27(1):11–14.

Bean, J. A., Weeks, A., and Boreman, G. D. (2011). Performance optimization of antenna-coupled tunnel diode infrared detectors. IEEE Journal of Quantum Electronics, 47(1):126–135.

Chi-Anh, N., Shin, H.-J., Kim, K., Han, Y.-H., and Moon, S. (2005). Characterization of uncooled bolometer with vanadium tungsten oxide infrared active layer. Sensors and Actuators A: Physical, 123:87–91.

Choi, K., Dagenais, M., and Peckerar, M. M. (2009). Fabrication of a thin film asymmetric tunneling diode using geometric field enhancement. In Semiconductor Device Research Symposium, 2009. ISDRS'09. International, pages 1–2. IEEE.

Choi, K., Yesilkoy, F., Chryssis, A., Dagenais, M., and Peckerar, M. (2010). New process development for planar-type cic tunneling diodes. IEEE Electron Device Letters, 31(8):809–811.

Choi, K., Yesilkoy, F., Ryu, G., Cho, S. H., Goldsman, N., Dagenais, M., and Peckerar, M. (2011). A focused asymmetric metal–insulator–metal tunneling diode: fabrication, dc characteristics and rf rectification analysis. IEEE Transactions on Electron Devices, 58(10):3519–3528.

Dagenais, M., Choi, K., Yesilkoy, F., Chryssis, A. N., and Peckerar, M. C. (2010). Solar spectrum rectification using nano-antennas and tunneling diodes. In OPTO, pages 76050E–76050E. International Society for Optics and Photonics.

Dodd, L. E., Shenton, S. A., Gallant, A. J., and Wood, D. (2015). Improving metal-oxide-metal (mom) diode performance via the optimization of the oxide layer. Journal of Electronic Materials, 44(5):1361–1366.

Eliasson, B. J. (2001). Metal-insulator-metal diodes for solar energy conversion. PhD thesis, University of Colorado.

Estes, M. J. and Moddel, G. (2006). Surface plasmon devices. US Patent 7,010,183.

Forsythe, G. E., Moler, C. B., and Malcolm, M. A. (1977). Computer methods for mathematical computations. Englewood Cliffs, NJ: Prentice-Hall.

Gadalla, M., Abdel-Rahman, M., and Shamim, A. (2014). Design, optimization and fabrication of a 28.3 thz nano-rectenna for infrared detection and rectification. Scientific Reports, 4 (2014).

Grover, S., Dmitriyeva, O., Estes, M. J., and Moddel, G. (2010). Traveling-wave metal/insulator/metal diodes for improved infrared bandwidth and efficiency of antenna-coupled rectifiers. IEEE Transactions on Nanotechnology, 9(6):716–722.

Grover, S. and Moddel, G. (2011). Applicability of metal/insulator/metal (mim) diodes to solar rectennas. IEEE Journal of Photovoltaics, 1(1):78–83.

Grover, S. and Moddel, G. (2012). Engineering the current–voltage characteristics of metal–insulator–metal diodes using double-insulator tunnel barriers. Solid-State Electronics, 67(1):94–99.

Hartman, T. E. (1962). Tunneling of a wave packet. Journal of Applied Physics, 33(12):3427–3433.

Hashem, I. E., Rafat, N. H., and Soliman, E. A. (2014). Dipole nantennas terminated by traveling wave rectifiers for ambient thermal energy harvesting. IEEE Transactions on Nanotechnology, 13(4):767–778.

Heiblum, M., Wang, S., Whinnery, J., and Gustafson, T. (1978). Characteristics of integrated mom junctions at dc and at optical frequencies. IEEE Journal of Quantum Electronics, 14(3):159–169.

Herner, S., Belkadi, A., Weerakkody, A., Pelz, B., and Moddel, G. (2017a). Responsivity-resistance relationship in MIIM diodes. Submitted for publication.

Herner, S., Weerakkody, A., Belkadi, A., and Moddel, G. (2017b). High performance MIIM diode based on cobalt oxide/titanium oxide. Applied Physics Letters, 110(22):223901.

Hobbs, P. C., Laibowitz, R. B., and Libsch, F. R. (2005). Ni–nio–ni tunnel junctions for terahertz and infrared detection. Applied optics, 44(32):6813–6822.

Hobbs, P. C., Laibowitz, R. B., Libsch, F. R., LaBianca, N. C., and Chiniwalla, P. P. (2007). Efficient waveguide-integrated tunnel junction detectors at 1.6 μm. Optics express, 15(25):16376–16389.

Joshi, S. (2015). Performance limits of optical rectennas. PhD thesis, University of Colorado at Boulder.

Joshi, S. and Moddel, G. (2015). Rectennas at optical frequencies: How to analyze the response. Journal of Applied Physics, 118(8):084503.

Knight, M. W., Sobhani, H., Nordlander, P., and Halas, N. J. (2011). Photodetection with active optical antennas. Science, 332(6030):702–704.

Kreyszig, E. (2006). Advanced Engineering Mathematics. John Wiley & Sons, Columbus.

Lei, X. and Van, V. (2013). Fdtd modeling of traveling-wave mim diode for ultrafast pulse detection. Optics Communications, 294:344–350.

Maraghechi, P., Foroughi-Abari, A., Cadien, K., and Elezzabi, A. (2011). Enhanced rectifying response from metal-insulator-insulator-metal junctions. Applied Physics Letters, 99(25):253503.

Maraghechi, P., Foroughi-Abari, A., Cadien, K., and Elezzabi, A. (2012). Observation of resonant tunneling phenomenon in metal-insulator-insulator-insulator-metal electron tunnel devices. Applied Physics Letters, 100(11):113503.

Miskovsky, N. M., Cutler, P. H., Mayer, A., Weiss, B. L., Willis, B., Sullivan, T. E., and Lerner, P. B. (2012). Nanoscale devices for rectification of high frequency radiation from the infrared through the visible: a new approach. Journal of Nanotechnology, 2012.

Moore, J., Williams, R., and Graves, R. (1977). Thermal conductivity, electrical resistivity, and seebeck coefficient of high-purity chromium from 280 to 1000 k. Journal of Applied Physics, 48(2):610–617.

Muehlschlegel, P., Eisler, H.-J., Martin, O. J., Hecht, B., and Pohl, D. (2005). Resonant optical antennas. science, 308(5728):1607–1609.

Nagae, M. (1972). Response time of metal-insulator-metal tunnel junctions. Japanese Journal of Applied Physics, 11(11):1611.

Neil, H. et al. (1969). Microwave to dc converter. US Patent 3,434,678.

Nicol, A. H. (2005). Grating coupled surface plasmon enhanced fluorescence spectroscopy. Dizertační práce, univerzita Mainz.

Novotny, L. and Van Hulst, N. (2011). Antennas for light. Nature photonics, 5(2):83–90.

Ozkan, E. G., Inac, M., Shafique, A., Ozcan, M., and Gurbuz, Y. (2016). The metal-insulator-metal diodes for infrared energy harvesting and detection applications. In SPIE Defense+ Security, pages 98190F–98190F. International Society for Optics and Photonics.

Palik, E. D. (1998). Handbook of optical constants of solids, volume 3. Academic press.

Pelz, B., Belkadi, A., and Moddel, G. (2016). Traveling-wave metal-insulator-metal diodes for infrared rectennas. IEEE Photovoltaic Specialist Conference (2016).

Pelz, B., Belkadi, A., and Moddel, G. (2017). Avoiding erroneous analysis of mim diode current-voltage characteristics: Exponential fitting. Submitted for publication.

Piltan, S. and Sievenpiper, D. (2017). Optical rectification using geometrical field enhancement in gold nano-arrays. Journal of Applied Physics, 122(18):183101.

Plis, E. A. (2014). Inas/gasb type-ii superlattice detectors. Advances in Electronics, 2014.

Rogalski, A. (2002). Infrared detectors: an overview. Infrared Physics & Technology, 43(3):187–210.

Rogalski, A. (2003). Infrared detectors: status and trends. Progress in quantum electronics, 27(2):59–210.

Rogalski, A. (2010). Infrared detectors. CRC press.

Sabaawi, A. M., Tsimenidis, C. C., and Sharif, B. S. (2013). Characterization of coupling and quantum efficiencies in solar rectennas. In Antennas and Propagation Conference (LAPC), 2013 Loughborough, pages 363–368. IEEE.

Sanchez, A., Davis Jr, C., Liu, K., and Javan, A. (1978). The mom tunneling diode: theoretical estimate of its performance at microwave and infrared frequencies. Journal of Applied Physics, 49(10):5270–5277.

Sayed, I. E. H., Rafat, N. H., and Soliman, E. A. (2015). Harvesting thermal infrared emission using nanodipole terminated by traveling wave rectifier. In Antennas and Propagation (EuCAP), 2015 9th European Conference on, pages 1–5. IEEE.

Shockley, W. (1949). The theory of p-n junctions in semiconductors and p-n junction transistors. Bell System Technical Journal, 28(3):435–489.

Simmons, J. G. (1963). Electric tunnel effect between dissimilar electrodes separated by a thin insulating film. Journal of Applied Physics, 34(9):2581–2590.

Sze, S. M. and Ng, K. K. (1981). Physics of semiconductor devices. John Wiley & Sons, New York.

Thacker, Z. and Pinhero, P. J. (2016). Terahertz spectroscopy of candidate oxides in mim diodes for terahertz detection. IEEE Transactions on Terahertz Science and Technology, 6(3):414–419.

Ting, D. Z.-Y., Hill, C. J., Soibel, A., Keo, S. A., Mumolo, J. M., Nguyen, J., and Gunapala, S. D. (2009). A high-performance long wavelength superlattice complementary barrier infrared detector. Applied Physics Letters, 95(2):023508.

Tiwari, B., Bean, J. A., Szakmány, G., Bernstein, G. H., Fay, P., and Porod, W. (2009). Controlled etching and regrowth of tunnel oxide for antenna-coupled metal-oxide-metal diodes. Journal of Vacuum Science & Technology B: Microelectronics and Nanometer Structures Processing, Measurement, and Phenomena, 27(5):2153–2160.

Weerakkody, A., Sedghi, N., Mitrovic, I., van Zalinge, H., Noureddine, I. N., Hall, S., Wrench, J., Chalker, P., Phillips, L., Treharne, R., et al. (2015). Enhanced low voltage nonlinearity in resonant tunneling metal–insulator–insulator–metal nanostructures. Microelectronic Engineering, 147:298–301.

Woolf, D., Loncar, M., and Capasso, F. (2009). The forces from coupled surface plasmon polaritons in planar waveguides. Optics express, 17(22):19996–20011.

Zhang, J. and Huang, Y. (1980). Rectennas for wireless energy harvesting. Department of Electrical Engineering and Electronics, University of Liverpool, Liverpool UK [3] Brown, William C." The History of the Development of the Rectenna." Microwave Power Transmission and Reception, 1.

Zhu, Z., Joshi, S., and Moddel, G. (2014). High performance room temperature rectenna ir detectors using graphene geometric diodes. IEEE Journal of Selected Topics in Quantum Electronics, 20(6):70–78.

Zhu, Z. J. (2014). Graphene geometric diodes for optical rectennas. PhD thesis, University of Colorado at Boulder.

Appendix A

Modified Exponential Fitting Procedure

To fit the data to Eq. 3.14, we find the pair of R_s and α values that allow the best fit for Eq. 3.13 to the modified $I(V)$ data. Given a pair of R_s and α values, the V in the (V, I) data set can be converted to V_D using Eq. 3.12. When the data is converted to (V_D, I) ordered pairs, Eq. 3.13 is now an appropriate model to fit the data. Coefficients I_0, b, and d can be determined using least squares regression, as done in section 3.

To determine the optimum R_s and α, we pick the pair of R_s and α values that give the highest coefficient of determination, R^2, for the fit of Eq. 3.13 to modified (V_D, I) data sets. To make this comparison of different values for R_s and α, we first establish a range of interest. The additional series resistance must be smaller than the smallest measured absolute diode resistance, which can be approximated as $V_{max}/I(V_{max})$, where V_{max} is the maximum measured voltage. Thus for R_s, we are interested in the following range:

$$0 \leq R_s \leq V_{max}/I(V_{max}) \tag{A.1}$$

For α, we examine this range:

$$0 \leq \alpha \leq 1/V_{max}I(V_{max}) \tag{A.2}$$

A new (V_D, I) pair is generated for every α and R_s combination. The exponential model in Eq. 3.13 is used to fit the resulting V_D vs I. The combination of R_s and α values that have the highest coefficient of determination, R^2, for the fit to Eq. 3.13 is chosen for the final model. For MIM-2, we have a maximum R^2 when $R_s = 334\ \Omega$ and $\alpha = 1125\ \Omega/V^2$. These R_s and α values lead to $b =$

8.64 V^{-1}, $d = 7.07\ V^{-1}$, and $I_0 = 1.83 \times 10^{-5}$ A. This fit procedure is also suitable for MIM-1, and shows that the series resistance is, in fact, negligible in that case. The highest R^2 is found when both $R_s = 0\ \Omega$ and $\alpha = 0\ \Omega/V^2$, resulting in identical b, d, and I_0 values established in Section 3.

Now that we have the fit coefficients for MIM-2, we can generate the fit I(V) needed to plot the responsivity, resistance and residue. Because the current in Eq. 3.14 is recursive, several steps are required to plot the resulting fit. First, we plug Eq. 3.13 in for the current in Eq. 3.12 to get an equation that relates V and V_D. Since this results in a transcendental equation, we must numerically solve for V_D values for a set of voltages, V, over any range of interest, generally ($\pm$ 400 mV). Once we have V_D, we can calculate I using Eq. 3.13. Now that we have V and I we can easily plot $I(V)$, the residue, the asymmetry, or generate resistance and responsivity curves using central difference approximation derivatives.

Appendix B

Optical Rectenna Response Analysis

B.1 Estimating Lumped-Element Optical Response

For any optical measurement of an MIM rectenna, making a calculation of the estimated lumped-element optical response provides a good reference point. The short-circuit current, I_{sc}, for an illuminated lumped-element can be calculated as follows:

$$I_{sc} = I_0 A_{abs} \eta_{ant} \eta_c \beta_0 \tag{B.1}$$

Similar to Chapter 5, I_0 is the illumination intensity, and A_{abs} is the absorption area of the rectenna. The product of I_0, A_{abs}, η_c, and η_{ant} gives the power coupled to the diode. For the bowtie antenna used throughout this work, the estimated absorption area is 24 μm^2. The remaining factor of β_0, zero-bias responsivty, in Eq. B.1 estimates the short-circuit current for a given power delivered to the diode. I can estimate $\eta_{ant} = 10\%$ and then calculate the η_c from Eq. 5.6, modified to reflect I am calculating for a lumped-element diode. The coupling equation requires values for antenna impedance, Z_A; where R_A is the real part and X_A is the imaginary part of the antenna impedance. I use the simulated values from Chapter 5 (Z_A = 112-j117 Ω).

$$\eta_c = \frac{4 R_A Z'_D}{(R_A + Z'_D)^2 + (X_A + Z''_D)^2} \tag{B.2}$$

where Z'_D is the real part and Z''_D is the imaginary part of the series equivalent diode impedance. Generally, the lumped-element diode resistance and capacitance are considered to be in parallel.

However, the coupling calculation in Eq. B.2 requires a series equivalent impedance. This series equivalent impedance of the parallel diode resistance and capacitance is calculated as follows:

$$Z'_D = \frac{R_0}{(\omega C R_0)^2 + 1} \tag{B.3}$$

$$Z''_D = \frac{-\omega C R_0^2}{(\omega C R_0)^2 + 1} \tag{B.4}$$

where R_0 is the diode zero-bias resistance, ω is the angular frequency and C is the geometric capacitance and is calculated as done in Chapter 1 in Eq. 1.3. Once I_{sc} has been calculated, any of the performance metrics can be estimated as discussed in the next section. The lumped-element device presented in this work, as well as other lumped-element devices measured by other members of my lab show good agreement between this estimation method and experimental results.

B.2 Calculating Optical Performance Metrics

For any optical measurement either open-circuit voltage or short-circuit current can be used to estimate other performance metrics. Given the relatively linear nature of my diodes, particularly over the DC voltages at which these rectenna operate (several μV), short-circuit current and open-circuit voltage can be correlated using the diode resistance and Ohm's law.

$$V_{oc} = I_{sc} R_0 \tag{B.5}$$

Either I_{sc} or V_{oc} can be used to calculate the DC power out.

$$P_{dc} = \frac{I_{sc}^2 R_0}{4} = \frac{V_{oc}^2}{4R_0} \tag{B.6}$$

where R_0 is the zero-bias diode resistance. I_{sc} can be used to calculate system responsivity, β_{sys}, as well.

$$\beta_{sys} = \frac{I_{sc}}{P_{in}} \tag{B.7}$$

where P_{in} is input power to the rectenna calculated at the product of absorption area and illumination intensity. Finally, detectivity can be calculated as follows (Rogalski, 2003; Zhu, 2014):

$$D^* = \sqrt{A_{Abs}\Delta f}\frac{\beta_{sys}}{I_n} \tag{B.8}$$

where k is the Boltzmann constant, T is temperature, Δf is detector bandwidth, and I_n is the noise current calculated as shown in the following equation.

$$I_n = \sqrt{\Delta f(2qI_{bias} + \frac{4kT}{R_0})} \tag{B.9}$$

The noise current has two components, shot noise from the DC bias current and the Johnson noise based on the diode resistance. Without an applied bias, $I_{bias} = 0$, the detectivity equation simplifies to the following:

$$D^* = \beta_{sys}\sqrt{A_{Abs}}\sqrt{\frac{R_0}{4kT}} \tag{B.10}$$

In the above case, the bandwidth, Δf, terms cancel, and the detectivity is independent of bandwidth.

Appendix C

Estimating Thermal Time Constant

If I assume the only thermal conduction path for cooling the TWD is through the substrate and that the Si acts as a uniform temperature heat sink, I can estimate the thermal time-constant for the TWD rectenna. In this case, the heat capacity is based on the mass of the metal in the TWD.

$$C_{thermal} = c\rho A t_m \tag{C.1}$$

where ρ is the average metal density, A is the area, t_m is the metal thickness, and c is the average specific heat for the metals in the TWD structure. The thermal resistance is calculated for the 300 nm SiO_2 between the TWD and the silicon substrate.

$$R_{thermal} = \frac{t_{SiO_2}}{A\sigma_{SiO_2}} \tag{C.2}$$

where t_{SiO_2} is the thickness of the SiO_2, A is the area, and σ_{SiO_2} is the thermal conductivity of SiO_2. Finally, the thermal time-constant, $\tau_{thermal}$ can be calculated as the product of the thermal resistance in Eq C.2 and the heat capacity in Eq. C.1.

$$\tau_{thermal} = R_{thermal}C_{thermal} = \frac{t_{SiO_2}}{\sigma_{SiO_2}} c\rho t_m \tag{C.3}$$

Notice, that for the final equation, the time-constant is independent of area. The necessary modulation frequency can be calculated as $1/\tau_{thermal}$. Using the parameters for the GSM fabricated TWD devices, $\tau_{thermal} \approx 19$ MHz.

Appendix D

Boston Electronics HgCdTe Photodiode

As a sanity check that my optical measurement system is correctly calibrated and that I am calculating the detector metrics properly, I measure the HgCdTe photodiode and calculate the system responsivity and detectivity. The specifications for the manufacturer indicate that the HgCdTe photodiode has a responsivity of 3.2 mA/W and a current amplifier with a transimpedance of 1.2×10^4 V/A. I illuminated the diode with the CW laser in my optical set up and modulated it by the mechanical chopper at 1.69 kHz. Since the photodiode is polarization independent, just as was done in Chapter 6, I put a linear polarizer after the half wave plate. The open-circuit voltage response is shown below in Figure D.1. To prevent damage to the photodiode and keep the output voltage within specification for the lock-in amplifier, the laser was operated at ∼30% of maximum power. The photodiode manufacture recommend limiting the power to the diode to 100 mW and the maximum input voltage to the lock-in amplifier is 1 V.

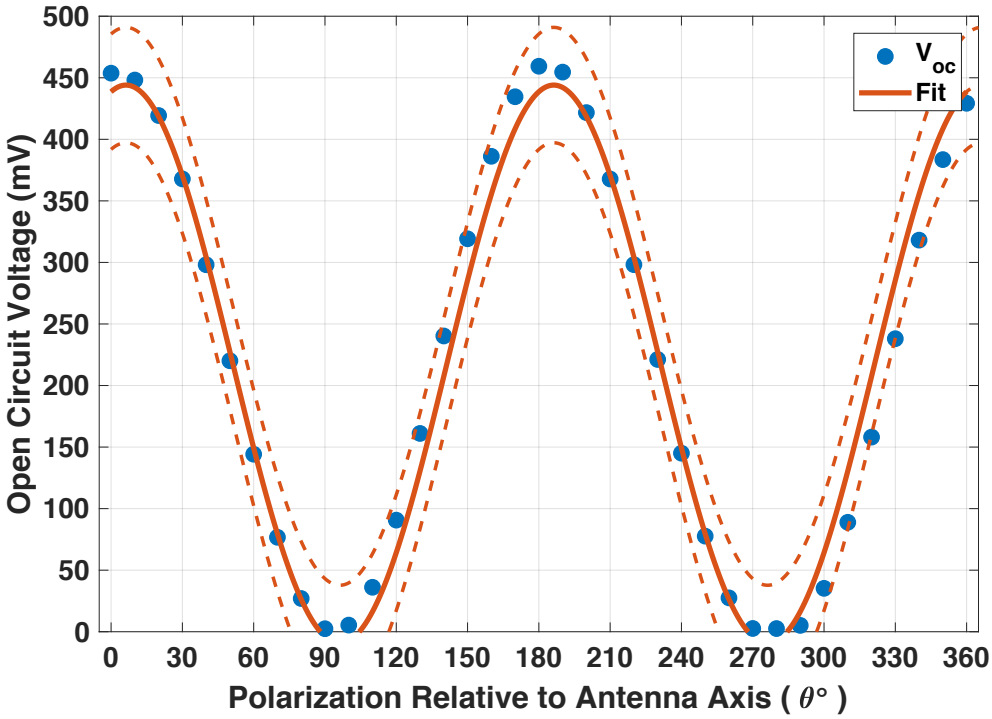

Figure D.1: Optical response of Boston Electronics HgCdTe photodiode

The data is fit to Eq. 6.8 from Chapter 6. The 95% confidence intervals are represented by the dashed lines on the figure. From the fit, V_{oc} = 444 mV. The input power is the product of the illumination intensity (0.012 W/mm^2) and the absorption area (1 mm^2), 0.012 W. I_{sc} can be calculated from V_{oc} by dividing by the transimpedance of 1.2×10^4 V/A. This yields I_{sc} = 37 μA. Dividing by the input power gives a system responsivity, β_{sys} = 3.08 mA/W, which is within specification of the reported responsivity of 3.2 mA/W ±20%.

Using the other reported performance metrics, I_n = 21 pA/$\sqrt{Hz}$ and R_d = 37 Ω combined with the measured system responsivity, I can calculate a detectivity of 1.47×10^7 Jones using the equations in Appendix B. This is also within the specification range of D^*=1.5×10^7±20% Jones.